



# Università degli Studi di Ferrara

## DOTTORATO DI RICERCA IN Scienze della Terra

CICLO  
XXI

COORDINATORE Prof.  
Luigi Beccaluva

*Structural characterization of zeolitic catalysts in non-ambient conditions by X-ray and neutron diffraction*

Settore Scientifico Disciplinare GEO/ 06

**Dottorando**

Dott. Nome e Cognome

Ilaria Parodi

**Tutore**

Prof. Nome e Cognome

Annalisa Martucci

Anni 2006/2008

## ABSTRACT

### English:

This PhD thesis strives to give an exhaustive characterization of the behaviour of zeolites in non-ambient conditions. Zeolites presents a lot of peculiar characteristics, such as shape selectivity, high thermal stability, but the most important is their catalytic activity, which have been evaluated for many petrochemical reactions, such as gas-oil cracking and hydrocracking, aromatic alkylation and isomerisation ecc.

The catalytic activity of zeolites is due to their particular structure. These minerals, in fact, are characterized by large pores and channels. Only molecules with determined dimensions, consistent with the pores dimensions, can have access to the acid sites located inside these cavities and can be processed.

The importance of a detailed structural characterization is due to the fact that it is necessary to explain the efficiency of these materials, their stability as well as the different types of shape selectivity seen in a wide range of catalytic systems.

The understanding of the zeolite behaviour upon heating is of particular importance since the sorptive and catalytic properties, molecular sieve effects are enhanced in the dehydrated/calcined phases. Besides, it is important to study the response to heating because reactions involving hydrocarbons need high temperature (about 300-500°C), so it is important that zeolites used for these reactions have a good thermal stability, and it is important to localize acid sites.

The study of the characterization of these materials in non-ambient conditions was carried out starting from structure analysis of diffraction data collected on powder or single crystals, using X-ray (conventional source or synchrotron radiation) or neutron diffraction.

The main results obtained in this PhD thesis can be summarize as follows: 1) zeolite tschernichite. It has been evaluated how defects due to the simultaneous presence of two different polytypes affect the thermal stability of this material; 2) zeolite gmelinite. The most important results is that it was possible to observe that gmelinite, when heated at  $T > 330^{\circ}\text{C}$  transform into a new phase (AFI-type) which is very important for catalysis and has a good thermal stability; 3) zeolite omega. It was possible to follow in real time the activation of this important catalyst and its acid sites were localized; 4) zeolite ferrierite and heulandite: protons bonded to framework oxygens were located, and it is put in evidence the importance of water interaction with these catalysts.

**Italiano:**

Questa tesi di dottorato si prefigge di dare una caratterizzazione esauriente del comportamento delle zeoliti in condizioni non ambiente. Le zeoliti presentano molte caratteristiche peculiare, quali la selettività di forma, un'alta stabilità termica, ma la più importante di queste caratteristiche è sicuramente la loro attività catalitica, che è stata sfruttata in molte reazioni petrolchimiche, come il gas-oil cracking, hydrocracking, alcalizzazione aromatica, isomerizzazione ecc.

L'attività catalitica delle zeoliti è dovuta alla loro particolare struttura. Questi minerali, infatti, sono caratterizzati da una struttura che presenta grosse cavità, come pori e canali. Solo molecole di determinate dimensioni possono accedere ai siti acidi presenti all'interno di queste cavità ed essere quindi elaborate.

L'importanza di una caratterizzazione strutturale dettagliata è richiesta in quanto è necessario conoscere l'efficienza di questi materiali, la loro stabilità e le differenti condizioni di selettività di forma in un ampio ambito di sistemi catalitici.

La comprensione del comportamento delle zeoliti quando sottoposte a riscaldamento è di particolare importanza in quanto le proprietà di assorbimento e catalitiche e gli effetti di setacci molecolari sono intensificati nelle fasi calcinate/disidratate. Inoltre è importante studiare come le zeoliti reagiscono al riscaldamento perché le reazioni che coinvolgono gli idrocarburi necessitano di alte temperature (circa 300-500°C), quindi è importante che le zeoliti usate per queste reazioni abbiano una buona stabilità termica, e localizzare i siti acidi all'interno delle loro strutture.

Lo studio della caratterizzazione di questi materiali in condizioni non-ambiente è stato effettuato partendo dall'analisi della struttura da dati di diffrazione raccolti su polveri o su cristallo singolo, tramite raggi-X ( sorgenti convenzionali o radiazione di sincrotrone) e diffrazione neutronica.

I risultati ottenuti in questa tesi di dottorato possono essere così riassunti: 1) zeolite tschernichite. È stata evidenziato come i difetti dovuti alla presenza simultanea di due politipi influenzano la stabilità termica di questo materiale, 2) zeolite gmelinite. Il risultato più importante è stato che è stato possibile osservare che la gmelinite, quando riscaldata a più di 330°C, si trasforma in una nuova fase (di tipo AFI), molto importante per la catalisi e con una buona stabilità termica, 3) zeolite omega. È stato possibile seguire in tempo reale l'attivazione di questo catalizzatore e localizzare i siti acidi al suo interno, 4) zeolite ferrierite e heulandite: sono stati localizzati i protoni legati agli ossigeni del framework ed è stata messa in evidenza l'importanza dell'interazione con l'acqua per questi catalizzatori.

<b>INTRODUCTION</b>	1
<b>CHAPTER 1: ABOUT ZEOLITES</b>	
1.1. Generalities of zeolites	3
1.2. Crystallochemistry of zeolites	4
1.3. Classifications of zeolites	6
1.4. Genesis of zeolites	8
1.5. Synthesis of zeolites	9
1.6. Properties and applications of zeolites	12
1.7. Zeolites as catalysts	14
<b>CHAPTER 2: THERMAL BEHAVIOUR OF ZEOLITES</b>	
2.1. Introduction	17
2.2. History of the study of the thermal behaviour of zeolites	17
2.3. Classification of zeolites based on their thermal behaviour	18
2.4. Modifications induced by heating	20
2.5. Factors governing the thermal behaviour of zeolites	21
<b>CHAPTER 3: EXPERIMENTAL METHODS</b>	
3.1. Introduction	24
3.2. Single crystal X-ray diffraction	25
3.3. X-ray powder diffraction	27
3.4. Synchrotron radiation	30
3.5. Neutron diffraction	33
3.6. Thermal analysis	
<b>CHAPTER 4 – ZEOLITE TSCHERNICHITE</b>	
4.1. Tschernichite and zeolite beta: structural and chemical features	36
4.2. Experimental	38
4.2.1. The choice of experimental approach	38
4.2.2. Experimental method	40
4.2.3. Structural refinements	41
4.3. Structural refinements results	41
4.3.1. The two phase fractions in the large and small crystals, respectively	41
4.3.2. Thermal stability	44
<b>CHAPTER 5 – ZEOLITE GMELINITE</b>	
5.1. Gmelinite: structural and chemical features	47
5.2. Experimental	49
5.2.1. Material	49
5.2.2. In-situ single crystal analysis	49
5.2.3. Ex-situ x-ray powder data collection	50
5.2.4. Ex-situ single crystal data collection	52
5.2.5. In-situ time-resolved synchrotron data collection	52
5.3. Structure refinements	53
5.3.1. In-situ single crystal analysis	53
5.3.2. Ex-situ single crystal refinements	53
5.4. Results and discussion	53
5.4.1. Crystal structure from in-situ single-crystal analysis at room temperature (GME-RT)	53

5.4.1. Crystal structure from in-situ single-crystal analysis at room temperature (GME-RT)	53
5.4.2. Crystal structure from in-situ single-crystal analysis at 100K (GME-100K)	54
5.4.3. Crystal structure from in-situ single-crystal analysis after the cooling (GME-RTr)	55
5.4.4. Crystal structure from in-situ single-crystal analysis at T=50°C (GME-50)	56
5.4.5. Crystal structure from in-situ single-crystal analysis at T=75°C (GME-75)	56
5.4.6. Crystal structure from in-situ single-crystal analysis at T=90°C (GME-90)	56
5.4.7. Crystal structure from in-situ single-crystal analysis at T=75°C (cooling) (GME-75r)	57
5.4.8. Crystal structure from in-situ single-crystal analysis at T=25°C (cooling) (GME-25r)	57
5.4.9. Crystal structure from in-situ single-crystal analysis at T=25°C (aft.3 ds) (GME-25r-3d)	57
5.5. Discussion of in-situ single crystal data	58
5.6. Discussion of ex-situ data	59
5.7. Discussion of in-situ time-resolved synchrotron powder diffraction data	62
Tables	64

## **CHAPTER 6 – NH<sub>4</sub> FORM OF ZEOLITE OMEGA**

6.1. Zeolite omega: structural and chemical features	69
6.2. Experimental	72
6.2.1. Material	72
6.2.2. Experimental conditions	72
6.2.3. Structure refinements	73
6.3. Results of structure refinements	74
6.3.1. Crystal structure refinement of NH <sub>4</sub> -omega zeolite at room temperature	74
6.3.2. Refinement by in situ X-ray data: temperature dependent unit cell variations	75
6.3.3. Refinement by in situ X-ray data: temperature-dependent occupation of the extraframework sites	76
6.3.4. Thermogravimetric analysis	78
6.3.5. Refinement by in situ X-ray data: temperature-dependent deformation of the framework and evidences of formation of Brønsted acid sites	79
Tables	83

## **CHAPTER 7 – ZEOLITE FERRIERITE**

7.1. Ferrierite: structural and chemical features	87
7.2. Catalytic properties and proton transfer in ferrierite	88
7.3. Experimental	89
7.4. Results of structure refinements	90
7.5. Discussion	92
Tables	92

## **CHAPTER 8 – ZEOLITE HEULANDITE**

8.1. Introduction	98
8.2. Experimental	99
8.2.1. Materials	99
8.2.2. Neutron data collection	100
8.3. Results of refinement and discussion	101
Tables	107

## **CHAPTER 9 – CONCLUSIONS**

109

## **CHAPTER 10 – REFERENCES**

111

## INTRODUCTION

Zeolites are microporous materials that have found wide use in industry since the late 1950s, with one of their most important applications being chemical catalysis. They are particularly important as cracking catalysts in oil refining. One of their defining features—apart from being solid catalysts that are easy to recycle—is that the shape, or topology, of the internal pore structure of a zeolite can strongly affect the selectivity with which particular product molecules are formed in chemical transformations catalysed by the zeolite. The original explanation for the shape selectivity associated with zeolite catalysis is simple and intuitive: the pores, or rather the active sites within the pores, exclusively process the molecules that fit inside. Significant technical advances over the last decades have made it possible to synthesize and characterize well-defined zeolite crystals, and to measure diffusion and adsorption processes accurately in a number of zeolite/hydrocarbon systems.

A detailed structural characterization can explain the efficiency of these materials, their stability as well as the different types of shape selectivity seen in a wide range of catalytic systems. The catalytic activity of zeolites depends on the presence in their structure of the so-called “Brønsted acid sites”. These acid sites, which are responsible for the catalytic activity of zeolites, are due to the presence of Al due to the substitution  $\text{Al} \rightarrow \text{Si}$  in the framework structure. This substitution create a charge unbalance in the framework which is compensate by protons attached to the framework oxygens. These protons constitute acid sites that can catalyse the two types of reaction important in all oil refining: the isomerization and the cracking of hydrocarbons. The principal mechanism of acidity in these materials is the donation of Brønsted acid protons from bridging framework hydroxyls. The location and population of these hydroxyl groups in hydrogen zeolites provides a basis for the interpretation of their properties. For this reason, the protonated or deuterated forms of zeolites have long been a subject of research.

The understanding of the zeolite behaviour upon heating is of particular importance since the sorptive and catalytic properties, molecular sieve effects are enhanced in the dehydrated/calcined phases. Besides, it is important to study the response to heating because reactions involving hydrocarbons need high temperature (about 300-500°C), so it is important that zeolites used for these reactions have a good thermal stability.

The aim of this work is to characterize zeolitic catalysts in non-ambient conditions starting from structure analysis of diffraction data collected on powder or single crystals, using X-ray (conventional source or synchrotron radiation) or neutron diffraction. In particular, my interest is focus on the following zeolites:

- 1) zeolite tschernichite. Thermally-induced modifications of both monoclinic and tetragonal polytypes of tschernichite have been studied by in-situ “time resolved” synchrotron powders diffraction data collected in the temperature range 30-800°C. These results are of particular interest as tschernichite is the natural analogue of an

important acid catalyst like beta, in which it is not possible the physical separation of the two polytypes.

- 2)  $\text{NH}_4$  zeolite omega. This is a large pore material known for its strong Brønsted acidity and adsorption capacities for large molecular species. The in-situ heating process (temperature range: 50-100°C) of the ammonium form of this catalyst was performed in order to have evidence about the formation of acid sites and to study thermally-induced modifications which accompany this process.
- 3) zeolite gmelinite. The interest in gmelinite was due to the straight 12-ring channel, which can make this zeolite a good catalyst for hydrocarbons conversions. This zeolite was studied in order to have an exhaustive picture of the structural modifications, the dehydration-rehydration process, and the phase transformations from 100K to collapsing temperature, studied by single crystal and powder X-ray diffraction.
- 4) zeolite ferrierite. The characteristic behaviour of this zeolite is a high conversion with low isobutene selectivity at a short time-on-stream, being it associated with the presence of strong acid sites. In this work particular interest is focussed on the rehydrated acidic-ferrierite to localize the Brønsted acid sites and to study if water in interaction with acid sites forms hydroxonium ions, hydrogen-bonded water, isolated water or free OH groups. Neutron diffraction was used with this aim as it is the most direct experimental method used to probe Brønsted acid siting because neutrons interact strongly enough with hydrogen nuclei to have a significant effect on diffracted intensities. For this study, data were collected at 2.5K.
- 5) zeolite heulandite. Heulandite-type zeolites are among the most abundant microporous aluminosilicates in nature. As for ferrierite, the aim of this work is to determine position and concentration of hydroxyl groups in calcined D-heulandite and their interaction with water molecules via powder neutron diffraction. Also for this study, data were collected at 2.5K.

## 1.1) GENERALITIES OF ZEOLITES

The discovery of natural zeolites dates back to 1756. Their discovery is attributable to A.F. Cronsted, who observed that these minerals (stilbites, in particular), when heated, release vapour, and coined the term “zeolite” (from the Greek words *zeo*= to boil and *lithos*= rock; that is, boiling stones). After this first discovery the zeolite family grew.

Despite there being more than 170 zeolites, only thirty of them are natural compounds. The others are obtained in laboratories by synthesis processes and are defined as “synthetic zeolites”.

The first author to deal with synthetic zeolites was Barrer in 1938, in a pioneering work, after Weigel and Steinhoff found that it was possible to separate gas molecules according to their size using a dehydrated zeolite, in 1925. On the basis of this study, a lot of synthetic zeolites were produced. The advantage of using synthetic zeolites is that the chemical composition and pore size of these materials can be chosen (Barrer, 1982).

Since the first definition of zeolite was provided by Cronsted, there have been many other definitions.

All these definitions have had to consider the vast chemical variability of zeolites.

One of the most important definitions was given by Smith (1963). According to this author, a zeolite is a mineral which shows the following characteristics:

“Aluminosilicate which has a 3D framework, built up by tetrahedral  $TO_4$  (with  $T = Si^{4+}$  or  $Al^{3+}$ ), sharing all their vertices (tectosilicates, a family of minerals with  $T/O$  ratio =  $1/2$ ). These tetrahedra gather to form a structure characterized by a lot of empty spaces, such as channels and cages, and so it can be defined as an open structure (framework density  $< 20$  atoms/ $\text{\AA}^3$ ).

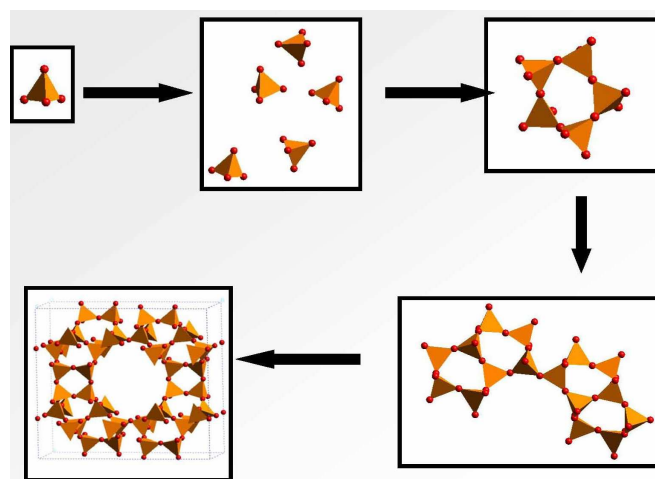


Figure 1: How zeolites are built

Furthermore, cavities in the structure are occupied by water molecules and extraframework cations (alkali cations,  $Ca^{2+}$ ,  $Mg^{2+}$ ,  $K^+$ ,  $Na^+$ ), which compensate the charge imbalance due to isomorphic substitution  $Al^{3+} \rightarrow Si^{4+}$  in tetrahedra. Both cations and water molecules are

characterized by high mobility (this explains the great interest in zeolites). In some cases Al can be substituted by Fe<sup>3+</sup>, B<sup>3+</sup>, Ga<sup>3+</sup>.

The degree of Si/Al substitution follows the Lowenstein rule (1954), according to this rule Al in adjacent tetrahedra are energetically unfavoured.

The definition given by Smith had some limitations since some natural or synthetic compounds show zeolitic properties but could not be included in the definition.

In fact, there are some materials in which tetrahedral sites are not occupied by Al or Si (for example, pahasapaite has neither Si nor Al in its framework, only B and P). Besides this, in some materials the framework is interrupted by OH groups, such as roggianite and maricopaite, or other materials are characterized by a tetrahedric framework and large cavities, but they do not have extraframework cations, (such as AIPO, SAPO, clathrasil).

A wider definition was needed, which did not put constrains on the framework chemical composition and could include an interrupted framework.

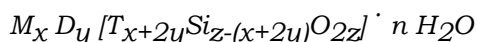
This definition was given by IMA CNMMN (International Mineralogical Association, Commission on New Minerals and Mineral Names (Coombs et al; 1998)). According to this definition "Zeolite mineral is a crystalline substance with a structure characterized by a framework of linked tetrahedra, each consisting of four O atoms surrounding a cation. This framework contains open cavities in the form of channels and cages. These are usually occupied by H<sub>2</sub>O molecules and extra-framework cations that are commonly exchangeable. The channels are large enough to allow the passage of guest species. In the hydrated phases, dehydration occurs at temperatures mostly below about 400°C and is largely reversible.

The framework may be interrupted by (OH,F) groups; these occupy a tetrahedron apex that is not shared with adjacent tetrahedra ".

This definition has been widely used for every review on zeolites, because it can include all those minerals which show zeolitic properties, such as reversible dehydration, cationic exchange and molecular sieves.

## 1.2) CRYSTALLOCHEMISTRY OF ZEOLITES

The general formula for zeolites based on Smith's definition can be written as:



With:

framework composition inside the parenthesis

M= alkali cations more or less exchangeable (Na, K, Li)

D= cations such as Mg, Ca, Sr, Ba (Fe, Mn)

T= tetracoordinated cations

and

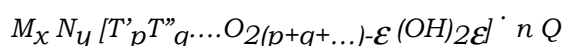
$$0 \leq x \leq 0.5 z$$

$$0 \leq y \leq 0.25 z$$

$$0 \leq x+2y \leq 0.5 z$$

$$0.3 z \leq n \leq 1.2 z$$

According to the CNMMN (natural or synthetic) definition, the general formula for zeolites can be written as follow:



With:

M= alkali cations more or less exchangeable (Na, K, Li)

N= non-metallic ions or organic molecules

T= tetrahedric coordinated cations

Q= adsorbed molecules (not only water)

Many authors, however, tend to prefer the other, more restrictive definition.

The variations in chemical composition of zeolites are affected by the type, charge and dimension of extraframework cations, and by the Si/Al ratio.

The Si/Al ratio is a very important factor among those which determine the physical properties of zeolites, because it can give some clue to charge localisation and therefore the localisation of extraframework cations or possible acid sites. On the basis of the Lowenstein rule, this ratio has a lower limit of 1 since it is unlikely that an  $AlO_4$  tetrahedron could be bonded to another  $AlO_4$  tetrahedron by sharing their oxygens. When Si/Al=1 (as in the case of gismondine), Si and Al tetrahedra regularly alternate and build up an ordered structure. The upper limit for the Si/Al ratio is a maximum value of six (clinoptinolite, mordenite) or seven, as is the case for mutinaite, to date the poorest Al zeolite studied. In synthetic zeolites this value does not have any upper limits (or is infinite, as is the case for silicalites).

As can be seen above, extraframework cations balance the negative charge due to Si/Al substitution. These cations are localised in the cavities of the framework. They can be bonded to framework oxygens or to water molecules. In the latter case, water molecules build up a "moisturising sphere" around the extraframework cations, pointing their negative dipole towards the cation. It is important to note that the number of water molecules inside the channels is affected by crystallisation conditions and by the nature of bonded cations. In fact, divalent cations tend to have a bigger moisturising sphere than monovalent cations.

On the whole, it is possible to divide the zeolites structure into three parts: the framework, the exchangeable cations and the water molecules. These three components are strictly chemically bonded since a variation in of one of them induces variations in the other two. For example, Si/Al distribution affects the chemical composition and the distribution of cations and acid sites, and for this reason, the distribution of the molecules. The geometry of the tetrahedric framework and

its potential distortion is linked to these factors, but also to other processes such as dehydration and the removal of extraframework cations.

### **1.3) CLASSIFICATIONS OF ZEOLITES**

The physical properties of zeolites are strictly interconnected with their crystalline structure (i.e. the topology and geometry of the framework), so a good classification for zeolites should be based upon structural considerations. This classification, furthermore, does not account for composition, atom distribution in T sites, unit cell symmetry or dimensions, as it only refers to the way the framework atoms bond together.

The classification proposed by Meier et al. (1996) is based on framework topology. This classification was approved by the “Structures Commission” of the “International Zeolite Association”, in agreement with rules established by the IUPAC (International Union of Pure and Applied Chemistry). It comprises a great number of compounds, both synthetic and natural. This classification assigns a three letter code (called a “framework code type”) to each kind of framework. Every framework type comprises distinct compounds which can be different in composition, symmetry, unit cell dimension, extraframework content, but all with the same framework topology, that is to say, the same topological symmetry, TS (Smith, 1974). The word “structural type” is synonymous with “framework”. To date, 170 framework code types have been assigned. They have all been collected in the Atlas of Zeolite Framework Types (also available online as a database). Another important feature connected to this classification is the concept of Framework density (FD), strictly linked to zeolite porosity. The FD is equivalent to the number of tetrahedral atoms per  $1000\text{Å}^3$ . In a zeolite this value must be less than 19-21 (Meier et al., 1996). For all the other siliceous frameworks this value is more than 27.

In order to describe zeolite structures, it is possible to use structural units with different levels of complexity to make up the fundamental zeolite topological pattern. The starting unit is the  $\text{TO}_4$  tetrahedron (which is called the “primary building unit” or PBU), (Meier, 1968). Therefore, the framework is described as a three-dimensional net built up of points (corresponding to the Si and Al atoms in tetrahedra). In this net every point is connected to four other points, and the oxygen framework lies near the lines connecting to the contiguous tetrahedra. Inside this scheme it is possible to recognize the so-called “SBU”, or Secondary Building Unit, which is the simplest configuration which forms a tetrahedric framework. The IUPAC classification is based on these SBUs, in fact, distinct framework topologies are described as the combination of SBUs.

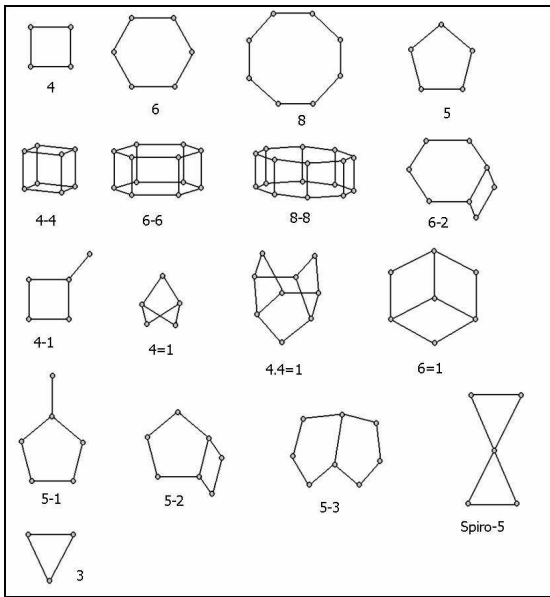


Figure 2: Secondary Building Units (SBU) of zeolite structures

(from: Atlas of Zeolite Structure Types)

Meier et al. (1968) described nine SBUs: 4, 6 and 8-membered rings, double rings 4-4, 6-6, 8-8, complex unities 4-1, 5-1 and 4-4-1. Subsequently, eight other SBUs have been recognized.

The 17 SBUs are reported in Figure 2.

For some zeolites it is better to describe their structure using “finite structural subunits” (SSUs), which are polyhedral forms characterized by quite complex symmetry, such as gmelinite or sodalite cages.

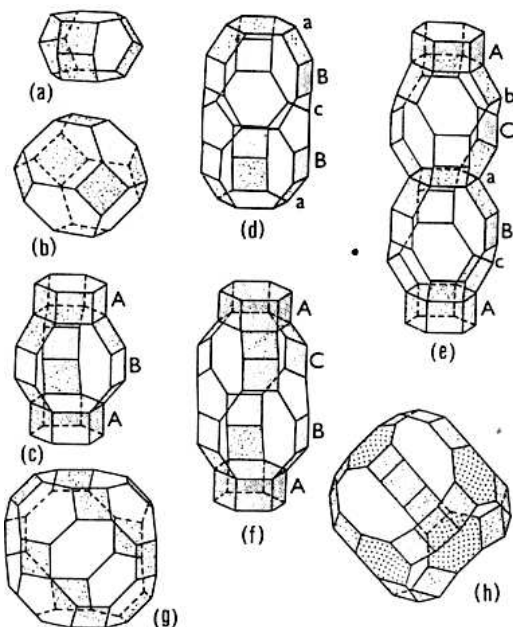


Figure 3: some cages in zeolites:

- (a) cancrinite cage;
- (b) sodalite cage (or  $\beta$  cage);
- (c) gmelinite cage;
- (d) erionite cage;
- (e) levyne cage;
- (f) chabazite cage;
- (g)  $\alpha$  cage;
- (h) faujasite cage

(from : Tsitsishvili et al., 1992).

These forms can help the description of more complex structures (Smith, 1963). For some zeolites, furthermore, the concept of “infinite units” has been introduced, so some frameworks are

described as a distorted overlapping of layers, built up by nets, joined by tetrahedral rings, or as parallel chains with precise configurations (Figure 3).

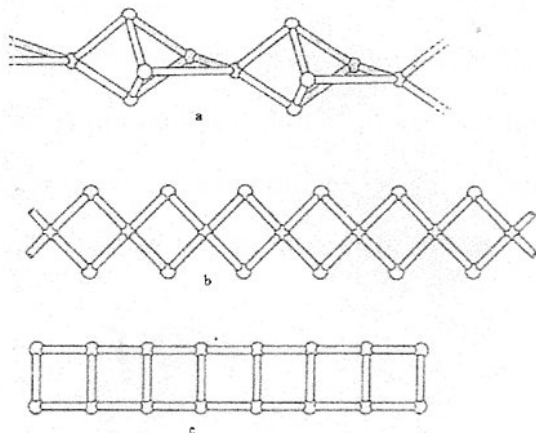


Figure 4: infinite units in zeolites.

The choice of describing zeolite structures using a precise structural pattern is an arbitrary one, since, due to its great variety, a universal criterion cannot exist. This is also due to all the characteristics which it is necessary to highlight, such as the topology, geometry, cavity forms and dimensions, relationship with other structures, etc.

#### 1.4) GENESIS OF ZEOLITES

Zeolites usually crystallise in high alkaline conditions ( $\text{pH} > 7$ ) and at low pressure and temperature ( $< 300^\circ\text{C}$ ). Natural zeolites can have two types of genesis:

- a) Hydrothermal. Crystals are generated in cavities and fractures of igneous rocks (mostly basalts, but also plutonic and metamorphic rocks), which are deposited by the precipitation of hot aqueous solutions of magmatic origin. The interaction between the magmatic fluid and the rocks in decreasing pressure allows the crystals nucleation inside the cavities. The result is macroscopic dimension crystals in small percentages in comparison with the hosting rock. The Si/Al ratio is affected by the chemical composition of the percolating fluid.
- b) Diagenetic. The formation of zeolite crystals is inside pyroclastic blankets exposed to meteoric water or layer water. Permeating fluids loosen the silicatic component (above all made of glass) of the blankets. From the resulting Si-Al-Mg-Ca-K rich solution, submicroscopic crystals deposit in high amounts.

Diagenetic zeolites are called “sedimentary zeolites”, and rock which contains more than 50% of zeolitic components are called zeolitites. In particular, if these rocks are permeated by a layer of meteoric water, the zeolitisation process can be zoned horizontally (geologic closed system) or vertically (geologic open system). In these kind of rocks, the zeolitisation process gives all the peculiar properties of zeolites, (structural microporosity, ion exchange, selective adsorption,

hydrophilic properties, reversible dehydration) in proportional percentages to zeolites in rock. Besides this, they maintain textural porosity, permeability and a low specific weight.

### 1.5) SYNTHESIS OF ZEOLITES

The study of synthetic zeolites was begun by Barrer in 1938. Initially, interest in this work was quite scarce, because of difficulties in obtaining crystalline pure phases. Then, during the 50s, when easier synthesis conditions were discovered, interest began to increase.

In these conditions a great number of zeolites were synthesised, the most important among them are A, X and Y zeolites. Further progress occurred when the possibility of using organic molecules, called templates, either as pure phases or as an additive to metal oxides was discovered (thanks to this method the synthesis of Si-rich zeolites was made possible).

Three types of processes can be distinguished. These processes differ mainly on the basis of the materials used for the synthesis:

- synthesis from hydrogel or reactive aluminosilicates
- synthesis from clays (kaoline in particular)
- synthesis from natural materials

PROCESS	REAGENT	PRODUCT
From a hydrogel	Reactive oxides Soluble silicates Soluble aluminates Caustic soda	<ul style="list-style-type: none"> <li>• High purity powders: A, X, Y zeolites and softener (Zeolon)</li> <li>• High purity products: A, Y zeolites, softener</li> <li>• Zeolites in amorphous matrix: Y zeolite</li> <li>• Powders at various levels of purity: A, X, Y zeolites</li> </ul>
From a clay	Native kaolin Metakaolin Calcined kaolin Soluble silicates Caustic soda Sodium chloride	<ul style="list-style-type: none"> <li>• Various shapes obtained by in situ crystallisation (high purity and without ligands): A, X, Y zeolites and softener</li> <li>• Clay groundmass, for partial crystallisation: X and Y zeolites</li> </ul>
From natural compounds	Natural silica Acid-treated clay Amorphous mineral Caustic soda	<ul style="list-style-type: none"> <li>• Powders at various levels of purity Y zeolites and softener.</li> <li>• Y zeolite in clay groundmass</li> <li>• A and Y zeolites supported on ceramic</li> </ul>

Table 1: synthetic zeolites: processes, reagents and products.

In order to simplify, zeolites can be synthesised by heating a reaction mixture made up of silica and alumina gel, various cations (also of an organic nature, such as TMA, Figure 4), and a base mixed with distilled water in an oven. Synthesis is carried out in high pH conditions.

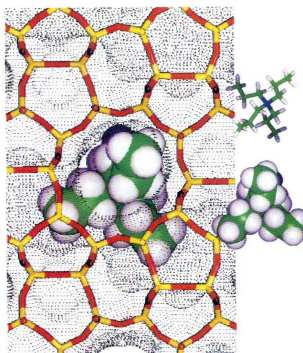


Figure 4: template molecules act as a structure directing agents around which zeolites can grow.

The time required for synthesis is usually brief and the temperature quite low (about 120°C).

Isoelectric elements with Si or Al ( $B^{+3}$ ,  $Ga^{+3}$ ,  $Fe^{+3}$ ,  $Cr^{+3}$ ,  $Ge^{+4}$  e  $Ti^{+4}$ ) may enter the structure during synthesis.

The physical properties and the chemical composition of the reaction mixture (the so called “reaction gel”), the global chemical composition, the nature of templates, the pressure and the last of heating treatment are very important parameters. They determine the properties of synthesised zeolites, such as its structure, morphology, particle sizes, particle size distribution, homogeneity of elements within the crystallites and many more.

Typical precursor materials are:

- oxide sources :  $SiO_2$  (Aerosol, Ludox, Siloxane, prec. Silica, Na/K water glass, fly ash) and  $Al_2O_3$  (Al salt,  $AlOOH$ ,  $Al(OH)_3$ , Na-aluminate);
- Template: Amine, alkylammonium salt, alcohol, ( $Na^+$ );
- Mineralizer:  $NaOH$ ,  $NH_4OH$ ,  $HF$

An organic template molecule, such as amines, alkylammonium salts or alcohols, has to be added to the reaction mixture. These structure directing agents are essential for the formation of a large number of zeolitic materials (Figure 5). Nevertheless, the role of the template molecule in the synthesis of zeolites is not absolutely clear. The most accepted mechanisms of interaction of template to form zeolites are:

- The true template effect. The organic molecule determine the topology of zeolite on the basis of its own shape, and zeolite is formed around it.
- The pore filling effect. The template stabilizes the micropores of the zeolite by filling them and, thus, preventing a collapse of the pores

Other important parameters for the synthesis of zeolites are the gel composition, the gel aging, the seeding, the temperature ramp, temperature and time of reaction and the order of mixing. The variation of the mixture chemical composition affects the growth rate of crystals and nature and composition of the final product.

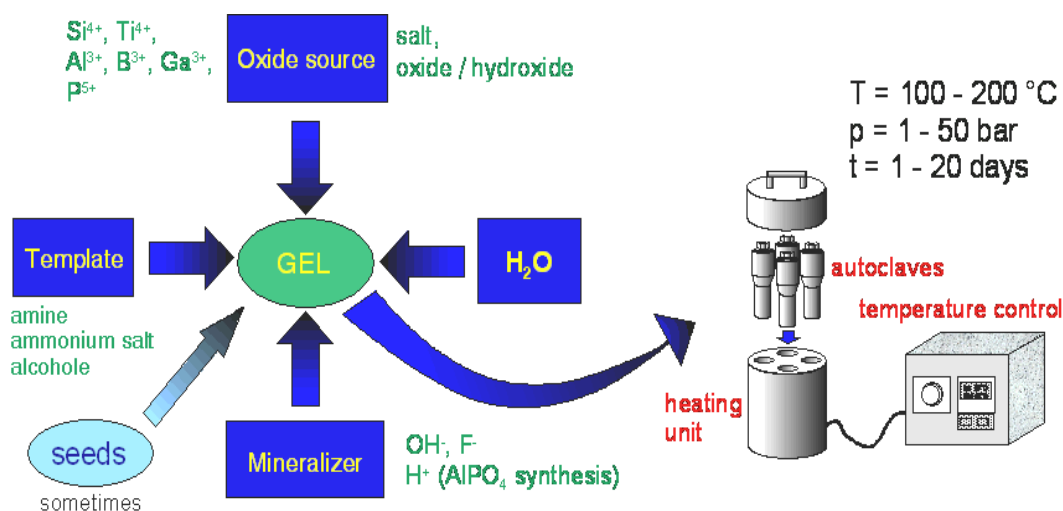


Figure 5: a typical synthesis process for zeolites.

A typical synthesis process consists of the transition from the first phase, in which the reagents are mixed (disordered state) to the nucleation phase (microscopically ordered state) and finally to crystal formation (macroscopically ordered state). The crystal formation mechanism is very complicated. There are two extreme formation mechanisms (Figure 6): the solution transport mechanism, which involves nuclei formation and the following growth in the liquid phase, and transformation into the solid phase mechanism, in which crystallisation takes place directly in the amorphous gel.

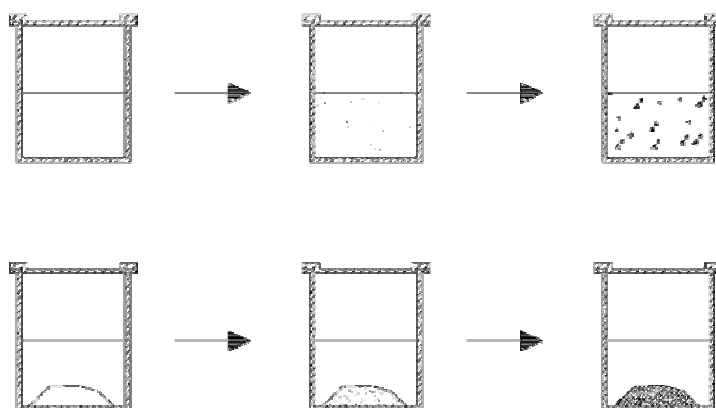


Figure 6: the two possible extreme mechanisms for zeolites formation.

The formation of zeolites takes place using one on these two mechanisms, but also with the joint application of both these methods.

Depending on which synthesised zeolites are used, other post-synthesis treatments can be applied. For example, in order to obtain catalytically active zeolites, sodium in the structure must be exchanged with an ammonium ion, and then the zeolite must be calcined, in order to remove the ammonium and leave only protons.

## 1.6) PROPERTIES AND APPLICATIONS OF ZEOLITES

The study of zeolite properties allows these minerals to be used for a great number of industrial processes and, to date, many new applications have been discovered thanks to continuous studies in this field.

Zeolite physical-chemical characteristics are the reason why zeolites are so interesting with regard to so many processes (Table 2).

These characteristics are:

1) High cation exchange. Cation exchange is the reversible interchange of two cations between two compounds, one of these (the exchanger) is not soluble in the material in which this exchange takes place.

A scheme of the process can be the following:  $Z A^{x+} + S B^{y+} \leftarrow \rightarrow Z B^{y+} + S A^{x+}$

For example, an Na zeolite when put into an  $NH_4$  solution can exchange its cations with those from the solution. If the exchanged zeolite is monocationic, in a brief time it will be completely exchanged, while if it is polycationic, it will exchange only those cations with low solvation energies. The exchange property is affected by the Si/Al ratio.

Zeolites as cationic exchangers are above all used as purifiers for polluting solutions and as amendants for soils. Other examples are cationic exchangers: for the temporary capture of such ions as  $NH_4$  and K and their subsequently low discharge after an exchange with Na and Ca in the soil. This process leads to more extensive use and a lesser extent of loosening and leaching, P transfer and solubilisation of insoluble phosphate materials, and the possibility of using tricalcic phosphates as fertilizers or in recovering insoluble P in the soil, the capture of polluting (Cu, Pb, Zn) and radiogenic (Cs, Sr) metals and the consequent decrease in their assimilation into the soil.

2) Reversible dehydration. Zeolite structures can easily expel from zeolitic water molecules and water coordinated to extraframework cations, even at low temperatures (200°C) or for vacuum treatment.

3) High adsorption capacity. The word “to adsorb” means the ability of a material to adsorb gas or liquid molecules on its surface. In the case of zeolites, even the walls of cavities act as external surfaces. Adsorbed molecules are captured by superficial charges not bonded in the framework. The ability of a zeolite to adsorb is affected by its Si/Al ratio, in fact, a higher Si/Al value implies a lower surface charge density, this leads to lower adsorption ability and to more

hydrophobic behaviour by the zeolite. Some zeolites, for example, are used to remove SO<sub>2</sub> from polluted emissions in industrial furnaces. In this kind of process, zeolites are very useful, thanks to the fact that their structure does not show modifications until 700°C.

4) Molecular sieve. Dehydrated zeolites have empty channels and cages, so these zeolites can adsorb a lot of molecules (not only water). In this way zeolites can be used to purify or segregate materials. The selective capacity of zeolites is not only affected by their Si/Al ratio but also by the dimension of pores and channels which host molecules. In this way zeolites can act as molecular sieves, that's to say, for a mixture of two components which are different in shape and dimension, in transit through zeolite channels will separate different components. According to Barrer (1958) the minimum diameter required to allow the transit of molecules is one of a six ring tetrahedra.

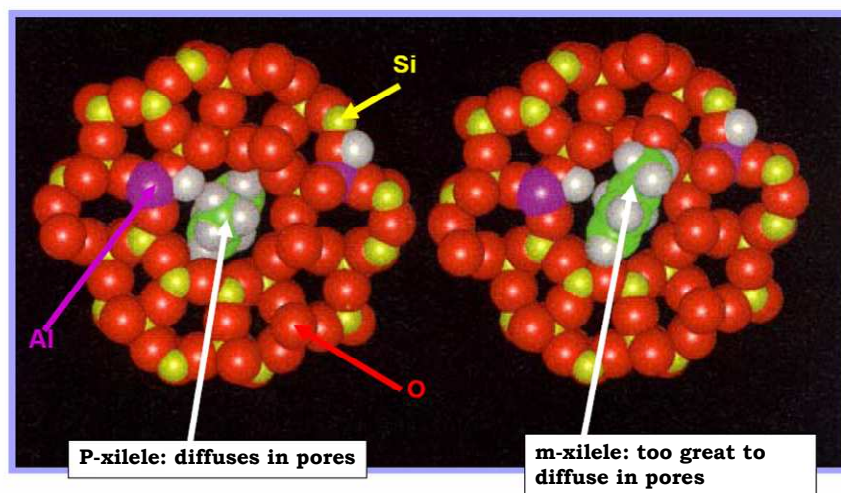


Figure 7: zeolites as molecular sieves. The use of H-ZSM-5 for xylene isomerization (from Attilio Citterio, 2006)

	Characteristics	Application fields
<b>Natural Zeolites (sedimentary)</b>	<ul style="list-style-type: none"> <li>Limited availability</li> <li>Limited number of structural types</li> <li>Limited level of purity</li> <li>Less expensive</li> </ul>	Zootechnical, air and water treatment and purification, agriculture, construction
<b>Synthetic Zeolites</b>	<ul style="list-style-type: none"> <li>Unlimited availability</li> <li>Large number of structural types</li> <li>High level of purity</li> <li>More expensive</li> </ul>	Petrochemical industry and detergent

Table 2: Application fields of natural and synthetic zeolites

## 1.7) ZEOLITES AS CATALYSTS

Catalysis is probably the most important application for zeolites. The properties which make zeolites such excellent catalysts are their good thermal stability and their high surface area. Using zeolites as catalysts it is possible to treat 100 times the amount of molecules which would be treatable with other catalysts. Furthermore, thanks to their ability to act as molecular sieves, zeolites can show shape selectivity, that is to say, only molecules characterised by a specific shape and dimension can reach an acid site.

In catalytic processing, the capacity to adsorb molecules is widely used to control molecules from entering catalytically active sites. It is possible to distinguish three situations (Figure 8):

- 1) selectivity to a reagent: only molecules with shapes and dimensions smaller than that of the pore system can reach the acid sites (for example a linear hydrocarbon can be adsorbed while a branched one cannot enter);
- 2) selectivity to products: only specific reaction products can enter the pores (for example xilene: three type of xilene are formed inside the channel but only one of them can go out);
- 3) selectivity to a transition state: some reactions are prevented because the transition state (activated complex) needs more space than available in the zeolite cavities (for example transalkylation of diakyl-benzene) .

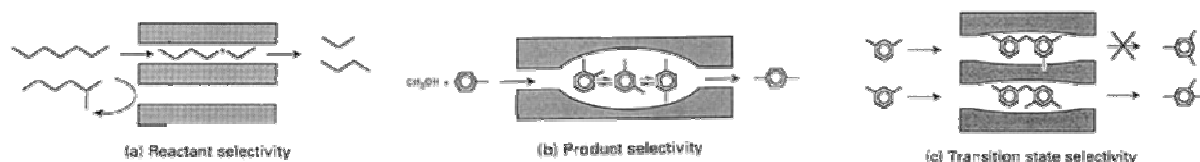


Figure 8: types of catalytic processes

For some reaction mechanisms acid sites are very important. Brønsted acid sites can be considered as protonated oxygens which act as a Si-O-Al bridge, in which the H<sup>+</sup> proton bonds to the oxygen to balance the charge imbalance in the framework due to the substitution Al → Si in the tetrahedral (Figure 9). The amount of acidity is affected by the Al content in the tetrahedral sites, and it is one of the most interesting aspects of zeolites as catalysts.

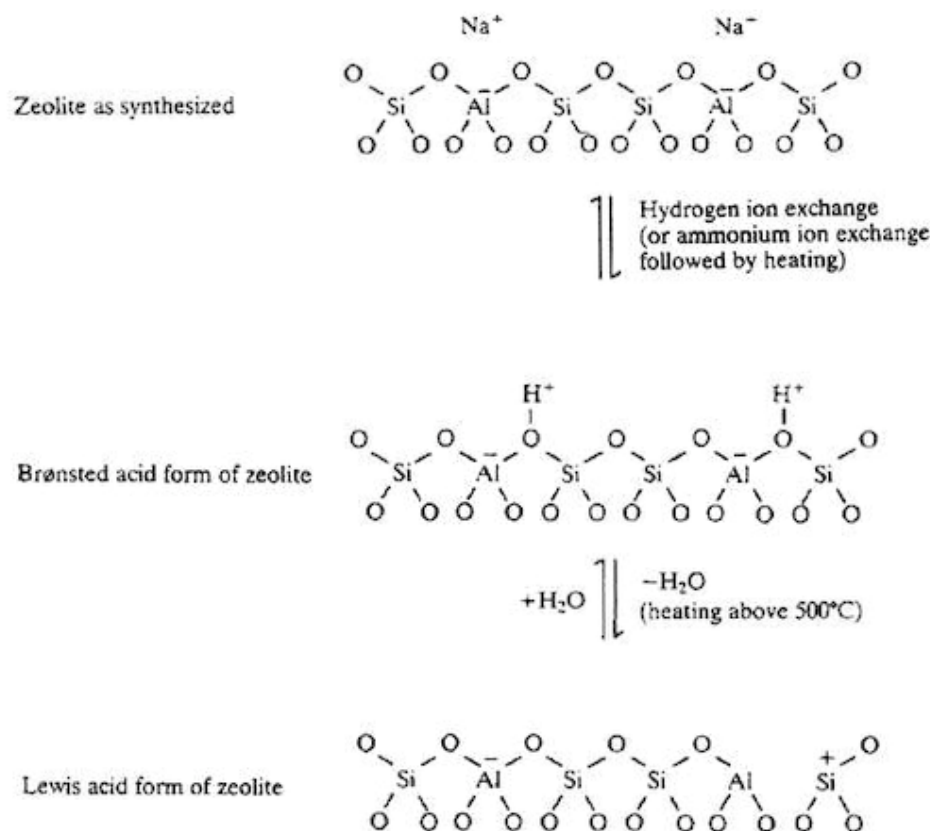
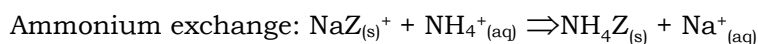


Figure 9: Schemes for generation of Brønsted and Lewis acid sites in zeolites

Zeolites are usually synthesised using Na ions which can balance the negative charges in the structure: to obtain catalytically active zeolites it is necessary to exchange Na ions with protons by a direct exchange reaction with an aqueous solution, in this way it is possible to form Brønsted acid sites. Usually, zeolites are exchanged in solution with ammonium ion,  $\text{NH}_4^+$ , and then calcined at about  $550^\circ\text{C}$  for two hours, so it is possible to remove ammonium and only protons remain inside the structure.



Catalytic activity depends not only on Brønsted acidity but also on: 1- electrostatic field gradient which acts as a Lewis acid to polarise a bond in an adsorbed molecule, 2- the interaction with metallic clusters. None of these processes act alone. Whatever the mechanism, adsorbed molecules are under the influence of a variable crystalline field. Interaction between cations and the framework increase the molecule occupancy time inside the cavities, and increase the possibilities of a reaction occurring. In this way an electrostatic field is generated inside the

cavities which can be strong enough to produce an ionisation of C-H bonds in the adsorbed molecules.

A zeolite can have a strong and localised electrostatic field ( $10^{-9}$  Vm<sup>-1</sup>, Lamberti et al., 1999), which can modify the electronic configuration of extraframework cations and make these cations active for catalysis. The nature of the final products in a catalytic process can be affected by zeolite porosity. In fact, the porosity controls the diffusion coefficient of the molecular species hosted inside the zeolite cavities.

The possibility of incorporating metallic atoms inside the framework or the extraframework, increases the possibility of catalysis. New catalytic reactions can be obtained by inserting metallic species (metallic clusters) obtained by reducing the zeolites which contain transition metallic ions, such as Ni<sup>2+</sup> e Pt<sup>2+</sup>.

## **2.1) INTRODUCTION**

In ambient conditions, the structure of zeolites (i.e.: framework, exchangeable cations, water molecules) is a system which is in equilibrium with the environment. When temperatures increase, or external pressure decreases, water molecules are expelled from the zeolitic system, which can thus, reach new equilibrium conditions. The study of the thermal behaviour of zeolites is very important since the most important properties of zeolites, such as catalytic activity, adsorption capacity, and their ability to act as molecular sieves appear when zeolites are in their anhydrous form. Zeolites, and in particular zeolites in their acid form, are widely used in catalysts in various chemical and petrochemical industrial reactions. These kind of processes, such as hydrocarbon cracking (which converts hydrocarbons into the lightest paraffins and alkanes) require quite high temperatures.

The dehydration process is very complicated, and varies from zeolite to zeolite, so thermal behaviour is not so easy to foresee.

## **2.2) HISTORY OF THE STUDY OF THE THERMAL BEHAVIOUR OF ZEOLITES**

The study of the thermal behaviour of zeolites started in 18<sup>th</sup> century, when, in 1756, Cronsted found that zeolites when heated seemed to “boil” (so he decided to call these minerals zeolites, which means “boiling stones”).

In 1840, Damou discovered that dehydration in zeolites was a reversible process, and that calcinations did not change their topology.

In 1890, Rinne demonstrated experimentally that natrolite, when heated, transformed into a new phase, called “metanatrolite”. The new phase, when exposed to air, adsorbed lost water and was re-converted into natrolite.

In 1896, Friedel hypothesised the “sponge-like” structure of zeolites, after some experiments on the adsorption of different fluids in zeolites.

In 1932, Rinne found that heulandite when heated to 350°C transforms into a new polymorph, and, when its temperature decreases, it transforms into a new and more stable phase.

The most common method used to study zeolite thermal behaviour and their dehydration process was thermogravimetric analysis (TG, DTG) and differential thermal analysis (DTA). More in-depth studies began during the 70s, with the first experiment based on structural analysis from data collected by single crystal “ex-situ” XRD. During these experiments the sample was dehydrated in a vacuum at a selected temperature, and then data were collected by single crystal diffraction, performed at room temperature after the sample was sealed in a glass capillary. In this way the data collection was performed very near to equilibrium conditions. This treatment presented a disadvantage: it was not possible to discriminate between the temperature and the vacuum effects

on the dehydration process. Besides, the mosaicity of the samples increased during the heating process, so the number of heating cycles that could be done on the crystal were very limited.

In recent years these problems have been overcome by using “in-situ” dehydration methods, thanks to time resolved data collection on powder or single crystal samples (using CCD or Image Plate detector systems and/or synchrotron sources). The advantage of this method is that it is possible to have faster data collection (that is to say, in “far from equilibrium” conditions), so it is possible to have a continuous picture of the dehydration process and thus, by using a powder sample, it is possible to avoid the problem of the limited number of snapshots available during the heating process.

### **2.3) CLASSIFICATION OF ZEOLITES BASED ON THEIR THERMAL BEHAVIOUR**

On the basis of the results obtained by thermogravimetric analysis, Breck (1974) decided to classify zeolites in two groups:

- 1) zeolites that, when dehydrated, do not show important structural changes. The dehydration curves of these zeolites show a fairly linear and continuous trend as temperature increases;
- 2) zeolites that, when heated, undergo important structural changes. Their dehydration curves show discontinuities and steps when temperatures increase.

Alberti and Vezzalini (1984) and Bish and Carey (2001), classified zeolites on the basis of their thermal behaviour, starting from dehydration-induced structural changes on the framework into the following groups:

- 1) zeolites in which dehydration is a reversible process. Dehydration is accompanied by a rearrangement of extraframework cations and water molecules, and there are no important modifications in the framework or cell volume (for example mordenite);
- 2) zeolites in which dehydration is a reversible process, but is accompanied by a large distortion of the framework and an important decrease in volume cell (for example: clinoptilolite);
- 3) zeolites in which dehydration is a partially reversible process, accompanied by important modifications in the framework due to T-O-T bond breakage, the migration of framework cations towards new positions and the formation of new T-O-T bonds. As the dehydration process proceeds, these zeolites recrystallize into new and more stable phases (for example: barrerite, stilbite and stellerite).

Category #	Material	Framework type
<b>1</b>	Mordenite	(MOR)
	Boggsite	(BOG)
	Bikitaite	(BIK)
	Ferrierite	(FER)
	Chabazite	(CHA)
<b>2</b>	Epistilbite	(EPI)
	Clinoptinolite	(HEU)
<b>3</b>	Heulandite	(HEU)
	Brewsterite	(BRE)
	Stilbite	(STI)
	Stellerite	(STI)

Table 3: Classification of Alberti and Vezzalini (1984): some example of zeolites for the three groups

Baur (1992) divided zeolites on the basis of framework flexibility:

- 1) inflexible frameworks, which are quite rigid and do not show important structural modifications when heated, whatever their chemical composition;
- 2) flexible frameworks, which in turn are divided into the following groups:
  - 2.1) collapsible frameworks, in which hinges co-rotate, and distortion of the framework is enhanced (for example, all T-O-T bonds in heated natrolite show variations in the same direction);
  - 2.2) non-collapsible frameworks, in which T-O-T hinges antirotate, so compression at one hinge needs tension at another hinge and vice versa. Unit cell variations in this case are modest (for example, in zeolite A, all T-O-T angles rotate in opposite directions, thus compensating for the distortion effects).

It is, nevertheless, interesting to note that some zeolites can show different thermal behaviour depending on the thermal conditions (temperature of heating, time of heating, time elapsed after heating, data collected in near equilibrium conditions or far from equilibrium conditions).

For example, brewsterite, when heated under vacuum conditions and analysed by ex-situ analysis on single crystal, shows almost complete dehydration, T-O-T bond breakage inside the 4-ring of the cage and T cation migration towards a new site (face-sharing tetrahedra process), then a subsequent T cation migration towards a new fivefold coordinated site. If the same sample is heated and then collected by in-situ powder diffraction, no T-O-T breakage is observed (\*)

According to Cruciani (2006), the definition of a parameter which can quantify the thermal stability of zeolites is useful. An empirical Stability Index (SI) was introduced considering the collapse/breakdown temperature (determined by X-ray measurements), the maximum volume contraction and the presence of phase transformations. The correlation between the stability

index and the Si/Al ratio confirmed the importance of the latter ratio in controlling the thermal stability of zeolites. Cruciani (2006) observed that: (i) zeolites with  $\text{Si/Al} \geq 3.80$  are very stable; (ii) zeolites with  $\text{Si/Al} \leq 1.28$  are fairly unstable; and (iii) zeolite stability in the intermediate Si/Al range cannot be directly predicted from the Si/Al ratio. In the present study, the inverse relationship between thermal stability and ionic potential,  $(Z/r)_{\text{wt}}$ , was also confirmed: (i) zeolites with  $(Z/r)_{\text{wt}} < 0.072$  are very stable; (ii) those with  $(Z/r)_{\text{wt}} > 0.187$  are unstable, but (iii) the  $(Z/r)_{\text{wt}}$  ratio does not allow discrimination within an intermediate range.

## 2.5) MODIFICATIONS INDUCED BY HEATING

As seen in the first chapter, at ambient conditions zeolites are characterized by a 3D tetrahedra structure (framework) with Si or Al at the centre, and channel and cages which host extraframework cations and water molecules.

When heated, zeolites can show:

- 1) a decrease in cell volume due to the loss of water molecules and/or templating organic molecules (this is the dehydration or calcinations process). The maximum cell volume contraction with respect to the largest cell volume measured during heating is given by  $\Delta V_{\text{max}}(\%)$ . It is usually given by the volume at the end of the dehydration process, but there are some exceptions (for example yugawaralite, wairakite and bikitaite);
- 2) migration of extraframework cations. Extraframework cations, partially or completely coordinated.

Under heating conditions, extraframework cations, partially or completely coordinated to water molecules, tend to change their coordination sites, and usually, weakly polarized cations migrate towards framework oxygens after the loss of water molecules.

Framework deformation after cation migration depends on the nature of exchangeable cations and framework topology;

- 3) negative thermal expansion (NTE), which is defined as the reversible contraction of unit cell dimensions upon heating. Depending on whether the contraction occurs in three or only in one or two dimensions, the NTE can be isotropic (in the case of amorphous or cubic materials) or anisotropic (materials whose cell volume increases with temperature).
- 4) phase transitions of phase transformations (displacive or reconstructive) which lead to more or less metastable phase(s);
- 5) T-O-T bond breakage and the formation of new bonds due to a “*face sharing tetrahedral*” process. During this process oxygen bridges are broken and there is migration by the T cations to new tetrahedral sites which still maintain three vertices as before, the fourth vertex being an oxygen, when it is shared by two tetrahedra, or an hydroxyl, when it is unshared. This mechanism is described by (Taylor, 1960) as an Si migration from an initially full tetrahedric site to an initially empty tetrahedric site. These two tetrahedra have been defined by Alberti and Vezzalini (1984) as “face sharing tetrahedra” (Figure 10);

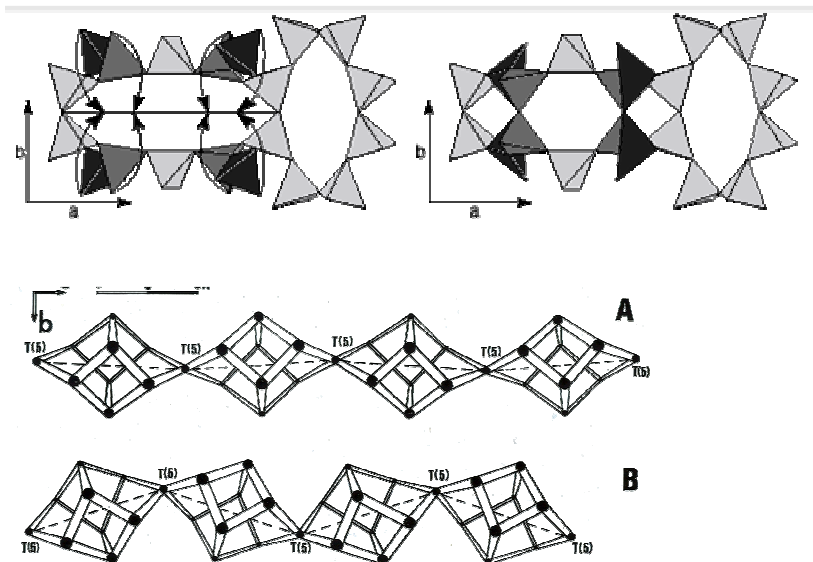


Figure 10: face sharing tetrahedra

- 6) if heat-induced modifications are significantly great, they can cause the collapse of the structure or its amorphization. Bish and Carey (2001) have illustrated two kinds of discontinuous processes: structural collapse (T-O-T bridges are broken, but it is still possible to recognise the framework structure by X ray diffraction and zeolites retain some sorption properties) and structural breakdown (which leads to complete amorphization, i.e. the loss of structure in zeolites, and consequently the loss of adsorption properties). Although these two terms indicate two different processes, they are very often used to indicate the same thing, i.e. structural destruction.

## 2.4) FACTORS GOVERNING THE THERMAL BEHAVIOUR OF ZEOLITES

Thermal stability of zeolites depends on many factors, such as:

- 1) Si/Al (or Si/(Si+AL)) ratio. Thermal stability increases with the Si/Al ratio. This depends on the fact that energy for Si-O bond breakage is greater than the energy required to break an Al-O bond. So, zeolites with a higher Si/Al ratio (more hydrophobic) are expected to show lower dehydration temperatures. This is not a general rule, in fact some zeolites with a low Si/Al ratio (merlinoite, laumontite, bikitaite, analcime and chabazite) show more stable thermal behaviour than higher Si/Al zeolites (tschernichite, heulandite, barrerite and brewsterite).
- 2) Si/Al ordering in the framework for a fixed Si/Al ratio. Many studies have demonstrated that the location of extraframework cations in zeolites after dehydration is affected by Al distribution in the tetrahedral sites, so it is easy to hypothesise a correlation between framework oxygens bonded to cations in dehydrated forms and framework oxygens bonded to protons in acid form (Alberti et al., 2001). Starting from the assumption that these oxygens have weak bonds with respect to T cations and/or strong bonds with respect to

extraframework cations, some authors have hypothesised a connection between thermal stability and Si/Al ordering. For example, Armbruster (1993) demonstrated that in all heulandite-clinoptilolite one of the tetrahedral sites is enriched in Al, thus leading to a weaker bond with one of the oxygens. This can explain the strong interaction between these oxygens and Ca ions in dehydrated structures, and this could be a clue to understanding the differences between heulandite and clinoptilolite. Furthermore, it has been observed (Cruciani et al., 2001) that epistilbite, when dehydrated, shows the largest deformation in those T-O-T angles which show greater Al enrichment.

The nature and number of extraframework cations (McDaniel et al., 1976). There is a general consensus that zeolites containing monovalent alkali cations (e.g.  $K^+$ ,  $Na^+$ ) are generally more stable than those containing divalent cations (e.g.  $Ca^{2+}$ ) (Bish and Carey, 2001; Reisner et al., 2000). The example of natural zeolite chabazite in various cationic forms typifies the behaviour of other zeolites. Ionic potential or electrical charge density appears to be the most suitable parameter for quantifying the effects of charge-compensating cations on thermal stability. It is worth noting that specific effects which simply relate zeolite stability to cation size, irrespective of their charge, have been proposed. Some authors attribute a role in promoting zeolite resistance to collapse to the relative ability of various cations to fill the voids in the crystal after dehydration (a sort of “packing” effect).

In particular, larger cations prevent structural collapse (Koyama and Takeuchi, 1977), while on the contrary, small cations cannot keep channels expanded. Some results, contrasting with the above general trend of increasing thermal stability with ionic potential or size, have been reported. Furthermore, some exceptions to this rule have been reported, for example, Na-Y zeolites containing different RE cations collapse at higher temperatures with respect to those belonging to the parent Na-Y zeolite, and therefore, have improved stability. Thus, it has been demonstrated that the thermal stability of zeolites depends on both their RE content and nature (Trigueiro et al., 2002).

The coordination number of cations after dehydration is also an important factor in thermal stability. In fact, it has been demonstrated that a lower coordination number leads to lower thermal stability.

It is known that when the coordination of extraframework cations with water molecules is lost, they move towards the wall of the zeolite channel during the dehydration process, to form new bonds with framework oxygens. This displacement causes deformation in the zeolite structure, in particular in the T-O-T bridges. So, it is important to note that the coordination required by an ion could be of some importance in the thermal stability of a zeolite. For example, many studies have reported that some Ca-containing zeolites collapse when Ca coordination is lower than six (laumontite, epistilbite and gismondine) or seven (heulandite).

- 3) Framework topology is a very important factor in zeolite thermal stability. Zeolites with a high framework density (FD) have thicker walls between pores and channels, so they are more stable (McDaniel and Maher, 1976) (Tschaufeser and Parker, 1995) (Figure 10). Furthermore, zeolites characterised by regular shaped tetrahedral  $n$ -rings (and T-O-T

angles) are more stable than zeolites with distorted T-O-T, because in the latter the T-O-T angles are smaller and the Si/Al are not ordered within the T sites. Also the presence of five-membered ring channels (silicate ring relative energy is lower for five- or six-membered rings (Baur, 1992)) is of a certain importance. Some particular units or sub-units are also very important for thermal stability, for example columns of five-membered rings, or double six-membered rings, or double eight-membered rings (Baur, 1992; Smith, 1976) because channels with these sub-units become more rigid and are less affected by the heating effect. Another important factor is the connectivity, or flexibility, of the frameworks, in fact, non-collapsible frameworks are more stable than collapsible ones, in fact, the former should adsorb the strain induced by the displacement of extraframework cations during the heating process (Corà et al., 2003), but this is not a general rule.

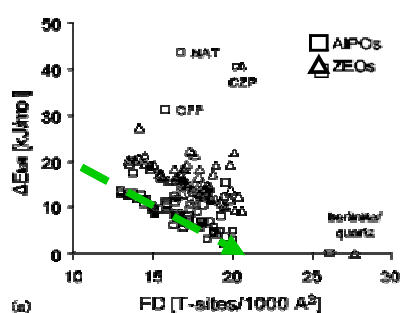


Figure 11: zeolite framework stability is predicted to increase with increasing FD (from Corà et al., 2003)

- 4) Extrinsic factors affect the temperature of decomposition. For example, the temperature at which water is lost depends on the modality of heating (dry or wet environments) and on the vapour water pressure (for example, Smith (1976) showed that the dehydration temperature of a zeolite at  $1 \times 10^5$  Pa water pressure is  $200^\circ\text{C}$  higher than in a dynamic vacuum). Partial  $\text{H}_2\text{O}$  pressure is also very important for reactions which occur during dehydration. For example, Van Reeuwijk (1974) showed that the transformation of natrolite into  $\alpha$ -metanattrolite occurs at different temperatures depending on the pressures ( $300^\circ\text{C}$  at low pressure and  $>450^\circ\text{C}$  at 5 bar)

Heating conditions are also an important factor. In fact, kinetic factors under isothermal or dynamic conditions affect the structural features of the final product. The heating process can be carried out near or far from equilibrium conditions, and zeolites can show different thermal behaviour depending on the heating modality. For example, in stellerite (Arletti et al., 2006) time-resolved study performed “in-situ” and with continuous heating in air gave contrasting results compared with the same zeolites collected by “ex-situ” single crystal, dehydrated under vacuum conditions and measured at ambient conditions. In fact, it is possible to observe the breakage of a T-O-T bridge in an “in-situ” study which cannot be observed in an “ex-situ” study. This also occurs for other zeolites, measured by “in-situ” or “ex-situ” techniques, such as stilbite (Cruciani et al., 1997) and brewsterite (Alberti et al., 1999; Ståhl and Hanson, 1999). For example, wairakite, shows different symmetry depending on continuous or stepwise heating (Seryotkin et al., 2002; Cruciani and Zanella, 2002).

### 3.1) INTRODUCTION

The aim of this work is to characterise zeolitic catalysts in non-ambient conditions starting from a structure analysis of diffraction data collected on powder or single crystals, using X-ray (conventional source or synchrotron radiation) or neutron diffraction. As already explained, a detailed structural characterisation can explain the efficiency of these microporous materials, their stability, as well as the different types of shape selectivity seen in a wide range of catalytic systems. A short overview of the experimental techniques (X-ray diffraction, neutron diffraction and thermal analyses) will be proposed in this chapter, with particular emphasis to their advantages and peculiarities.

### 3.2) SINGLE CRYSTAL X-RAY DIFFRACTION

The diffraction of monochromatic radiation from single crystals has been considered the best method for accurate crystal structure determination since the early days of X-ray crystallography. It is a very useful and precise tool, commonly used for the precise determination of a unit cell, including its dimensions and the position of its atoms within the lattice, its bond-lengths, angles and details of its site ordering. The goal of single crystal analysis is to obtain the structure factor  $F(h)$  value for a series of hkl reflections using scattering vector  $h$ . The structure amplitude  $|F(h)|$  is related to the integrated intensity of the diffracted beam while the crystal is rotated. In particular, by using synchrotron and neutron sources and applying correction factors it is possible to obtain very accurate  $F(h)|$  and  $|F(h)|^2$  measurements and thus, accurate  $I_{hkl}$  measurements.

Single-crystal diffractometers use either 3- or 4-circle goniometers. These circles make reference to the four angles ( $2\theta$ ,  $\chi$ ,  $\varphi$ , and  $\Omega$ ) that define the relationship between the crystal lattice, the incident ray and detector. The sample is glued onto a capillary and mounted on a goniometric head. In recent years, Kappa goniometers (Enraf-Nonius Corporation) have offered great accessibility to crystals at the expense of the weight that can be supported. The resolution function is the description of the 3D shape of the Bragg reflection in the instrument angles, in terms of instrumental parameters (incident beam divergence, wavelength dispersion, etc.) and sample characteristics such as size and mosaicity.

Modern single-crystal diffractometers use CCD (Charge-Coupled Device) technology to transform X-ray photons into an electrical signal which are then sent to a computer for processing.

Single-crystal diffraction is mainly used for the identification of new minerals, crystal solutions and refinement, the characterisation of ion coordination and variations in crystal lattices with chemistry. Thanks to specific instrumentation it is possible to solve structures at high pressure and/or temperature phases. The main advantage of this method is that it is not destructive and it is possible to obtain a detailed crystal structure. The main disadvantages are that for this kind of analysis a single, stable sample (of about 50—250 microns in size) is required. This is quite

difficult to find, even in natural or synthetic zeolites. Besides, the sample must not be twinned, should be optically clear, and data collection can take many hours.

While single crystal diffraction is the preferred method for determining structure and electronic density maps, the preparation of diffraction quality crystals often lags months or years behind pioneering scientific breakthroughs, such as high-temperature superconductivity. This is particularly true for many materials of major industrial or commercial importance, including zeolites, polymers, and pharmaceuticals, collectively known as small molecules, as well as many minerals. The ability of the synchrotron to produce intense, highly collimated X-radiation and to focus it with x-ray optics on a very small-sized spot enables single crystal diffraction to be performed on many of these materials where previously this was considered impossible.

### **3.3) X-RAY POWDER DIFFRACTION**

X-ray powder diffraction is a method which was developed in 1913 after the discovery of diffraction by crystals (Friedrich, 1913; Keene, 1913). Nowadays it is one of the most important techniques available to material scientists. However, one of its disadvantages is that, for many important crystalline solids it is difficult to grow a single crystal of sufficient size and quality to allow analysis by this method, while high-quality polycrystalline samples are often easier to obtain, leading to the choice of using powder diffraction patterns to determine crystal structures. Moreover, diffraction patterns of materials measured by X-ray powder diffraction are like fingerprints (in fact, every compound gives its own pattern), and powder diffraction provides information not only about the structure but also about the texture and morphology of the sample.

In addition, a great number of materials cannot be measured as single crystals, and powder diffraction is the only method to obtain information about these compounds. However, the information content in such patterns is significantly reduced in comparison with single crystal X-ray diffraction, and data problems can make solving a crystal structure difficult.

X-ray powder diffraction is an available option in studies on crystal structure behaviour under external conditions such as at high pressure, high or low temperature. X-ray radiation sources are usually vacuum tubes in which heated electrons are emitted from a cathode and are filed against an anode by an electric field. Generated X-rays usually have a wide spectrum of wavelengths, so a monochromator is necessary. The counting apparatus is composed of a detector (to convert the intensity of scattered X-rays into an electric signal) and a computing tool (to convert the signal into diffraction intensity values). The intensity of coherent X-ray diffraction depends on structural factors, the degree of crystallinity and volume, density and adsorption characteristics of the studied material, its incident beam characteristics, polarisation factors, etc. In this technique, a three dimensional diffraction pattern is collapsed into one dimension by spherical averaging. As a result, reflections which would otherwise be measured separately are caused to overlap. The resulting pattern is a collection of concentric rings, often with a fine-

structure derived from the individual crystallites in each ring. The resolution obtained from powder diffraction is limited by the extent of this overlap, the signal to background noise level and by the range of observations (d-range). Background noise can result from scattering by the cell or in the air.

In recent years several developments, such as the availability of high intensity and high collimation of synchrotron sources, the development of diffractometers interfaced to computers and the development of efficient data analysis methods, such as Rietveld refinements have been of great assistance in the experimental resolution of these overlaps. These features also reduce the signal to noise ratio, and can increase the range of observations. Powder diffraction techniques have become standard techniques for the identification of crystalline phases and for the determination of their volume fraction in mixed phases and also for solving problems regarding structure determination.

For a typical X-ray powder diffraction experiment, the scattering intensity  $I_h$  is obtained by integrating the diffraction profile of every reflection. Integrated intensities give important information about the crystal structure because they are proportional to structure factor  $|F(h)|^2$  which is directly related to the arrangement of atoms within the unit cell and proportional to the amount of diffracting material in the sample.

The most important powder diffraction applications are:

- 1) phase identification: this is one of the most common applications of the X-ray powder diffraction method because it requires only d-spacing and relative reflection intensity. It is carried out matching the measured diffraction pattern from an unknown material with patterns from single phase reference samples. This is usually performed in conjunction with databases of already measured powder patterns.
- 2) quantitative phase analysis: this method is based on the proportionality between the weight of a crystalline phase fraction in a mixture and the intensities of its diffraction lines.
- 3) structure determination: nowadays, this problem is no more considered the domain of the single crystal method. Different reflections for powder are thrown together in a single axis, and this leads to ambiguities in finding their individual positions and intensities but these problems have been overcome thanks to the development of the use of synchrotron radiation which has led to a reduction in the incidence of overlapping peaks.
- 4) structure refinements: once a structural model has been derived, the Rietveld method can be applied to refine the instrumental and structural parameters. If not all the atoms have been located during the structure determination stage, they can be located by using Fourier differences synthesis.
- 5) residual stress measurement: if a material is compressed, interplanar spacing is modified proportionally to the strength of the stress. The strain can be related to the peak shift ( $\Delta d/d = -\Delta 2\theta / 2 \tan \theta$ ), and residual strain can be transformed into residual stress using the elastic constant of the material.
- 6) texture measurement: this can be quantified by the crystalline orientation distribution function.

7) particle size and microstrain measurement.

For this PhD thesis, a Bruker D8 Advance diffractometer with a sol-x dispersive x-ray detector was used.

### 3.4) SYNCHROTRON RADIATION

In recent years, synchrotron radiation has become one of the most powerful and exhaustive methods for the study of the thermal behaviour of materials and for ab-initio structure resolution. Synchrotron radiation is the electromagnetic field emitted when relativistic accelerated charged particles (electrons or positrons) which are moving close to the speed of light, are forced to move along a circular path with the application of a static magnetic field perpendicular to the horizontal orbital plane. These relativistic particles have an energy value  $E = \gamma mc^2$  ( $\gamma > 1$  and  $m$ , represents the rest mass). For an electron or positron,  $mc^2 = 0.511 \text{ MeV}$  (Figure 12).

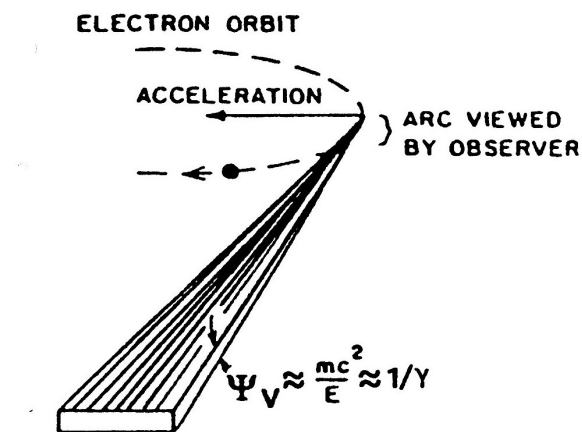


Figure 12: Radiation emission patter of relativistic electron ( $v/c \approx 1$ ) in circular motion (from Winick, 1981)

The polarisation of the radiation is very important since the beam emitted in the plane of the particle orbit is linearly polarised, while it is elliptically polarised when emitted from the plane. Electromagnetic radiation is emitted in a cone in the forward direction, at a tangent to the orbit of the charged particles.

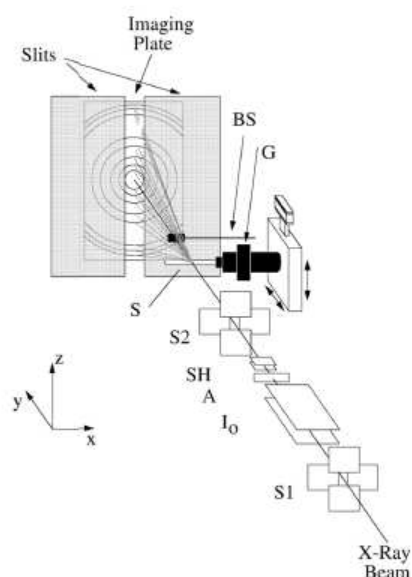
Compared to conventional sources, synchrotron radiation is brighter ( $10^4$  and  $10^{12}$  times), and it has a rather wide spectral range.

Thanks to the characteristics of synchrotron sources it is possible to obtain very high angular resolution ( $\Gamma < 0.01^\circ$ ) in terms of FWHM, so it is possible to remove errors due to sample shift and transparency (Cox et al. 1992, Klug & Alexander 1974).

Synchrotron light produced in this manner possesses a number of unique properties:

- a) patterns collected have a high intensity and a very high resolution (in terms of Bragg's peak separation);
- b) the increased brightness leads to data collection which is increased by several orders of magnitude, and this is the basis for time-resolved studies;
- c) it is possible to obtain a better signal/noise ratio, and consequently, to also detect very weak peaks at low angles, which are important for the determination of the unit cell parameters (Hriljac et al. 1991);
- d) diffraction peak profiling is easier to describe than those collected using laboratory sources
- e) it is possible to obtain small radiation axial divergence (which is polarised in the synchrotron's orbit);
- f) linear and area detectors with a large dynamic range have some advantages, as they allow faster scanning (very useful above all in the case of transient processes) of the reciprocal space, make the whole powder spectrum available for each sample orientation and show a low noise floor, leading to greater detection sensitivity. Furthermore, by recording a large portion of the ring, it is possible to obtain a better average upon integration.

Recent improvements in imaging plates (IP) and CCD detectors technology (Thoms *et al.* 1998) and CCD have been very useful for solving the problem of faster scanning. The pattern is recorded continuously behind a slit and then the data are processed after the reaction is complete (Norby 1996, 1997b).



- S1: the resolution slit system (vertical and horizontal) (spot size defined at a resolution of  $\pm 25\mu$ )
- Io: the ionisation chamber (monitors the effective photon flux on the sample)
- A: the absorber (reduces the beam intensity)
- SH: the rotating shutter (regulates the exposure time of the IP)
- S2: anti-scattering slit system (to reduce the diffuse background due to air scattering)
- S: sample
- BS: beam stopper
- G: rotating/oscillating goniometer heads

Figure 13: the IP camera set-up installed in the second experimental hutch of the GILDA beamline (from Meneghini et al., Multipurpose imaging-plate camera for in-situ powder XRD at the GILDA beamline)

The translating imaging-plate technique is made up of a linear slit which selects a narrow portion of the Debye rings while the recording plate linearly translates behind the slits at a

constant speed allowing the accumulation of a continuous diffraction pattern as a function of time. In such a way, it is possible to probe the evolution of the sample structure as a function of time and/or environmental conditions.

The very high quality of results obtained by synchrotron data collection permits the performance of full-profile Rietveld structural refinements. To create images of or detect fine structures, the wavelength of the illuminating radiation must be of the same order as the structure. Synchrotron light is able to span the electromagnetic spectrum across almost all fields of scientific interest, from life-size imaging down to nanoscale, molecular and atomic length scales. This method is also very important because it enables the possibility of collecting so-called time-resolved data. Using synchrotron radiation it is possible to observe all structural modification induced by heating the sample in real time, and the structural changes are directly probed in selected conditions, making no assumptions in terms of the preservation of the structural properties on the sample treatment. Time resolved dynamic studies are measurements performed in non-ambient conditions. They consist in bringing a sample into a non-equilibrium state by applying external perturbation, such as a gradient of pressure or temperature and then collecting the diffraction patterns at determined intervals which correspond to the response of this perturbation. During these measurements, the data collection is faster than the rate of heat/pressure-induced transformations in the sample. Thanks to this experimental configuration, the development of the reactions can be studied in detail (Figure 14). It is important to note that for dynamic studies the detection time has to be shorter than the time scale of the process, and sometimes, especially for very fast reactions, data may show signal recording problems and poor counting statistics, so the use of linear area detectors and brilliant incident radiation beams becomes of essential importance. The main phenomena which can be studied by in-situ time-resolved analysis are reconstructive phase transitions, chemical reactions, temperature/pressure induced phase transitions and crystallisation.

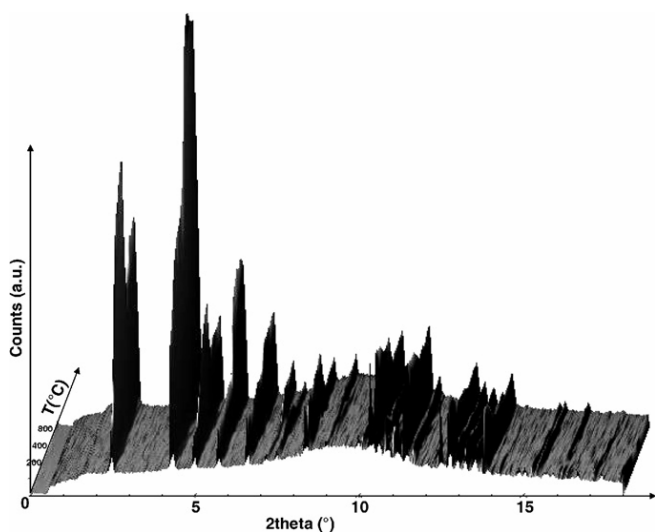


Figure 14: An example of time-resolved data collection: the evolution of the XRPD patterns in the 3–18°  $2\theta$  interval as a function of the temperature (30–830°C) in the omega zeolite (Martucci et. Al., 2007)

### 3.5) NEUTRON DIFFRACTION

Neutron diffraction is a powerful method for investigating zeolites structures, and in many cases it can be an excellent complement to X-ray diffraction.

The advantage of neutron over X-ray diffraction is due to its different interaction with matter.

In fact, while X-rays are scattered by the electrons in atoms, neutrons are scattered by its nucleus. As far as concerns X-ray diffraction, one of the most significant disadvantages is that the scattering power of these types of radiation strongly depends on their atomic number, i.e. on the number of  $Z$  electrons (in fact, scattered intensity for X-ray diffraction is strongly dependant on  $Z^2$ ). The atomic scattering factor for a  $j$  atom  $f_j$ , is proportional to  $Z_j$ . For this reason, X-ray techniques cannot localise light atoms (low atomic number leads to a low scattering power) and cannot distinguish between atoms with similar atomic numbers (for example, Si and Al in tetrahedral sites). Furthermore, the scattering power decreases very quickly ( $\sin\theta/\lambda$ ), and so, diffraction intensity is low at high angles.

On the contrary, for neutron diffraction, scattering power depends on the properties of the scattering nucleus, and does not vary monotonically with  $Z$  (Figure 15 and 16). On the contrary, it takes place according to the nature and number of the scattering nuclei. Furthermore, the scattering tends to increase with  $Z$ , but shows many oscillations between atoms which are near to one another and also between isotopes of the same element.

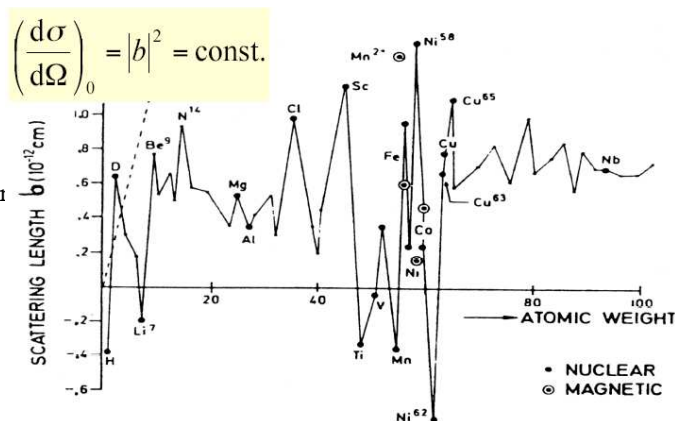


Figure 15: neutron scattering length for  $1$  as a function of atomic number

	X-rays $f_{\vec{q}} = 0 \equiv Z$	Neutrons		
		$b$ f(m)	$\rho^{coh}$ (bams)	$\rho^{tot}$ (bams)
hydrogen	1	-3.8	1.8	82
deuterium	1	6.5	5.4	7.6
carbon	6	6.6	5.5	5.5
nitrogen	7	9.4	11	11.4
oxygen	8	5.8	4.2	4.24
sulphur	16	3.1	1.2	1.2
iron	26	9.6	11.4	11.8

Figure 16: variations of the coherent cross section or the scattering length for neutrons (not monotonic with  $Z$  and smaller than the corresponding variation for  $f$ )

The most significant advantages of neutron diffraction are:

- 1) the characterisation of atoms with a low  $Z$  value which present only a small contribution in terms of electron density, such as hydrogen, is simpler;
- 2) atoms with similar  $Z$  values have different scattering cross sections;
- 3) scattering depends on the nucleus of atoms, so it is possible to discriminate between different isotopes of the same atom and therefore, it is possible to find isotopic substitutions;
- 4) there is no fall-off at high angles, so structural solution at high resolutions is possible
- 5) due to the absence of any long interactions, neutrons have very little adsorption, so they can penetrate deeply (usually in the order of cm) into the matter, and this is very important when heavy atoms are studied;
- 6) neutron diffraction can see the position of the nuclei of atoms, while X-rays can only see the electronic cloud surrounding the atom, so they provide complementary information;
- 7) thanks to the combined use of neutron and X-ray diffraction, it is possible to obtain very detailed pictures of molecular structures.

So, neutron diffraction is widely used for the study of zeolitic structures, microporous materials and other inorganic compounds, and, if combined with X-ray diffraction, is a powerful tool for exploring mineral structures. In fact, X-rays are employed for ab-initio resolutions, while neutron diffraction is used in order to locate hydrogen and light atoms in structures which have already been partially mapped. besides it is used to know Si, Al ordering inside the tetrahedric sites, in order to localise water molecules and extraframework cations in channels and cages with good detail and, above all, in order to localise protons bonded to framework oxygens.

During a typical neutron experiment, the sample is irradiated with neutron fluxes and then spatial distribution and/or scattered neutrons energy variations are measured.

There are two types of neutron sources (Figure 17):

- 1) (fission) reactors. They are “steady-state” sources. Neutrons are produced by the fission of an enriched material, such as  $^{235}\text{U}$ . During fission reaction, a thermal neutron is adsorbed by a  $^{235}\text{U}$  nucleus. The nucleus becomes highly excited and splits into a few fission fragments (medium-heavy elements) and 2-5 fast neutrons. On average, each reaction gives 2.5 neutrons, of which 1.5 are needed to keep the chain reaction going.
- 2) spallation. Neutron production is due to a dynamic process, based on a particle accelerator and not on a static reactor. Charged particles (protons) are accelerated to high velocities before being fired at heavy metal targets. The impact induces processes that produce many particle types, such as protons, pions, muons, and about 20 neutrons per incident proton, which are mainly released by evaporation. The main differences between spallation sources and reactors are that the spallation target is more concentrated than the reactor core, thus yielding higher flux and is normally pulsed and leading to a peak flux equivalent to a high-flux reactor.

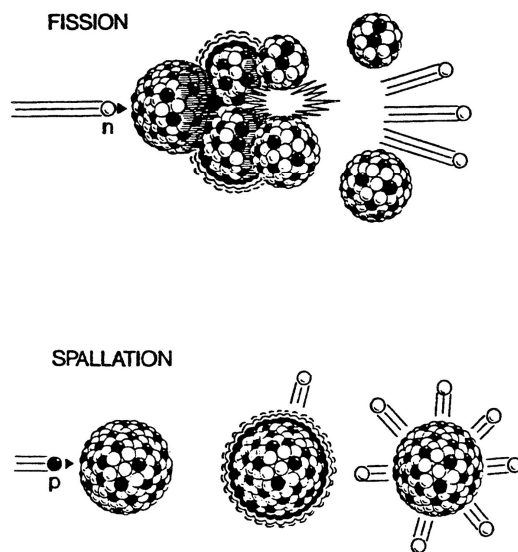


Figure 17: Production of neutrons: fission reaction and spallation source

The reason that neutron diffraction has been used so often for this thesis is that, by using neutron radiation it was possible to localise protons bonded to framework oxygens in activated zeolites. In fact, neutron diffraction is the most direct experimental method used to probe Brønsted acid siting since only with this kind of radiation is it possible to obtain significant effects on diffracted intensities using hydrogen nuclei. Deuterium is the isotope which is usually used in these experiments since it has a large coherent scattering cross section and tolerably small incoherent scattering cross section.

Furthermore, thanks to this method, it was possible to study the interactions of acid sites with water molecules inside zeolites structures, and to prove whether acid strength remained high after the rehydration process.

For this PhD thesis, data were collected at the ILL neutron sources in Grenoble, at the D2B line (Figure 18). At this line the polychromatic beam from the thermal beam H11 is collimated and diffracted by monochromator at a large take-off angle to obtain high resolution. Bragg reflections are measured by a bank of 64 detectors. The detectors are moved so that counts are averaged over several detectors. The diffractometer D2B is characterised by a very high take-off angle ( $135^\circ$ ) for such a monochromator. It is 300 mm high, focusing vertically at about 50 mm; this large incident vertical divergence is matched by 200 mm high detectors and collimators. A complete diffraction pattern is obtained after about 100 steps of  $0.025^\circ$  in  $2\theta$ , since the 64 detectors are spaced at  $2.5^\circ$  intervals.

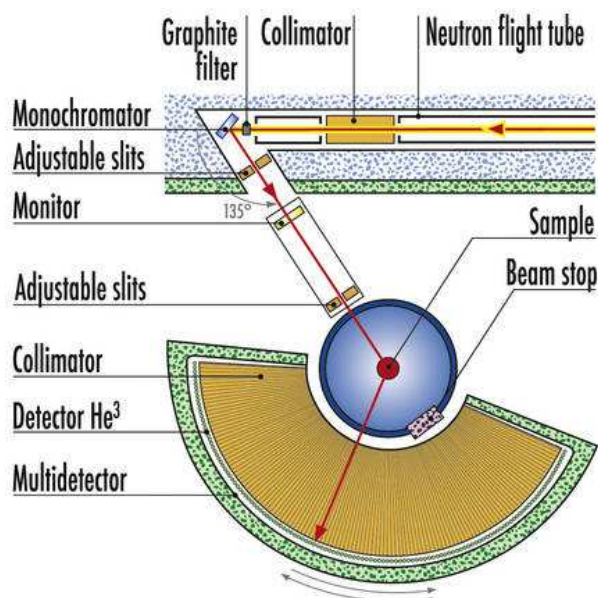


Figure 18: the High-resolution two-axis diffractometer D2B at the ILL line.

### 3.6) THERMAL ANALYSIS

Thermogravimetric analysis (TG, DTG) and thermal analysis (DTA) were the first methods used in the early studies on the thermal behaviour of zeolites.

According to the ICTA, International Confederation for Thermal Analysis, (ASTM 473-85), the definition of thermal analysis is a “Group of techniques based on the measurement of a physical property of a substance in function of the temperature (or time) during a controlled temperature program (heating, cooling, isotherm)”.

The temperature program can have heating or cooling phases, or a constant temperature (isotherm), or a combination of the above. The results of the measurements produce a so-called “thermal analysis curve”, and the features of this curve (such as peaks, discontinuities, slope changes ) are related to the thermal events which occur in the sample.

The principal applications for these techniques are: the detection of chemical-physical transformations in the material during thermal treatment, the evaluation of decomposition processes, the determination of enthalpy and specific heat values and the study of reaction kinetics and mechanisms.

During a specific reaction, the heat exchanged between the system and the ambient is the system enthalpy ( $\Delta H$ ) variation. By convention, when  $\Delta H < 0$ , the heat moves from the system to the ambient and the reaction can be defined as “exothermic”.

The most important exo/endothemic reactions are shown in Table 4:

Endothermic reactions	Exothermic reactions
Melting	Adsorption
Dehydration	Crystallisation
Polymorphic reactions	Oxidation
Sublimation	
Evaporation	
Structural modifications	

Table 4: exo-endothermic reaction

Thanks to thermal analysis is it possible to:

- 1) evaluate the effects on materials on the basis of working conditions;
- 2) study the loss of water during the dehydration process;
- 3) follow chemical-physical modifications induced by heating;
- 4) determine the amount of chemical species lost during the heating process.

There are two different methods for carrying out thermal analysis:

- a) isothermal methods: the sample is heated to a given temperature until no further weight loss, then heated to a higher temperature until no further weight loss, and so on
- b) dynamic method: the sample is heated at a constant rate and the weight loss is monitored continuously

Usually, the thermal gradient used for thermal analysis is 5-10°C/min.

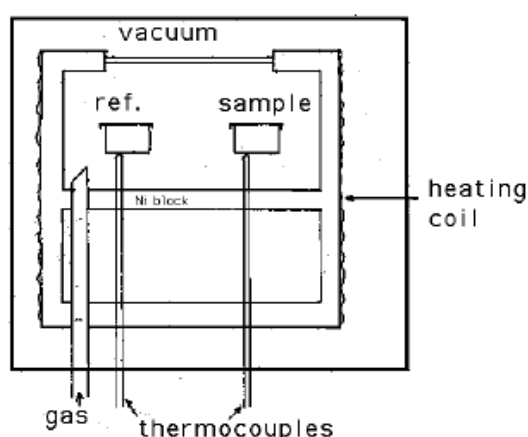


Figure 19: schematic illustration of a DTA cell

A straightforward measurement for zeolite thermal stability has been recorded as the temperature of the first exothermal peak on the DTA curve. In the assumption of this peak as marking the zeolite breakdown, its exothermal character might appear anomalous, compared to the typical endothermal nature of crystalline material decomposition; a possible explanation is

given by the large free surface energy that is released during the zeolite amorphisation process (Breck, 1974). The exothermal peak on the DTA curve has been applied, for instance, to establish the influence of both the nature and content of rare earth (RE) cations on the thermal stability and textural properties of a faujasite-type zeolite (NaY) (Trigueiro et al., 2002). However, in Ba-exchanged zeolites which share the same faujasite-type framework (X, LSX), the first DTA exothermal peak is interpreted as a result of the crystallisation of hexacelsian from the amorphous phase formed after the zeolite breakdown (Esposito et al., 2004). This suggests that the assignment of the DTA exothermal peak to zeolite breakdown cannot be taken for granted without parallel X-ray data. Moreover, many zeolites do not even show the exothermal peak associated upon amorphisation (Figure 20).

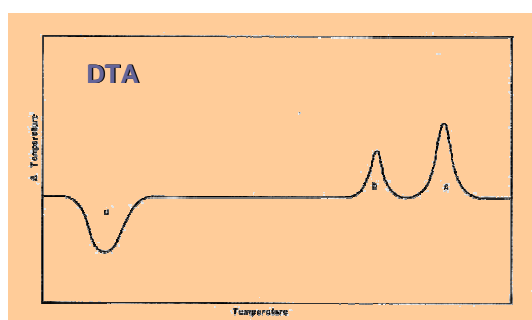


Figure 20: a typical DTA analysis:  
1st endotherm(s): evolution of water and other volatile species, if present;  
1st exotherm: collapse of the crystalline zeolite to amorphous phase;  
2nd exotherm: recrystallisation to a new phase.

The dehydration and amorphisation/recrystallisation temperatures are typically evaluated using the endothermic and exothermic peaks on the DTA curves, respectively.

For this PhD thesis, a STA 409 PC Luxx thermobalance, designed for simultaneous TG-DTA measurements was used. The TG, TG-DTA sample carriers are equipped with a thermocouple to directly measure the temperature at the sample/reference crucible (DTA).

#### 4.1) TSCHERNICHITE AND ZEOLITE BETA: STRUCTURAL AND CHEMICAL FEATURES

In the last ten years, the Antarctic region has been the focus of several mineralogical papers concerning both the discovery of a group of new and very rare natural zeolites such as mutinaite and gottardiite, respectively, at Mt. Adamson in the Giurassic Ferrar Dolerite (Vezzalini et al., 1997; Alberti et al., 1996) and the occurrence of tschernichite (Galli et al., 1995), a Ca-rich zeolite whose framework topology has been proposed as being related to that of synthetic zeolite beta (Smith et al, 1991).

Zeolite beta, firstly described by the Mobile Oil Corporation (Wadlinger et al., 1967), is a large-pore, high-silica zeolite which is synthesised using tetraethylammonium (TEA) as a structure directing agent. Its peculiar pore structure and high acidity makes this material a very active and selective catalyst for a wide spectrum of reactions of industrial importance, such as the alkylation (Bellussi et al, 1995; Perego et al, 1996), acylation (Hoefnagel and van Bekkum, 1993; Kouwenhoven et al, 1996), disproportionation, and transalkylation (Das et al., 1994; Wang et al., 1990) of aromatics, as well as the alkylation (De Jong et al., 1997; Nivarthi et al., 2000), cracking (Boretto et al., 1992) and isomerisation (Lee ad Rhee, 1997; Wang et al, 2005) of paraffins, etc.

The framework structure of zeolite beta (structural code BEA) was resolved independently by Newsam et al. (1998) and Higgins et al. (1988) using a combination of various techniques, from model building to DLS refinement, high resolution electron microscopy imaging, electron diffraction, X-ray powder diffraction, and X-ray powder pattern simulation.

The authors showed that the peculiar diffraction pattern of this material was characterised by a set of sharp reflections at  $h = 3n$  and  $k = 3n$ , and a set of diffuse maxima for  $h \neq 3n$  or  $k \neq 3n$ , frequently superimposed on continuous streaks parallel to  $c^*$ , pointing to a disordered structure in the normal direction (001), with disorder due to  $\pm a/3$  and  $\pm b/3$  displacements in the (001) plane. Both groups of authors agreed that the structure of zeolite beta could be described as a disordered sequence of different polytypes with frequent planar faults: polytype A, which is tetragonal with space group  $P4_122$  (or  $P4_322$ ) and cell parameters  $a = b \approx 12.5 \text{ \AA}$  and  $c \approx 26.4 \text{ \AA}$ , and polytype B, which is monoclinic with space group  $C2/c$  and cell parameters  $a \approx b \approx 17.6 \text{ \AA}$ ,  $c \approx 14.4 \text{ \AA}$  and  $\beta \approx 114^\circ$  (Newsam et al. 1998; Higgins et al. (1988). Both polytypes can be described as consisting of tetragonal layer-like building units. According to the OD theory, these two structures represent the two maximum degrees of order (MDO) topologies.

According to Higgins et al. (1988) a third polytype, called polytype C, was also suggested. It is monoclinic with space group  $P2/c$  and with  $a \approx b \approx 12.5 \text{ \AA}$ ,  $c \approx 27.6 \text{ \AA}$ , and  $\beta \approx 107^\circ$ .

The natural counterpart of synthetic zeolite beta, known as tschernichite, was discovered at Goble, Oregon, and described by Smith et al. (1991) and Boggs et al. (1993). The occurrence of the structure-type of zeolite beta in a natural phase is extremely important, since it implies, as correctly proposed by the authors, that an organic template may not be necessary for synthesis. Smith et al. [1991] stated that tschernichite consists in the intergrowth of polytype A and B.

The authors observed that “tschernichite patterns match best with computed X-ray patterns for an approximately equal amount of the A and B arrangements in a random sequence”, where A and B refer to polytypic forms. They also observed that the mineral occurred in large (tetragonal dipramids terminating in a basal pinacoid up to 0.6 x 0.6 x 1.2 mm in size,) and small (radiating hemispherical groups) crystals (Alberti et al., 2002). The second finding of this mineral was in the Jurassic Ferrar Dolerite at Mt. Adamson, in Northern Victoria Land, Antarctica (Galli et al., 1995). Also in this case, tschernichite shows two types of larger and smaller crystals.

Microprobe chemical analyses (Galli et al., 1995) showed that the two samples have different Si/Al ratios (2.66 for large crystals, 3.94 for small crystals) as was shown for the tschernichite found at Goble. The chemical analysis performed revealed a higher silica content in the smaller crystals than in the larger ones, “probably as a result of differing conditions during their formation”. It is easy to suppose that these differences in morphology and chemistry are related to the different, monoclinic and tetragonal, polytypes which are highly intergrown in synthetic beta.

Synthetic procession images obtained by X-ray single crystal diffraction data were interpreted by Alberti et al. (2002) with the help of OD theory, which allowed ambiguities to be overcome regarding symmetry assignment. Larger crystals are characterised by the dominant presence of monoclinic polytypes, while smaller crystals are dominated by a greater prevalence of tetragonal polytypes. Both structures were refined and their structural features, in particular the location and coordination of the extraframework cations were assigned (Alberti et al., 2002).

The tetragonal Periodic Building Unit (PerBU) is called a beta layer (Figures 21 and 22). It is composed of T16 units built up by four fused 6-rings or eight fused 5-rings related by translation along *a* and *b*.

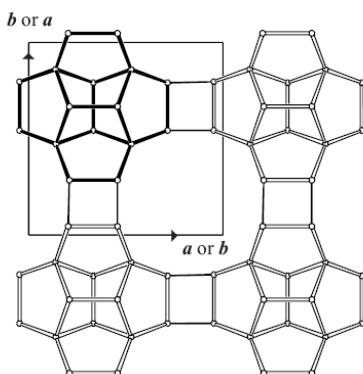


Figure 21: PerBU viewed along the normal *c* plane

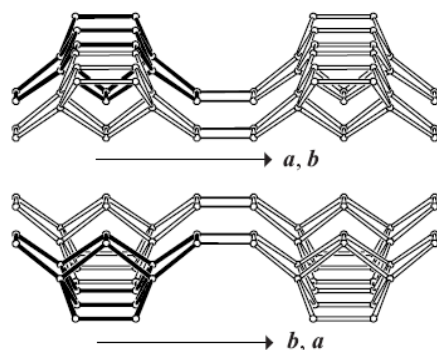


Figure 22: PerBU viewed along *b* (or *a*) (top right), and along *a* (or *b*) (bottom right). The depicted PerBUs on the right are related by a rotation of 90° around *c*.

The structure can be described as the repetition of three composite building units, as shown in Figure 23.

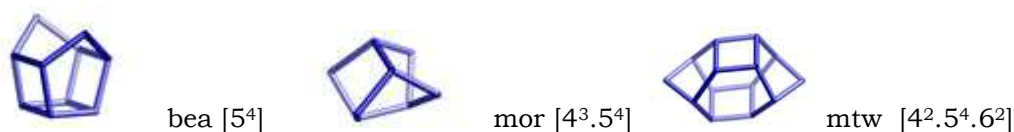


Figure 23: Composite Building Unites in BEA

According to the OD theory, these two structures represent the two maximum degrees of order (MDO) topologies.

Neighbouring PBUs, related by a mirror operation, can be connected along [001] via O bridges in three different ways (Figure 24):

- a) the lateral shift in the top layer along  $a$  or  $b$  is zero
- b) the lateral shift in the top layer is  $1/3 a$  or  $1/3 b$
- c) the lateral shift in the top layer is  $-1/3 a$  or  $-1/3 b$

Once the distribution of the lateral shifts between the layers stacked along [001] is known, the 3-D structure is defined.

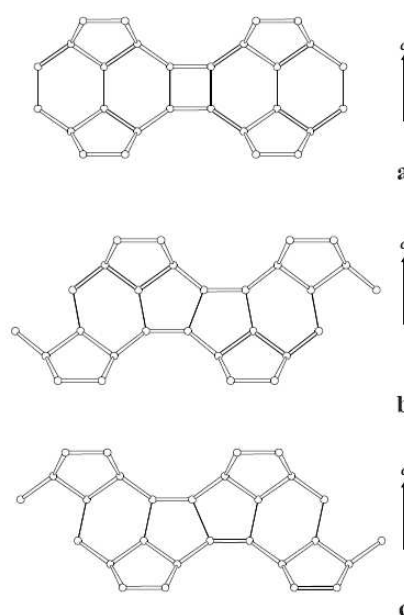


Figure 24

## 4.2) EXPERIMENTAL

### 4.2.1) The choice of experimental approach

The aim of this work is to study the thermal behaviour of the two polytypes. The response of microporous materials on heating is not only of academic significance but also of potential industrial importance. Their thermal behaviour (i.e. stability, phase transformations, dehydration and rehydration temperature and rate and structural modifications) affects the absorption and diffusion of cations and molecules and, consequently, the catalytic properties of materials.

A variety of experimental approaches have been used to study the response of microporous materials on heating, among these diffraction techniques are particularly informative. For many years these studies were performed “ex-situ”, i.e. by collecting intensity data after the sample was

dehydrated – usually in a vacuum – at selected temperatures in a furnace and subsequently sealed in a glass capillary, therefore in a status not far from equilibrium conditions.

In the recent years, intensity data have frequently been collected by using so called “in situ” experimental approaches. In this case data collection is carried out by maintaining the temperature of the material.

Two “in situ” approaches are now being performed owing to the development of new X-ray diffraction techniques on powders or single crystal. In one approach, the sample is heated at a predefined temperature, and held at this temperature for many hours, prior to data collection, to ensure that the sample has reached a status as close as possible to its thermodynamic equilibrium at the chosen temperature; this technique is usually carried out on single crystals. In the second approach, the intensity data are collected in continuum over the course of heating in order to observe the transformation process “in real time” i.e. in conditions far from their equilibrium conditions. This technique is usually carried out on powders.

Many experiments have shown that a large number of materials display different behaviour if the heating process is performed far or near equilibrium conditions. For example, stilbite (Cruciani et al., 1997) and stellerite (Arletti et al., 2006), zeolites with the same topology, when heated transform into a new contracted phase. In this phase, an oxygen bridge in the tetrahedra 4-ring is broken and tetrahedral cations migrate to a new position. Surprisingly, structural data has shown that the breakage occurs on different T-O-T bridges if the minerals are heated by an “in-situ” approach on powders or by an “ex-situ” approach on single crystals. Investigations into the thermal behaviour of brewsterite both on “ex-situ” X-ray single crystals and on “in-situ” (in real time) X-ray powder analysis showed that with the first experimental approach a breakage of one T-O-T bridge occurred upon heating, whereas according to the second approach no indications of any T-O-T bridge breakage existed (Alberti et al., 1999; Ståhl and Hanson, 1999).

Remarkable differences in thermal behaviour, even if not as important, have been found in many other cases.

Recently, thermally-induced modifications in the monoclinic polytype of zeolite tschernichite have been studied by in situ X-ray single-crystal analysis in the temperature range 30-350°C (Alberti et al., 2007).

The results indicate that during the heating process, the framework behaves as a very rigid structure, whereas a loss of crystallinity occurs below 350°C indicating the low thermal stability of this polytype in natural Ca-rich tschernichite. It was not possible to perform an analogue study on the tetragonal polytype A because of the excessively small dimensions of the crystals in this polytype.

The aim of this work is to study and compare the thermal behaviour of both tschernichite polytypes. In this research we have utilised an experimental approach which is different from the one described earlier. In fact, X-ray diffraction data were collected by “time resolved” in-situ techniques on powders obtained from both large crystals, where polytype B is dominant, and small crystals where polytype A prevails. Moreover, time resolved analysis allowed a comparison of

the differences, if any, in structure modifications resulting from the experimental approaches. These results are of particular interest as tschernichite is a natural analogue of an important acid catalyst like beta, in which the physical separation of the two polytypes is not possible.

#### 4.2.2) Experimental method

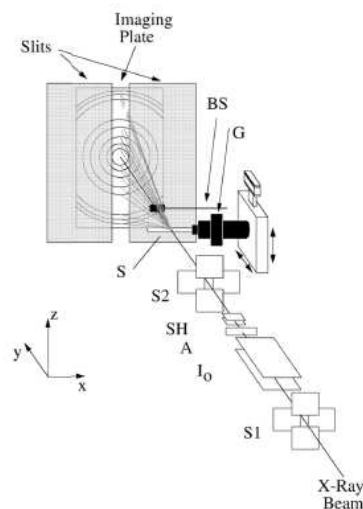
The “in-situ” time resolved diffraction measurements were performed at the GILDA-BM8 beamline at the ESRF, Grenoble, on a sample of tschernichite from Mont Adamson, Antarctica. For this experiment, two different data sets were collected, one set using small crystals (sample 2) and the other using large crystals (sample 1).

The powder samples were loaded and packed in a 0.3 mm diameter Lindemann capillary open at both ends then horizontally mounted on a rotating goniometer head. The capillary was heated *in situ* using a hot air stream equipped with a Eurotherm controller; a constant heating rate of 5°C/min was applied, and the samples were heated from 25°C to 800°C. The temperature was monitored using a thermocouple inserted at the heating gun opening. The measurements were carried out using the translating image plate (TIP) experimental setup technique (Figure 25), i.e. during the treatment powder diffraction patterns were continuously recorded during the heating treatment on a 4 mm slit-delimited portion of a 2D image plate which had a translating rate of 2.5 pixel/c with respect to the temperature increase (Norby 1997).

Monochromatic incident radiation characterised by  $\lambda = 0.68881(1) \text{ \AA}$  was selected. The distance between the sample and image plate was 204.7 mm and was determined by measuring the calibration procedure implemented in the FIT2D program. The temperature resolved diffraction patterns were extracted from the 2D image by integrating them onto 5°C-wide strips with an integration step of 10°C. External standard LaB<sub>6</sub> was used to calibrate the wavelength, as well as to determine the zero-shift position, sample to detector distance, and tilting angle of the image plate detector.

Figure 25: experimental setup

- The resolution slit system (vertical and horizontal) (S1)
- The ionisation chamber I<sub>0</sub>
- The absorber (A)
- The rotating shutter (SH)
- anti-scattering slit system (S2)
- sample (S)
- beam stopper (BS)
- rotating/oscillating goniometer heads (G)



### 4.2.3) Structure refinements

Structural refinements by full profile Rietveld on sample one (small crystals) and sample two (large crystals) were performed in the  $C2/c$  and  $P4_122$  space groups, respectively, using the GSAS package, starting from the atomic positions reported by Alberti et al. (2002). The evolution of the structural features was observed through 25 structure refinements. In all refinements the Bragg peak profile was modelled using a pseudo-Voigt function with a 0.005% peak intensity cut-off. The background curve was fitted using a Chebyshev polynomial with 24 terms. The  $2\theta$ -zero shift was accurately refined in all the data set patterns. One scale factor and the unit cell parameters were allowed to vary for all histograms. In the final cycles, the refined structural parameters for each data histogram were the following: fractional coordinates for all atoms, isotropic displacement and occupancy factor for extraframework sites and isotropic displacement factors (one for all tetrahedral cations, for all extraframework oxygen sites, for all extraframework cations and for all water molecules). Occupancy factor and isotropic displacement factor coefficients were varied in alternate cycles. Soft constrains were imposed on the T-O distances, and the same weight was used throughout the refinement procedure.

## 4.3) STRUCTURAL REFINEMENT RESULTS

It was possible to perform the structure refinements on polytype B (monoclinic) up to 400°C. The results indicate an acceptable agreement with those from “in-situ” single crystal structure refinements (Alberti et al., 2007) whereas, the structure refinements on tetragonal polytype had already become inconsistent at temperatures as low as 75°C. This result will be discussed later.

### 4.3.1) The two phase fractions in the large and small crystals, respectively.

The powder patterns of small and large tschernichite crystals are reported in Figures 26a and 26b.

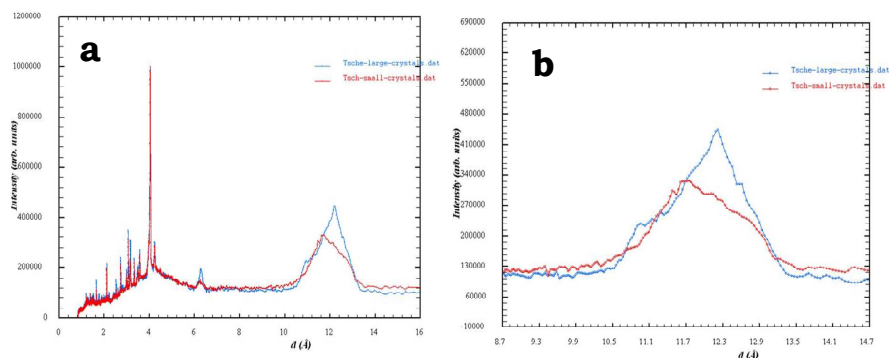


Figure 26: a) powder patterns of small and large tschernichite crystals; b) the two patterns in the low angle region

At a first examination, the two patterns seem very similar, leading to a doubt that they really do represent two different materials. However, a careful check of the 13-10 Å region (see Fig. 26b) clearly indicates that there are remarkable differences in the experimental profiles of the two samples. It is easy to attribute these differences to different fractions of polytypes in the two samples. It is therefore very important to determine this fraction.

Table 5 evidences the effect of the structural differences in the two polytypes in the low-angle region: two reflections occur in this region for both phases, (100) and (101) for the tetragonal polytype, (110) and (11-1) for the monoclinic type. (100) and (110) planes are orthogonal to the channel system, whereas (101) and (11-1) are parallel to the channel system.

Polytype A (tetragonal) $a=b=12.63\text{Å}$ , $c=26.51\text{Å}$	$2\theta$	d
(100)	$3.13^\circ$	12.63
(101)	3.46	11.40

$$I_{(100)} / I_{(101)} \approx 0.25$$

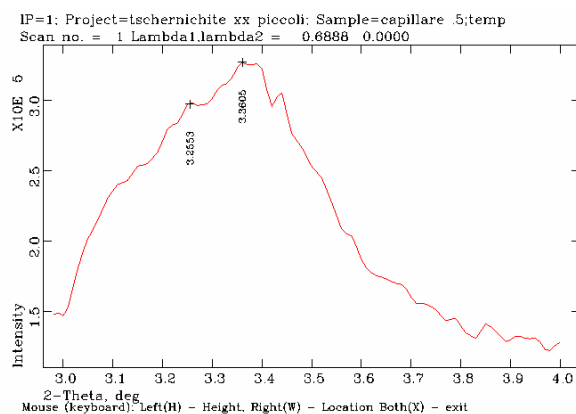
Polytype B (monoclinic) $a=17.98\text{Å}$ , $b=17.87\text{Å}$ , $c=14.61\text{Å}$ , $\beta=114.5^\circ$	$2\theta$	d
(110)	$3.27^\circ$	12.07
(11-1)	3.68	10.71

$$I_{(110)} / I_{(11-1)} \approx 2.0$$

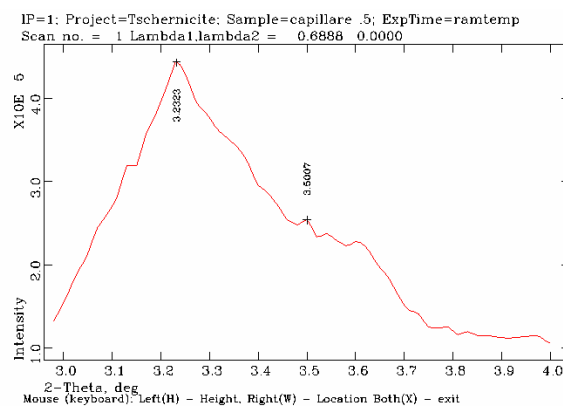
Table 5: reflections in the low-angle region for the two polytypes

If the results of the single-crystal structure refinement of monoclinic and tetragonal tschernichite (Alberti et al., 2002) are used, we found (Table 5, Figure 27) :

- the tetragonal polytype distances  $d_{(100)}$  and  $d_{(101)}$  are remarkably larger than the corresponding monoclinic polytype distances  $d_{(110)}$  and  $d_{(11-1)}$ ;
- in the tetragonal phase, the intensity of the peak (100) is by far lower than that of peak (101) ( $I_{(100)} / I_{(101)} \approx 0.25$ ), whereas in the monoclinic phase the intensity of peak (110) is by far higher than that of peak (11-1) ( $I_{(110)} / I_{(11-1)} \approx 2.0$ );
- if the intensity of the peaks is calculated considering only the framework atoms, the intensity ratios are strongly modified with ( $I_{(100)} / I_{(101)} \approx 3.2$ ) and ( $I_{(110)} / I_{(11-1)} \approx 1.5$ ).



Small crystals – 30°C



Large crystals – 30°C

Figure 27: results of structure refinement in the low angle zone for monoclinic and tetragonal polytypes.

Two different routes can be followed to determine the fraction of the two polytypes in the two samples: I) the domains of the two polytypes are sufficiently large to accept two phase Rietveld refinement as a sufficient approximation; II) the frequency of stackings faults in our samples is so high that only an approach through DIFFAX software (Newsan et al., 1988) can give an acceptable approximation.

With this second route, however, we met an almost insuperable obstacle: single-crystal structure refinements indicated that many cation and water molecules sites are present in both tschernichite polytypes and that all have partial occupancy. Moreover, the findings reported at point c) above, indicate that the effect of extraframework content on the intensities of the low-angle reflections cannot be neglected.

As a consequence, route I) was followed, considering the results as an acceptable semi-quantitative approximation.

If the peak positions and the slope of experimental profiles in the 13-10 Å region are compared with the calculated profiles, using the GSAS package, we observe that the experimental and calculated powder pattern fits quite well (Figure 28).

The results, reported in Table 6 indicate that sample two (large crystals) is characterised by a large prevalence of monoclinic polytypes, whereas in sample one, the tetragonal polytype is only slightly more abundant than the monoclinic polytype. It is practically impossible to state whether this last result is also due to the presence of some crystals which are predominantly monoclinic or if the monoclinic polytype is really preferred to the tetragonal one. It is of interest to note that, according to results by Newsan et al. (1988), the monoclinic phase represents about 56% of synthetic beta.

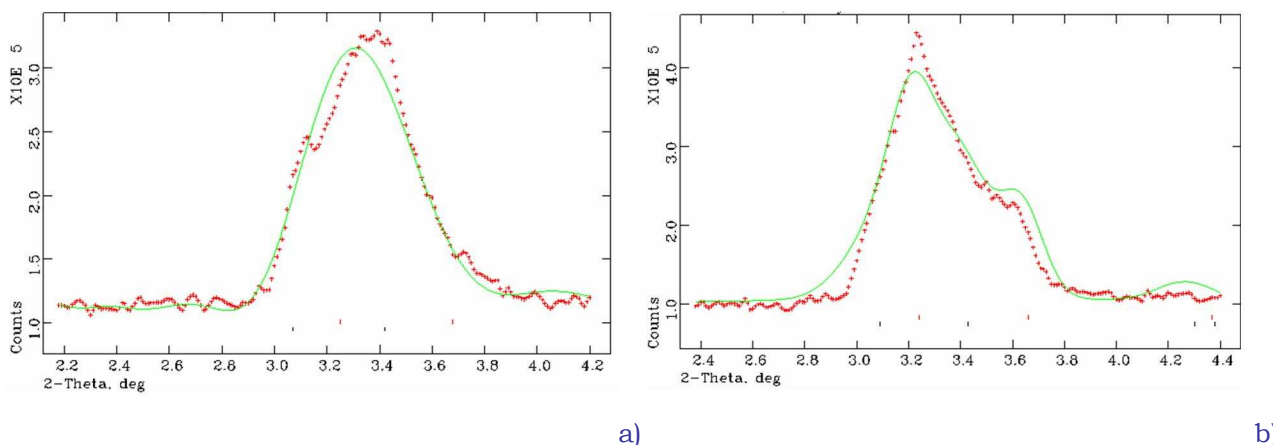


Figure 28: calculated and experimental profile in the low angle zone

Results of our refinements indicate that small crystals are composed of 65% tetragonal polytypes and 35% monoclinic polytypes, while large crystals are composed of 80% monoclinic polytypes and 20% tetragonal polytypes. This result could explain the difficulties encountered during the structure refinement of sample with small crystals.

	Large crystals	Small crystals
30°C	A: 83% B:15%	A: 33% B:67%
40°C	A: 80% B:17%	A: 38% B:62%
50°C	A: 78% B:22%	A: 30% B:70%
Average	A: 80% B:20%	A: 34% B:66%

Table 6: fraction of tetragonal polytypes (A) and monoclinic polytypes (B) in large and small crystals, respectively, at 30, 40 and 50°C obtained using the GSAS package

#### 4.3.2) Thermal stability

The stepwise dehydration process in tschernichite, monitored by the break-up of powder patterns as a function of temperature, put in evidence some important differences in the behaviour of the two polytypes.

The temperature resolved diffraction data show that the amorphisation process begins at about 250°C in tetragonal polytype and at about 450°C in the monoclinic type (Figure 29). Figure 30 reports refined unit cell parameters as a function of temperature for both tetragonal (a) and monoclinic samples (b).

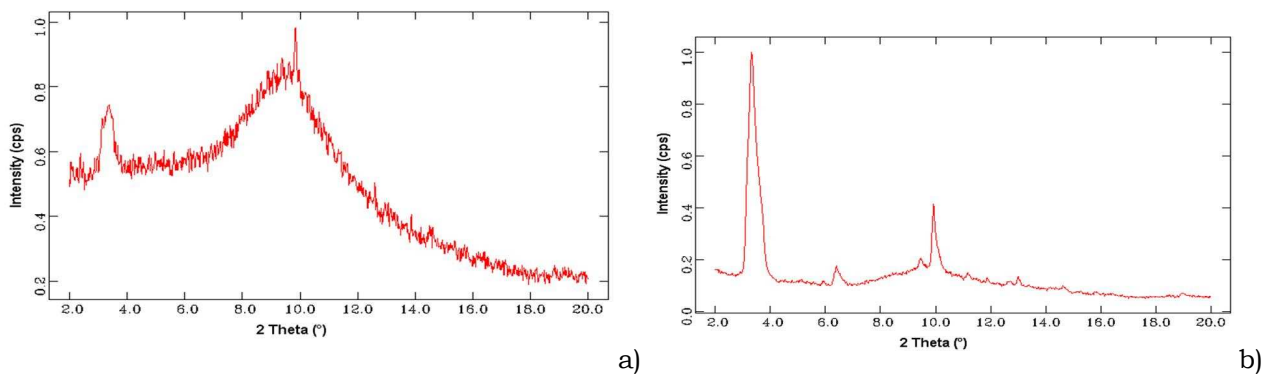


Figure 29a and 29b: diffraction data at amorphisation temperature for tetragonal (left) and monoclinic (right) polytype

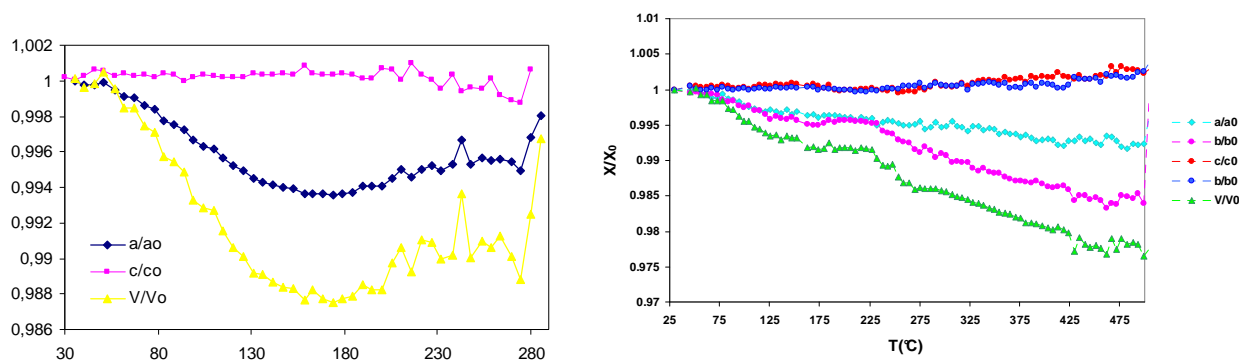


Figure 30: temperature dependent variations in the unit cell parameters in tetragonal (left) and monoclinic (right) polytype

This is an important point which deserves some consideration. Usually the thermal stability of a zeolite increases with an increase in the Si/Al ratio. This value is around 4.0 in small crystals where the tetragonal polytype prevails and around 2.6 in large crystals where the monoclinic polytype is dominant. Therefore, these data are in disagreement with in situ temperature resolved studies.

We can hypothesise two different mechanisms to justify this result:

1- the presence of a very high fraction of monoclinic polytypes in sample A (comparable with that of the tetragonal type) generates frequent staking vectors where polytypes A and B meet.

According to Wright et al. (2005) linear defects can be favoured in the staking directions, thus favouring an instability in the framework at lower temperatures. On the contrary, in sample B, where only one polytype (the monoclinic one) is preponderant, staking vectors and linear defects are less frequent, favouring a stability at higher temperatures. Since the remarkable presence of polytype B (monoclinic) in the sample is characterised by small crystals (polytype A), Rietveld refinements in sample 2 (small crystals) led to physically inconsistent results. On the other hand, structure refinements of sample 1 (monoclinic) provided a physical picture of the dehydration process which is consistent with the results reported by Alberti et al (2007).

2- the monoclinic polytype is energetically more stable than the tetragonal polytype

Weak support for this hypothesis could be found in high-resolution transmission electron microscopy (HR-TEM) studies by Szostak et al. (1995) and Wright et al. (2005) which seem to indicate that monoclinic domains are often larger than tetragonal ones or in the paper by Newsan et al (1988) where the computed profile of the first low angle peak of zeolite beta suggests a B/A ratio of about 1.35. These indications, however, are in disagreement with the computational study by Tomlinson et al. (1990) who found that the lattice energy of polymorphs A and B are about the same.

## 5.1) GMELINITE: STRUCTURAL AND CHEMICAL FEATURES

Gmelinite is a natural sodium zeolite which typically occurs in hydrothermal formations, mainly filling cavities in basalts. It is often closely related to chabasite, and the structural intergrowth of these two minerals are quite common (Passaglia et al., 1978).

The crystal chemistry of gmelinites was studied by Passaglia et al. (1978). The Si/(Si+Al) ratio varies in the range 0.65 - 0.71. Usually Na is the prevalent extraframework cation, but samples are not infrequent where Ca is the most abundant cation; in some cases (Malinovskii, 1984; Vezzalini et al., 1990; Luppi et al., 2007) potassium is the most abundant extraframework cation. Consequently, according to the Recommended Nomenclature of the IMA Subcommittee on Zeolites, three separate species must be recognised, gmelinite-Na, -Ca, and -K (Coombs et al., 1997).

The structure of gmelinite was first resolved by Fisher (1966) on a sample from Nova Scotia. Structure refinements on gmelinite-Na and gmelinite-Ca were performed by Galli et al. (1982), on gmelinite-K by Malinovskii (1984) and Vezzalini et al. (1990) whereas structure refinement on Ba-substituted gmelinite was carried out by Vigdorichik and Malinovskii (1986). In all these samples, two extraframework cation sites were localised near the walls of the channels, whereas the number of water sites varies according to the most abundant extraframework cation.

Zeolite gmelinite shows a hexagonal crystal structure, with space group  $P6_3/mmc$  (Fisher, 1966; Galli et al., 1982). The aluminosilicate framework was assigned the IUPAC code GME (Meier and Olson, 1992). It consists of a parallel stacking of double six rings (D6R units) in the sequence AABB. The resulting structure is characterised by a one-dimensional channel parallel to [001] delimited by rings of twelve tetrahedra (size  $7 \text{ \AA} \times 7 \text{ \AA}$ ) interconnected via two-dimensional 8-ring channels (size  $3.6 \text{ \AA} \times 3.9 \text{ \AA}$ ) orthogonal to the 12-ring channel, thus forming a multi-dimensional channel system (Figures 31).

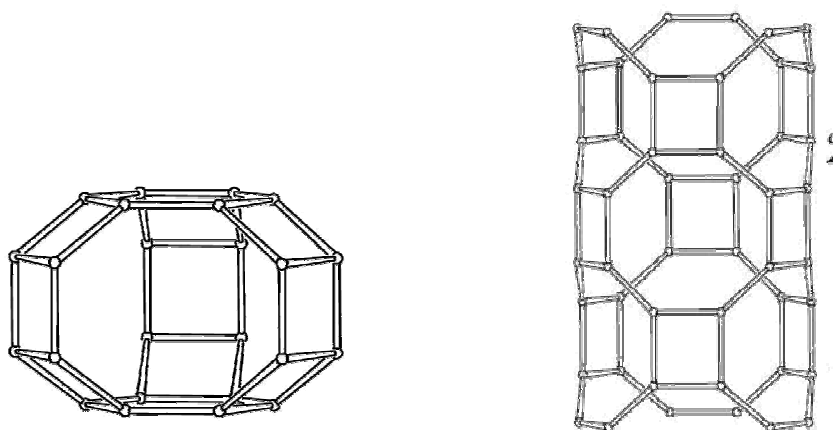


Figure 31: structure of zeolite gmelinite (on the left: gmelinite cage, on the right: the 12-ring channel)

Channels are occupied by extraframework mono- and divalent cations and  $\text{H}_2\text{O}$  molecules.

Previous works on Ca-, Na- and K rich- natural gmelinite (Malinovskii, 1984; Vezzalini et al., 1990; Fisher, 1966) revealed that two extraframework cation sites are present: C1 site, located in the

gmelinite cage, six-fold coordinated, and the C2 site, located in the 12-ring, fivefold coordinated in Ca and Na gmelinites, and sevenfold coordinated in K-gmelinites. It was also observed that as a consequence of the variety of exchangeable cations, frameworks may undergo a *c* lengthening and an *a* shortening, caused by the radius of extraframework cations and the strength of the bonds between the C2 cations and the framework oxygens.

The thermodynamic properties of natural gmelinite-Na from 5.8 to 302K were investigated by Paukov et al. (2001). The authors found that the molar heat capacity function ( $C_{p,m}$ ) of gmelinite displays anomalous behaviour at  $T > 160$  K. Above this temperature an additional contribution to the heat capacity appears. The authors suggested that this effect was a result of the disordering in the water and cations subsystem of gmelinite.

The thermal behaviour of natural gmelinite-Na from Prospect Park, New Jersey, and some of its ion-exchanged forms ( $\text{NH}_4^-$ , Ca-, and K-), was investigated by Kühn and Miale in 1978 in a study for Mobil. They found that gmelinite-Ca transforms into a new, unidentified, phase when heated for three hours at  $350^\circ\text{C}$ , and that the new phase is stable up to  $760^\circ\text{C}$ , when gmelinite has already collapsed. On the contrary the  $\text{NH}_4^-$  and K-forms of gmelinite do not show phase-transformation up to at least 825 K.

Huo and Stephenson (2002) showed that a Na-gmelinite synthesised having a quaternary ammonium template and a Si/Al ratio of around 4, when calcined in air for 5 hours at 775 K transforms into a new phase with AFI topology. The same result is obtained when the exchangeable cation is Li, Ca, Ba and Mg. On the contrary, K-gmelinite can be calcined up to 975 K to form a pure K-gmelinite zeolite by removing the ammonium template.

The interest in gmelinite was due to the straight 12-ring channel, which could make gmelinite a good catalyst for hydrocarbons conversion. Natural and synthetic gmelinite has often shown intergrowth with chabazite or related zeolites which block the 12-ring channel of the gmelinite structure, reducing the expected sorption properties to those of an 8-ring or smaller window zeolite. According to Daniels et al. (1978) polymeric cations prevents stacking faults in synthetic gmelinite. The only known gmelinite materials having open 12-ring channels are made with a DABCO polymer filling the channels (L.D. Rollman, 1984).

Furthermore, there is a study by EXXON Research Engineering (Vaughan and Strohmaier, 2002) on transition metal substituted gmelinite. The authors studied the directed crystallisation of a synthetic transition metal aluminosilicate crystalline zeolite with the gmelinite structure and chemical composition in the unhydrated form, since the product of this process can be used as a catalyst in a hydrocarbon conversion process or a Fischer-Tropsch synthesis.

Another study (Carpency et al., 1997) deals with a process for improving the conversion of a hydrocarbon feedstock to light olefins which is comprised of containing a hydrocarbon feedstock containing at least one diolefin involving various zeolites among which are those zeolites which belong to gmelinite group.

Cao et al, (1998) suggested a way for improving the catalytic activity and hydrothermal stability of small and medium pore acidic zeolite catalysts, among which gmelinite, by treating these zeolites with a phosphorus compound to form a phosphorus-treated zeolite and combining the phosphorus-treated zeolite with  $\text{AlPO}_4$ . According to the authors, this invention may be used in a

process for cracking hydrocarbons, or it can provide a method for improving the stability of a catalyst over time compared to an untreated zeolite catalyst of the same type.

## **5.2) EXPERIMENTAL**

### **5.2.1) Material**

A sample of gmelinite from Flinders, Victoria, Australia, was used in this study. The chemical composition ( $\text{K}_{0.27}\text{Na}_{6.98}\text{Sr}_{0.01}\text{Ca}_{0.15}\text{Mg}_{0.01}\text{Fe}_{0.01}(\text{H}_2\text{O})_{70} [\text{Al}_{7.40}\text{Si}_{16.55}\text{O}_{48}]$ ) was obtained on crystals of the sample by an ARL-SEMQ microprobe in wavelength dispersive mode operating at 15 Kv, 10 mA, and using a beam size of 45  $\mu\text{m}$ . A defocused beam and low beam count were chosen to minimise the Na loss. Twelve point analyses were performed; their low variability indicated good compositional homogeneity on the sample crystals. The estimated  $\text{H}_2\text{O}$  value was taken from the value (19.70% in weight) given by Passaglia et al. (1978, analysis n. 20) for gmelinite from Flinders, Victoria, Australia. It is worth noting that in gmelinites the water content is always in the narrow range 19.3-20.6% in weight, which corresponds to 21.5-23.0 of water molecules per unit cell, with a mean value of around 22.0-22.5. Note the very low calcium and potassium content, indicating that this sample must be classified as a gmelinite-Na according to the classification of the IMA Commission (Coombs et al., 1997).

### **5.2.2) In-situ single crystal analysis**

As a first step, single crystal analysis at room temperature was performed using a latest generation Nonius four cycle diffractometer equipped with a CCD detector and MoK $\alpha$  radiation.

Structural refinement was performed on the data obtained (GME-RT). The Si/Al ratio given by the chemical analysis was used for the atomic scattering curve of the tetrahedral cation, whereas the atomic scattering curve for Na was used for extraframework cations.

The data from Paukov et al. (2001) showed anomalous behaviour in the molar heat capacity at  $T > 160$  K and suggested the collection of diffraction data at a lower temperature in order to clarify if any structural modification had occurred. Therefore, a crystal was quenched to 100 K directly on the single-crystal diffractometer by a temperature-controlled nitrogen stream and a data collection was performed (GME-100K). Immediately after the data collection, the crystal was reported at room conditions and a new data collection was carried out.

Single crystals from the same sample from Flinders, were selected and glued to a quartz capillaries with a very small amount of refractory cement, (M-BOND GA-100, which is mainly composed of aluminium) in order to observe the dehydration-rehydration processes in gmelinite-Na. These capillaries were in turn inserted into an ENRAF NONIUS FR 559 goniometer head, built up according to the design proposed by Tuinstra and Fraase Storm (1978). The heater uses the principle of double gas streams flowing parallel to the goniometer head axis, which provide a cylindrical cool-gas stream that encloses the hot-gas jet coaxially. The crystal was heated by a hot

nitrogen flow, and the temperature was measured with a thermocouple placed about 4 mm below the capillary.

To ensure that the sample had reached the status which is as close as possible to its thermodynamic equilibrium and in order to prevent crystallinity loss, the heating profile was: ramp from room temperature to the heating temperatures with 2°C/min heating rate, held at these temperatures for about 14h prior to data collection, and then this process was repeated up to the collapsing temperature. A similar approach was followed for the cooling process from 90°C to 75°C and from 75°C to RT, using a 2°C/min cooling rate. Two different data collections were performed after cooling at room temperature; the first immediately after cooling, the second three days after cooling.

A first crystal, after data collection at room temperature, was heated at 50°C (GME-50), and subsequently at 100°C to perform data collections. Surprisingly, the crystal when heated at 100°C resulted as destroyed into minute fragments, so that a data collection was not possible. A second crystal, after data collection at room temperature, was heated at 75°C (GME-75) and then heated at 100°C. As for the first crystal, the heating at 100°C caused the fragmentation of the crystal, thus confirming the presence of strong strains in the framework, or even a possible collapsing of the framework of gmelinite at a temperature as low as 100°C. A third crystal, after data collection at room temperature, was heated at 90°C (GME-90) then cooled to 75°C (GME-75r) and to room temperature according the modalities described before (GME-RTr, and GME-RTr-3d).

As seen above, the fragmentation of the crystals before 100°C could be due to the presence of strong strains in the framework, to a collapse in the structure, or to a phase transformation of the mineral. In order to understand the causes of this unusual behaviour it was decided to perform other data collections, by ex-situ single crystal analysis and X-ray powder diffraction.

### **5.2.3) Ex-situ X-ray powder data collection**

Powders from the same sample were heated at increasing temperatures with the modalities used for single crystals, i.e. at the desired temperatures with 2°C/min heating rate and held at the temperature for 14 h before data collection. As a first step, the powders were heated at 130°C and an X-ray powder pattern was collected using a Bruker Advance diffractometer with a Sol-X solid state detector and a CuK $\alpha$  radiation. It was evident from the pattern that gmelinite is still present and maintained good crystallinity. Therefore the same powders were heated at increasing temperatures by steps of 50°C and for each temperature powder patterns were collected according to the modalities described before. No remarkable differences in the patterns were observed up to 280°C. At 330°C the powder pattern evidenced a phase transition of gmelinite-Na to a new

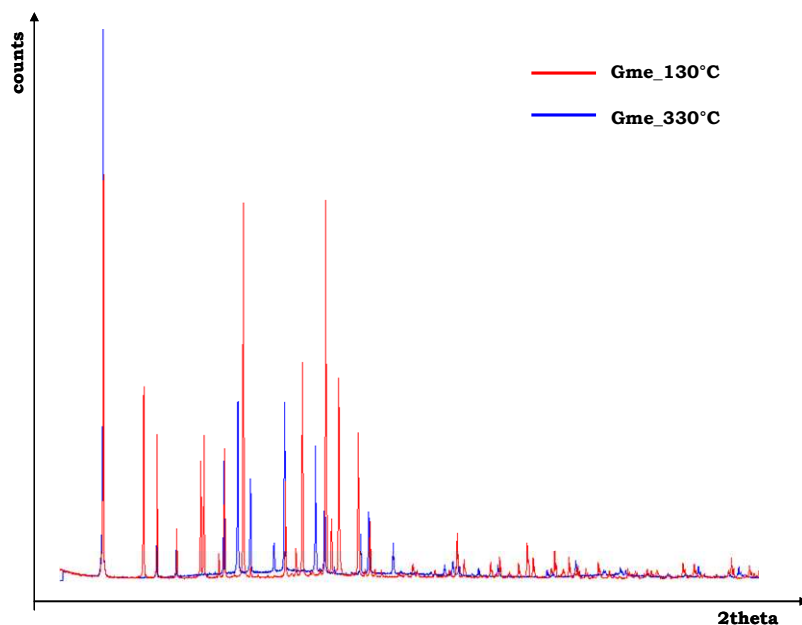


Figure 32: a comparison between Gme\_130°C and Gme\_330°C patterns

structure (Figure 32), whose pattern resembles that of a structure with AFI-type topology (Figure 33), even if strong differences in the intensities of the diffraction peaks appear.

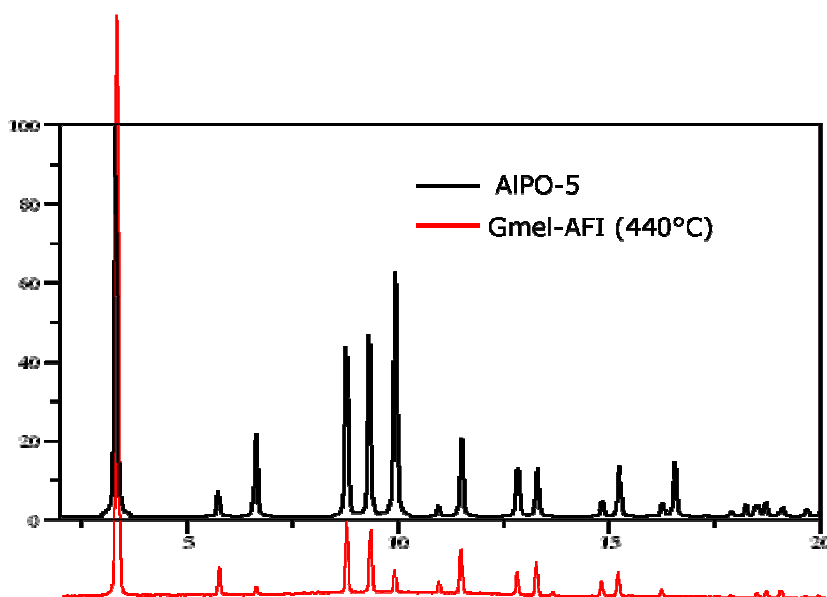


Figure 33: comparison between AIPO-5 and Gmelinite heated at 440°C patterns

This result agrees with the findings of Huo and Stephenson (2002) who observed that a gmelinite in its Na-form, which is synthesised with a quaternary ammonium template and calcined at 500°C transforms into a new phase whose powder pattern resembles that of an AIPO-5 material. In order to determine the range of stability of this new phase the same powders were heated at increasing temperatures, following the modalities described before, up to the collapse of the framework. The powder patterns showed that the material is thermally stable to 830°C without any remarkable loss of crystallinity, whereas at 880°C, and at 930°C, the material is completely amorphous. It is worth noting that the behaviour of this material at high temperatures differs

from that of AlPO-5. In fact, according to Bennett et al. (1983), the AlPO-5 sieve is thermally stable to 1000°C above which it transforms to the AlPO<sub>4</sub> analogue of tridymite.

Rietveld structure refinement from the powder pattern collected at 330°C confirmed the AFI-type topology; however, AlPO-5 and this material are characterised by fundamental differences in the structure.

#### **5.2.4) Ex-situ single crystal data collection**

In order to better understand the differences between this new phase and AlPO-5 structure, many single-crystals of gmelinite from the same sample were heated at 330°C. The largest number of these crystals was completely fragmented, but a few crystals remained sufficiently undamaged to allow a single-crystal data collection.

The single-crystal X-ray data collection was performed on the same diffractometer as described earlier. Synthetic precession images of the hk0, h0l, and hk1 reciprocal planes were obtained using the Nonius Collect Package.

#### **5.2.5) In-situ time-resolved synchrotron data collection**

The “in-situ” time resolved diffraction measurements on a powder sample of gmelinite-Na were performed at the GILDA-BM8 beamline at the ESRF, Grenoble. The powder samples were loaded and packed in a 0.3 mm diameter Lindemann capillary open at both ends then horizontally mounted on a rotating goniometer head. The capillary was heated in situ using a hot air stream equipped with a Eurotherm controller; a constant heating rate at 25°C/min was applied, and the samples were heated from 25°C to 940°C. The temperature was monitored using a thermocouple inserted at the heating gun opening. The measurements were carried out using the technique of translating image plate (TIP) experimental setup, i.e. during the treatment powder diffraction patterns were continuously recorded during the heating treatment on the 4 mm slit-delimited portion of a 2D image plate which had a translating rate of 2.5 pixel/c with respect to the temperature increase (Norby 1997).

A monochromatic incident radiation characterised by  $\lambda = 0.68881 \text{ \AA}$  was selected. The distance between the sample and image plate was 204.7 mm and was determined by measuring the calibration procedure implemented in the FIT2D program. 37 whole one-dimensional powder patterns were extracted from the image plate by integrating the 5°C-wide strips and with an integration step of 10°C. An external standard LaB<sub>6</sub> was used to calibrate the wavelength, as well as to determine the zero-shift position, sample to detector distance, and tilting angle of the image plate detector.

### **5.3) STRUCTURE REFINEMENTS**

#### **5.3.1) In-situ single crystal analysis**

Crystal structure refinement parameters are reported in Tables 7a and 7b. The DENZO-SMN (Otwinosky and Minor 1997) package was used for the refinement of the unit cell parameters and data reduction. The SHELXL-93 (Sheldrick, 1993) program was employed for all the crystal structure refinements. Systematic extinctions were always consistent with the topological hexagonal  $P6_3/mmc$  space group, and the starting parameters used for refinement were taken from Passaglia et al. (1982). No other significant extraframework sites were found from the electron densities localised in the Fourier maps. Crystallographic R1 (Fo based) factors for these structures, over the studied temperature range, varied between 3.8 – 7.6 % (see Table 7a and 7b). Tables 8a, 8b, 8c and 8d reports the atomic coordinates, occupancy and equivalent temperature factor, Table 9 the T-O distances, O-T-O and T-O-T angles, and the coordination distances of the extraframework cations and water molecules

#### **5.3.2) Ex-situ single crystal refinements**

Crystal structure refinement parameters are reported in Tables 10. The DENZO-SMN (Otwinosky and Minor 1997) package was used for the refinement of the unit cell parameters and data reduction. The SHELXL-93 (Sheldrick, 1993) program was employed for all the crystal structure refinements. The topological hexagonal  $P6/mmc$  space group was used for the refinement. The starting parameters used for refinement were taken from Passaglia et al. (1982) (Tables 11).

### **5.4) RESULTS AND DISCUSSION**

#### **5.4.1) Crystal structure from in-situ single-crystal analysis at room temperature (GME-RT)**

Only one independent tetrahedral site is present in the gmelinite framework. Its Al content calculated from the structure refinement data according to the method of Alberti and Gottardi (1988) is 30.5% in very good agreement with that found by the chemical analysis (30.9%).

As for the sodium-rich gmelinite of Galli et al. (1982), two extraframework cation sites have been localised, one (C1 in Table 8b) is fully occupied, the other one (C2 in Table 8b) is partially occupied. Overall, 84.3 e<sup>-</sup> have been found in comparison with the 85.5 e<sup>-</sup> given by the chemical analysis. Water molecules are located over three extraframework sites (named W1, W2, W3 according to the notation of Galli et al., 1982). W1 sites resulted as occupied in very near to 50% of cases, but the short distance (1.84 Å) from a symmetrically equivalent position imposes that water molecules occupy the two positions alternately. W2 is fully occupied, whereas W3 is partially occupied, with very high occupancy (85%, Table 8b). Overall, 22.2 water molecules have been localised in excellent agreement with the 21.85 molecules given by the chemical analysis.

C1 site is coordinated to three W1 water molecules and three O2 framework oxygens, whereas three O1 oxygens are at a large distance (3.28 Å). Cations in C2 sites are coordinated to four water molecules and three framework oxygen atoms. The C1 distance from the two water molecules are quite short (C2-W3 = 2.11 Å; C2-W2 = 2.18 Å) when compared with an ideal Na-O<sub>w</sub> distance (around 2.35 – 2.40 Å), but the high displacement factors of the two O<sub>w</sub> atoms can be interpreted as a static disorder of water molecules over two possible positions, one when cation site is empty (we must remember that the C2 site is occupied in only 30% of the cases), the other cases are when both sites are occupied simultaneously (Figure 34).

As reported in the Experimental Section, a structure refinement at RT was carried out before heating all the crystals used in this work. The differences, both in coordinates, occupancies, atom-atom distances and displacement factors, are always very small, and the results do not modify those described in this section at all.

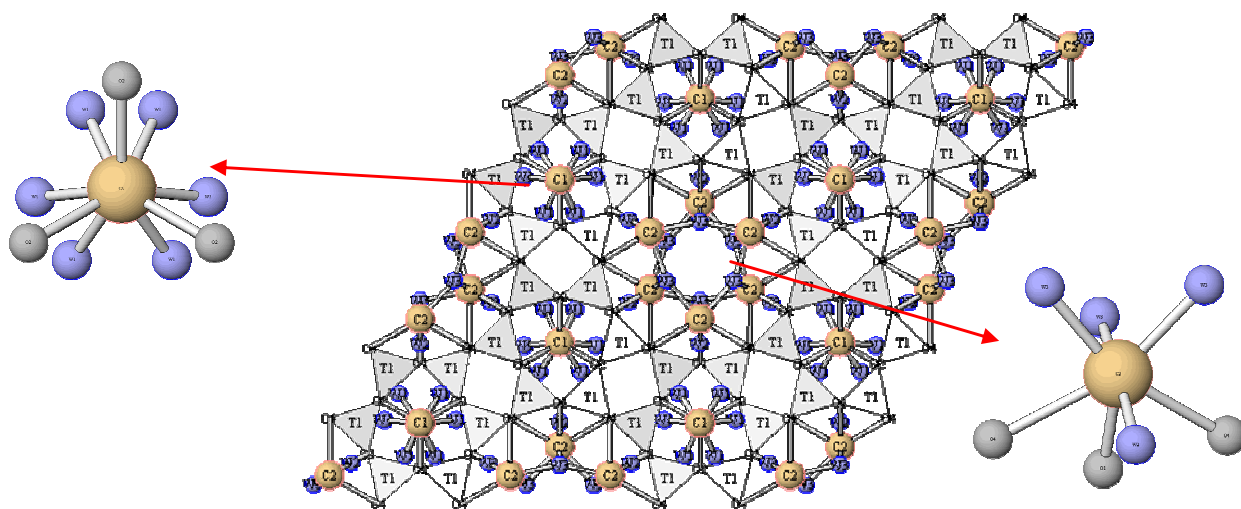


Figure 34: Crystal structure of gmelinite at T=25°C. On the left, C1 site, sixfold coordinated, and on the right C2 site, sevenfold coordinated

#### 5.4.2) Crystal structure from in-situ single-crystal analysis at 100K (GME 100K)

The starting parameters used for the crystal structure refinement of gmelinite at 100K were from GME-RT. Remarkable modifications in the extraframework content were immediately evident. Site W3, which at room temperature was almost completely occupied (see Table 8d) was found empty, whereas Na2, W1 and W2 sites resulted less occupied, with a decrease of their occupancy to around 15-20%. Only Na1 position, fully occupied in gmelinite at room temperature, maintained its full occupancy. Moreover, all these ions are remarkably shifted from their original positions. A new partially occupied site, attributed to H<sub>2</sub>O molecules on the basis of its coordination, (W4) was found using the Fourier maps. As a result, about 10% of cations and 20% of water molecules found using chemical analysis were not localised.

An inspection of the most probable symmetry indicated that the acentric space group  $P3_1c$  is slightly more probable than those of the oloedric  $P6_3/mmc$  and the emiedric  $P6_3/m$  and  $P-3_1c$  groups. Structure refinements were carried out in all these space groups and the most satisfactory result was obtained in the  $P3_1c$  space group. Difference and  $F_o$  syntheses showed the presence of weak maxima, five of these were refined and resulted weakly occupied (see Table 8d). According to their coordination four of these were attributed to water molecules, the other to cations. With these assumptions, about 95% and 85% of cations and water molecules found at room temperatures were localised. It is worth noting that the coordinates of some framework atoms (O3 and O4 in particular) differ from the  $P6_3/mmc$  symmetry by more than ten times their standard errors and the extraframework sites indicated remarkable shifts from the removed symmetry elements and the absence of the equivalent maxima in the Fourier maps. Therefore the most probable space group is  $P3_1c$  rather than  $P6_3/mmc$  (Figure 35).

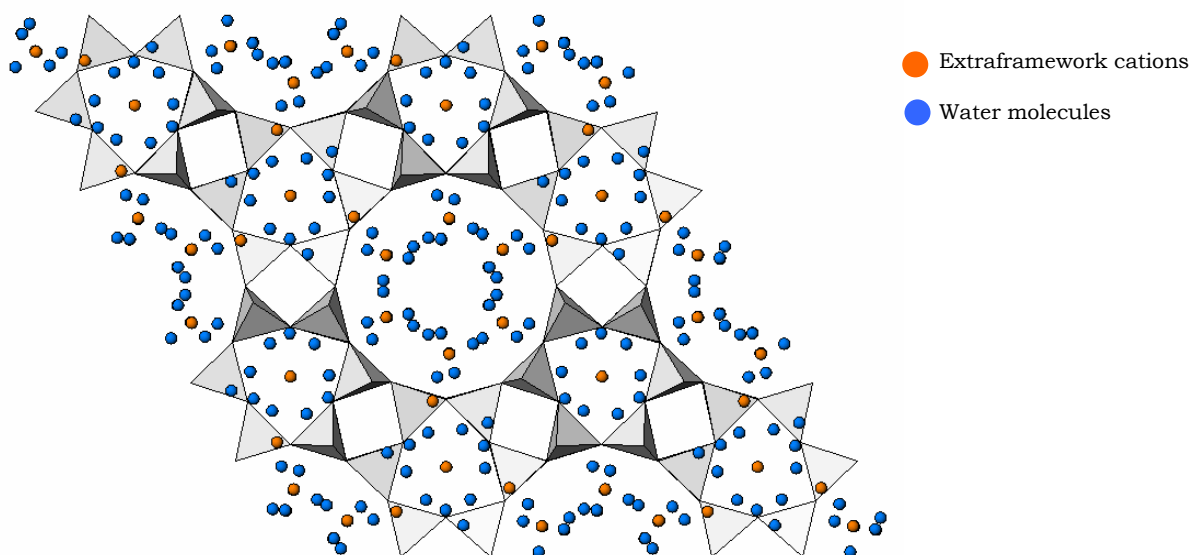


Figure 35: Gmelinite structure at T=100K

#### 5.4.3) Crystal structure from in-situ single-crystal analysis after cooling (GME-RTr)

After the data collection at 100K, the temperature was rapidly increased and a data collection on the gmelinite crystal was carried out. A crystal structure refinement was performed on these data and it indicated the complete reversibility of the process. All structure parameters, atomic coordinates, temperature factors and occupancies were almost identical to those obtained before the quenching of the crystal.

#### 5.4.4) Crystal structure from in-situ single-crystal analysis at T=50°C (GME-50)

The most relevant effect due to the heating at 50°C was the loss of a remarkable fraction of water (around 40% of the total) which is nearly equally distributed over the three H<sub>2</sub>O sites. As a consequence, cations in C1 site can be bonded only to two water molecules in W1 position and their coordination number decreases to five. Significant shifts in C2, W2, and W3 cause an increase in the C2-W3 distance and a remarkable decrease in the C2-W2 distance (from 2.18 to 1.93 Å). This distance is too short for a bond distance even considering the high displacement factors of C2 and W2, but the sum of occupancies of C2 and W2 is now less than 100%, so that the two sites are never occupied simultaneously, and the coordination number of C2 cannot be higher than six.

#### 5.4.5) Crystal structure from in-situ single-crystal analysis at T=75°C (GME-75)

At 75°C at least 90% of H<sub>2</sub>O was lost and only W1 site resulted weakly occupied (25%). As a result, no more than one water molecule can be bonded to C1. It is worth noting that as far as W1 site fraction decreases are concerned, framework oxygen O1 shifts towards C1. As a consequence of the water loss, the C2 site is now only bonded to one O1 and two O4 oxygens (see Table 9) assuming a three-fold coordination. It is important to note that the lowering of the coordination number of C1 is accompanied by a shortening of the distances C2-O1 and C2-O4 (Figure 36).

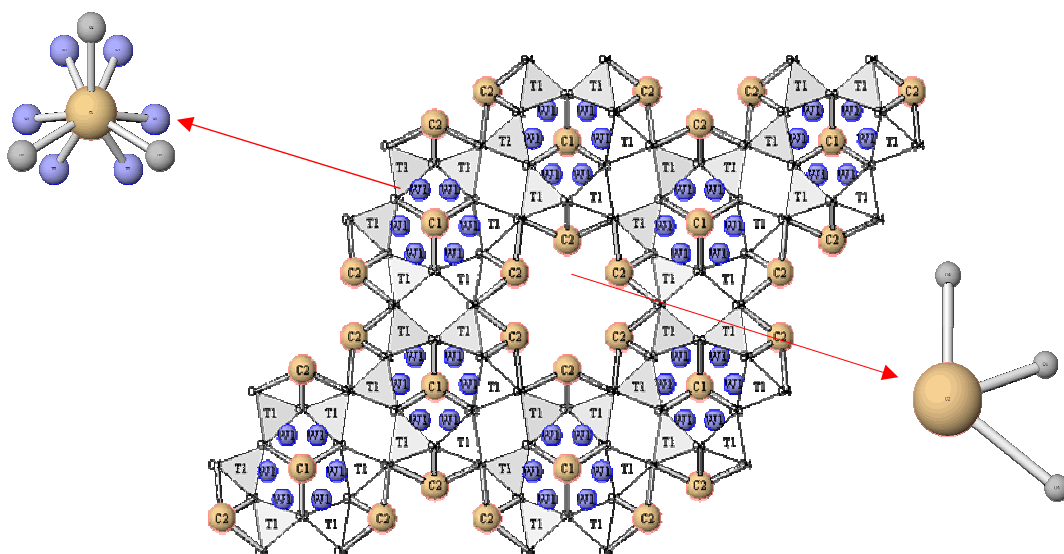


Figure 36: Crystal structure of gmelinite at T=75°C. On the left, C1 site, sixfold coordinated, and on the right C2 site, threefold coordinated

#### 5.4.6) Crystal structure from in-situ single-crystal analysis at T=90°C (GME-90)

At this temperature gmelinite is fully dehydrated; the O1 site continues its migration toward C1 up to a C1-O1 distance of 3.00 Å, which must be considered a coordination distance; this result evidences the interaction between the cations in C1 site and the framework oxygens O1. No significant modification affects the polyhedron C2, which remains three-coordinated. It should be noted that the four atoms C2, O1 and two O4 lie about on the same plane, forming a rhomboidal

configuration with angles O4-C2-O4 and O4-O1-O4 of 119° and 135°, respectively, and angles C2-O4-C1 of 52° (Figure 37).

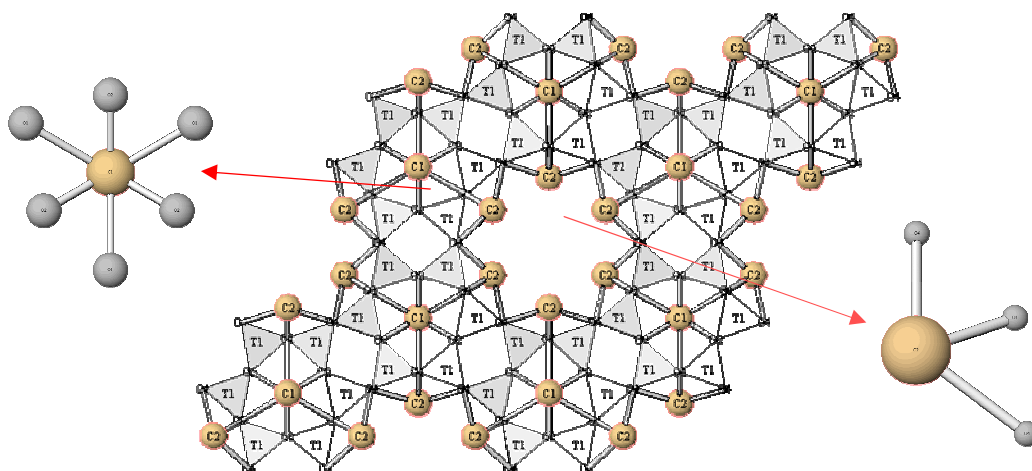


Figure 37: Crystal structure of gmelinite at  $T=90^{\circ}\text{C}$ . On the left, C1 site, fivefold coordinated, and on the right C2 site, threefold coordinated

#### 5.4.7) Crystal structure from in-situ single-crystal analysis at $T=75^{\circ}\text{C}$ (cooling) (GME-75r)

Gmelinite cooled to  $75^{\circ}\text{C}$  does not show any detectable rehydration and its structure is practically the same as GME-90 (see Table 8b).

#### 5.4.8) Crystal structure from in-situ single-crystal analysis at $T=25^{\circ}\text{C}$ (cooling) (GME-25r)

The structure refinement on gmelinite performed on data collected immediately after cooling at room temperature indicates that about 70% of the water content of untreated gmelinite was re-absorbed on W1, W2, and W3 sites with occupancies of 82, 76, and 63%, respectively. These values are slightly higher than those found for gmelinite heated at  $50^{\circ}\text{C}$  (see Table 8b). Worth noting is the quite short C2-W2 distance (2.04 Å), which is larger than the C2-W2 distance found in GME-50 (1.93 Å) where the occupancy of W2 was lower (65%). As in GME-50, however, this distance is shorter than the C2-W3 one (Table 9).

#### 5.4.9) Crystal structure from in-situ single-crystal analysis at $T=25^{\circ}\text{C}$ (after 3 days) (GME-25r-3d)

Three days after cooling gmelinite is completely rehydrated and the structure is identical to that of its untreated version. As for GME-RT, the C2-W3 distance is now shorter than the C2-W2 distance.

## 5.5) DISCUSSION OF IN-SITU SINGLE CRYSTAL DATA

During the dehydration-rehydration process, the variation of the unit cell parameters,  $a$ ,  $c$  and volume, were always less than 1.5%, and the distortions undergone by the framework were quite modest, so that gmelinite can be classified as belonging to the first classification group of Alberti and Vezzalini (1984), or as a non-collapsible framework according to Baur (1992).

As pointed out before, the results of the crystal structure refinements indicated that gmelinite-Na at 100 K strongly differs from gmelinite-Na at room conditions. What is particularly surprising is that cations and water molecules at a very low temperature extraframework spread over a large number of sites at low occupancy. With the increase in temperature these sites gather in few positions with higher occupancy (W1, W2, W3, C1, C2). To our knowledge, only dehydrated low silica X in its Li-form is characterised by an analogous behaviour. Paukov et al. (2001) found that the derivative of heat capacity of gmelinite-Na  $dC_{p,m}/dT(T)$  grows, starting from  $T > 160$  K. This implies that there is an additional contribution to the heat capacity which could be explained with the gradual disordering of water molecules over a large temperature interval (Hemingway and Robie, 1984).

In the case of gmelinite-Na from Flinders, however, the results seem to indicate an ordering of water molecules and extraframework cations with an increase in temperature. As reported in the “Experimental” section, a new X-ray data collection on the same crystal was performed at room conditions, either after the data collection at 100 K or after calcination, and gmelinite showed a complete restoring of its initial structure both when cooled to 100 K and when heated up to its complete dehydration.

Gottardi and Galli (1985) performed thermogravimetric analysis (with a heating rate of 20°C/min) on a sample of gmelinite from Flinders. They found that the dehydration process can be divided into three steps, at 100, 175 and 300°C, and that this process is complete at 400°C. These results seem to be in disagreement with our findings, but we have to consider that single-crystal X-ray data collections were performed many hours after heating, i.e. in conditions at, or very near to, equilibrium conditions, whereas the thermal analysis data refer to conditions far from equilibrium. Anyway, it is unusual for a zeolite to lose all its water content at a temperature as low as 90°C. As concerns the findings of the three different steps of dehydration, interpreted by Gottardi and Galli (1985) regarding the loss of water molecules at different temperatures in the three different crystallographic sites, this work seems to contradict this interpretation, as the water is lost at any temperature roughly proportionally for all the three sites. However, the structural modifications induced by heating, demonstrate that the features of thermal analysis cannot be explained by the loss of water molecules in the gmelinite structure.

As pointed out before, if gmelinite is fully dehydrated, cation C2 site (or better Na cations, as Na is the predominant extraframework atom) remains only three-fold coordinated. While three-coordinated magnesium occurs in dehydrated offretite (Mortier et al., 1975) and three-coordinated calcium in monoclinic polytype of tschernichite (Alberti et al., 2007), to our knowledge this is the first observation of three-coordination for Na in silicates.

The dehydration process of gmelinite is characterised by the remarkable displacement of two sites:

1. The shift of framework oxygen O1 towards cation site C1. The C1-O1 distance decreases from 3.27 Å at RT to 3.00 Å at 90°C, due to the loss of H<sub>2</sub>O in the W1 site, in order to reduce the electrostatic effect of C1 on O2 oxygens;
2. The shift of C2 cations O1 and O4 framework oxygens in the 8-ring channel in order to reduce the C2 bond distances in these sites as soon as possible. The C2-O1 distance decreases from 2.50 Å at 25°C to 2.38 Å at 90°C, the C2-O4 distance reduces from 2.90 Å at 25°C to at 2.82 Å 90°C.

It is worth noting that the occupancy of the C2 site is about 30%, so that only 0.3 charge units interact with the framework oxygens, whereas cations in C1 interact with the framework with one full charge. It is therefore easy to interpret the different coordination numbers for C1 and C2 as a consequence of the electrostatic effect of cations on the framework oxygens.

The shift of O1 towards C1 causes a rotation in the tetrahedron which reflects on the shape of all the rings of the framework:

- a) the 6-ring delimited by the oxygens O1 and O2, which at room temperature is strongly ditrigonal modifies towards a more hexagonal shape;
- b) the 8-ring accentuates its elliptical shape as the shortest axis, O1-O1, reduces by about 0.2 Å;
- c) the 12-ring assumes a more evident star-shaped form as the distances O1-O1 increase, whereas the distances O4-O4 decrease;
- d) the T1-O4-T1 and T1-O2-T1 angles accentuate their differences by 90°, the ideal value for a 4-ring, so that the 4-ring amplifies its rhombic shape. In fact, at RT O2 is 136.71° and O4 it is 148.37°, while at 90°C O2 is 141.49° and O4 it is 147.37°.

It is interesting to note that if in the framework of a natural zeolite is present a straight 12-ring channel, cations usually lie along the axis of the channel (for example; offretite (Alberti et al., 1996); mazzite (Galli, 1975); mordenite (Elsen et al., 1987; Simoncic and Armbruster, 2004); tetragonal (Alberti et al., 2002) and monoclinic (Alberti et al., 2007) polytypes of tschernichite) are fully solvated, whereas in gmelinite-Na, the cation C2 site is far from the centre of the channel and coordinates both water molecules and framework oxygens. A similar situation has recently been found in mazzite-Na from Boron, California (Arletti et al., 2005).

## **5.6) DISCUSSION OF EX-SITU DATA**

As seen above, gmelinite powder heated at  $T > 330^\circ\text{C}$  transforms into a new phase, AFI-type. The AFI-type topology was first found in an aluminophosphate material (AlPO-5), synthesised at 150°C from a hydrothermal system containing an aluminophosphate gel and tetrapropylammonium

hydroxide (Wilson et al., 1982). Its crystal structure was resolved by Bennett et al. (1983) by single crystal X-ray diffraction.

The topology of AFI materials can be described as columns of six-rings of tetrahedral in the sequence UDUDUD bonded to each other as in tridymite. These columns are connected through UDUD-type chains of 4-rings to delimitate 12-ring channels parallel to [001]. The topological symmetry is  $P6/mcc$  which is also the real symmetry of pure siliceous AFI-type SSZ-24 materials (Bialek et al., 1991) whereas the ordered distribution of Al and P in AlPO-5 lowers the real symmetry to the space group  $P6cc$ . As a matter of fact, the real AlPO-5 symmetry has been discussed by many authors. Mora et al. (1996) and Ikeda et al. (1999) found with the use of synchrotron and neutron powder diffraction respectively, that the most probable symmetry of calcined AlPO-5 is orthorhombic  $Pcc2$ , whereas, according to Ikeda et al. (1999) and Guo et al. (2005) its space group as a synthesised material remains  $P6cc$ . According to Klap et al. (2000) the crystal structure, determined by single crystal synchrotron X-ray diffraction data, can be described as consisting of three types of microdomains, each exhibiting  $P\bar{6}$  symmetry. According to Richardson et al. (1987) the powder pattern of AlPO-5 collected by neutron diffraction at 7 K shows complex features not interpretable on a single hexagonal cell.

A problem arises in the structure refinement of AFI-type materials. According to the framework topology  $P6/mcc$ , the  $T-O_m-T$  angle, where  $O_m$  is the framework oxygen lying on the mirror plane, is around  $180^\circ$ . Bennett et al. (1983) and Richardson et al. (1987) pointed out that this  $T-O_m-T$  is very near to  $180^\circ$  ( $178^\circ$ ), so, the displacement factor of this oxygen is anomalously large and the T-O distances are too short. These authors concluded that the position which had been attributed to the oxygen was the average of the positions occupied by it in reality. Klap et al. (2000) explained the presence of three microdomains with  $P\bar{6}$  symmetry as a consequence of the threefold disorder of  $O_m$ . Already in 1986 Alberti had evidenced that T-O-T angles of  $180^\circ$  which are absent in zeolites as such angles, or very near this value, are energetically unfavourable due to the partial covalency of the bond. As a result, the structure undergoes a lowering of symmetry and/or a splitting of the oxygen which results in the removal of the linear T-O-T angle.

This effect was clearly evident in the refinement of calcined SSZ-24 (Bialek et al., 1991) where  $O_m$  is split over two positions (with a distance between them of about  $0.8 \text{ \AA}$  and T-O-T angles of around  $160^\circ$ ).

Ruiz-Salvador et al. (1996) used the minimisation method and lattice dynamic calculations to identify stable minima for the structure of AlPO-5. They showed that the reduction of the symmetry of the structure from  $P6cc$  to  $P\bar{6}$  leads to the relaxation of the Al-O-P angles from the linear value, and found that the inclusion of a representation of the polarisability of the oxygen is essential in removing the linearity of the angle.

The ex-situ single crystal X-ray data collection mentioned earlier was used to study the structure of the AFI-type phase obtained by heating gmelinite-Na at over  $300^\circ\text{C}$ . Topological symmetry  $P6/mcc$  was assumed. The starting coordinates were taken from the framework model of Bialek et al. (1991) with  $O_m$  occupying a non-split site.

All hkl reflections were used for this structure determination. In spite of the quality of the experimental data, as shown in Figure 38, the reciprocal planes with l odd seem to be a haze of smoke rather than actual diffraction peaks, while regarding the very high R-factor (around 30%), an intelligible picture appeared with the distances and angles of the tetrahedron acceptably regular. An accurate analysis of  $F_o$  and  $\Delta F$  Fourier showed a new maximum (Si1P) at about a distance of approximately 1 Å from the tetrahedral cation site and symmetric with respect to the plane formed by the three framework oxygens parallel to the mirror plane. This maximum was interpreted as a new tetrahedral cation site.

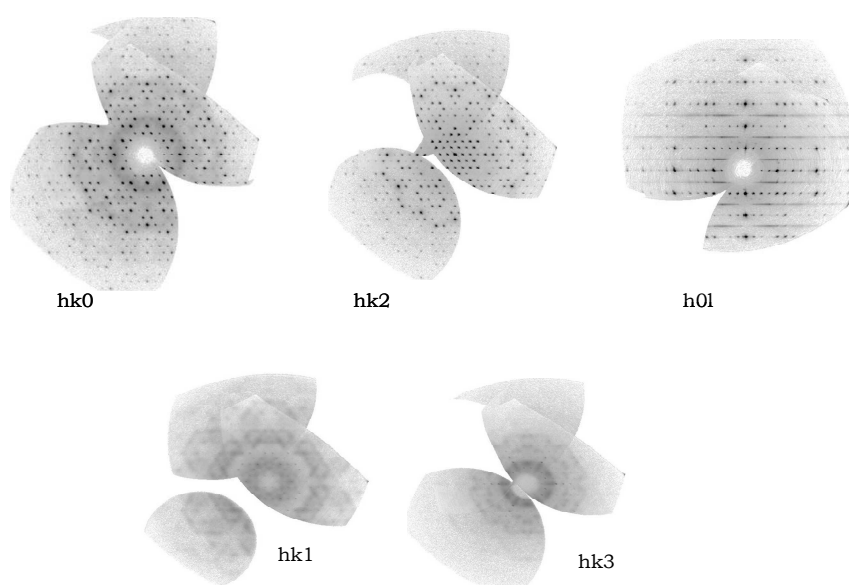


Figure 38: synthetic precession images of reciprocal planes in zeolites gmelinite after heating at  $T > 300^\circ\text{C}$

As seen above, in AFI-type materials the double 6-ring present in gmelinite is substituted by 6-rings of regularly alternated UDUDUD tetrahedral. Therefore we can describe the phase transformation  $\text{GME} \rightarrow \text{AFI}$  as a 'face sharing tetrahedra' process (Alberti and Vezzalini, 1983).

In this process a T-O-T bridge is broken and both tetrahedral cations migrate to generate new tetrahedra in which three vertexes are the same as before and the fourth is symmetric with respect to the mirror plane of the three vertices. In this way a new framework topology is created. Alberti and Martucci (2005) showed that phase transformation by heating which had been found to date in microporous aluminosilicates and aluminophosphates were always due to a 'face sharing tetrahedra' process.

It is worth noting that, in agreement with the findings of Bialek et al. (1991) on SSZ-24, the structure refinement indicates that the fourth vertexes of these tetrahedral are in their turn split over two new positions (with a distance among them of about 1 Å), thus confirming that linear T-O-T angles are energetically unfavourable.

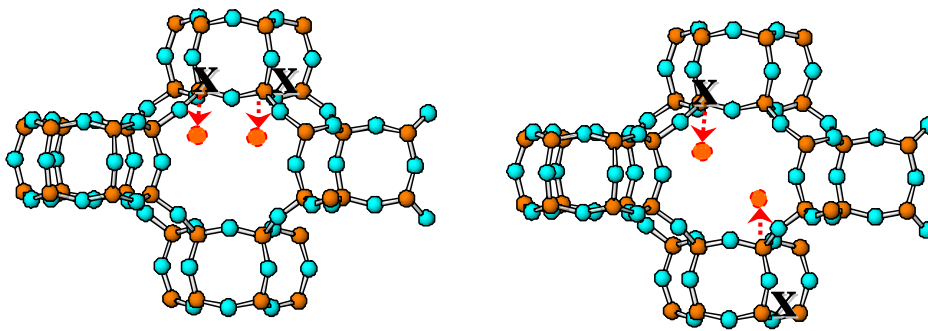


Figure 39: UU or DD errors in the UDUDUD regular alternation of the tetrahedra in the 6-ring.

These 'face sharing tetrahedra' cause errors, or antiphase domains, in the UDUDUD sequence in the 6-rings (Figure. 39). These errors can be an explanation for the diffuse streaks found in the  $hkl$  (with  $l$  odd) reciprocal planes, but cannot justify the presence of weak but well defined peaks in these planes, which indexes often correspond to those of systematic extinctions both in the  $P63/mmc$  symmetry of gmelinite and in the  $P6/mcc$  symmetry of AlPO-5.

For this reason and also considering the high value of R factor found for the refinement of this structure, refinement trials were carried out in the space groups  $P6cc$ ,  $P6$ ,  $P6/m$ ,  $P6/mmm$  both by using all the reflections or only those with  $l$  odd. In all cases, the refinements described a structure with the same main features as described earlier but with less accuracy. Therefore Tables 10 and 11 report the results given by the refinement in the AFI topological symmetry by using all the reflections.

The results of the refinement showed that framework cations are not randomly distributed over the two tetrahedra but one of these accounts for 70% of the total. Extraframework cations occupy two different positions, at the centre of the cage delimited by two 6-ring or distributed along the axis of the 12-ring. Four weakly occupied sites located inside the 12-ring were attributed to water molecules. It is worth noting that TG analysis performed on the sample heated at 350°C four days after the heating indicated a water loss of 13.5% and a dramatically lower value than the loss of 20% found for gmelinite-Na. This value is comparable with the findings of Kühl and Miale (1978) who found that a Na, Ca-gmelinite sample from Prospect Park, New Jersey, after calcination absorbs, at 25°C and 12 Torr, 13.8 gr of H<sub>2</sub>O per 100 gr. of dry zeolite, i.e. about 50% of the water content in the untreated mineral

## 5.7) DISCUSSION OF IN-SITU TIME-RESOLVED SYNCHROTRON POWDER DIFFRACTION DATA

The most important result of this data collection is that during the heating it was possible to recognise a transient phase between gmelinite and the AlPO type phase. As we can see by Figure 40, this phase appears in the temperature range 343-448°C. The structure of this phase is still unknown, but it was possible to obtain the cell parameters, thanks to the GSAS package.

Table 12 shows the unit cell parameters and symmetry of these three phases. Cell parameter  $a$  does not change remarkably in the phases, whereas parameter  $c$  dramatically shortens. The systematic absences in the powder pattern indicate that for this transient phase the space group is  $P6_3/mmc$  or one of its non-isomorphic subgroups ( $P6_3/mmc$ ,  $P6_3mc$ ,  $P-31c$  or  $P31c$ ). No inorganic data base reports a phase with these characteristics.

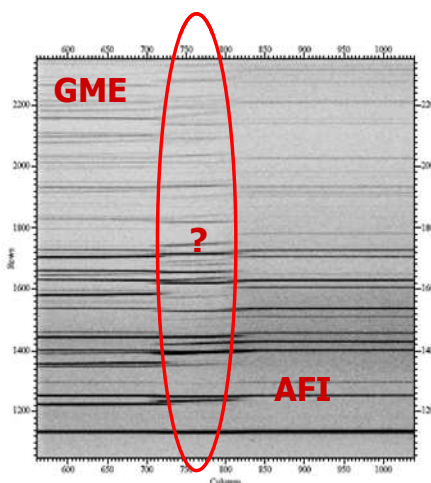
The first step of the phase transformation is the breaking of some T-O-T bridges in the D6R, possibly not regularly alternated, with the formation of a new phase where the value of parameter  $c$  is intermediate to those of gmelinite and AFI. However the new framework cation sites remain too far to give new T-O-T bridges. During a second step the decrease in parameter  $c$  allows the formation of these bonds, and the birth of the AFI structure.

An attempt to solve its crystal structure was therefore carried out by means of the program EXPO. Ambiguous and sometimes conflicting results were obtained, depending on the space group or on the strategy used to solve the crystal structure. However, it was evident that the framework is characterised by a high degree of disorder, with a very large number of interrupted T-O-T bridges. Unfortunately, a satisfactory model of the structure of this ‘transient’ phase was not obtained. The understanding of this structure could give important information about the mechanisms and kinetics of phase transformations.

	a	c	V	Space Group
Gmelinite 35°C "in situ" data	13.744(1)Å	10.055(1)Å	1644.9(1)Å <sup>3</sup>	$P6_3/mmc$
Unknown "transient" phase 343°C "in situ" data	13.969(1)Å	9.191(1)Å	1553.0(1)Å <sup>3</sup>	$P6_3/mmc$ ?
AFI-type phase 448°C "in situ" data	13.802(1)Å	8.495(1)Å	1401.5(1)Å <sup>3</sup>	$P6/mcc$

Table 12: Unit cell parameters of gmelinite, unknown phase and AFI-type phase.

Figure 40: GME → AFI transition



Note: Estimated standard deviations in parentheses refer to the last digit

Sample Name	GME-RT	GME-50	GME-75	GME-90	GME-75r	GME-25c	GME-25tr
<b>Temperature</b>	298 K	323 K	348 K	363 K	348 K	298 K	298 K
<b>a (Å)</b>	13.764(1)	13.728(1)	13.743(1)	13.783(1)	13.686(1)	13.656(1)	13.726(1)
<b>c (Å)</b>	10.078(1)	10.037(1)	10.045(1)	10.038(1)	9.992(1)	10.016(1)	10.049(1)
<b>Vol (Å<sup>3</sup>)</b>	1653.3(1)	1638.1(1)	1644.0(1)	1651.6(1)	1620.7(1)	1617.6(1)	1639.6(1)
<b>Space Group</b>			<i>P63/mmc</i>				
<b>Maximum 2θ</b>	72.2°	61.2°	70.0°	69.9°	69.9°	69.7°	73.4°
<b>Measured reflections</b>	13675	5663	10444	9739	9518	9515	2079
<b>Unique reflections</b>	1460	1014	1389	1379	1347	1334	1197
<b>Observed reflections &gt; 4σ</b>	1165	785	995	790	637	679	546
<b>Rint (%)</b>	4.04	4.06	5.07	6.04	12.02	12.03	8.08
<b>R1(%)</b>	4.01	4.02	7.06	4.09	6.00	5.04	5.06
<b>wR2(%)</b>	15.08	15.04	22.09	14.04	20.01	16.04	12.03
<b>Goof</b>	1.33	1.15	1.36	1.10	0,068	0,0674	1.09
<b>No. Of parameters</b>	62	62	52	44	44	46	62
<b>Largest diffraction peak and hole</b>	0.89/-0.73 e/Å	0.84/-1.10 e/Å	1.80/-0.88 e/Å	0.90/-0.80 e/Å	0.95/-0.53 e/Å	1.04/-1.58 e/Å	0.87/-0.54 e/Å

Table 7a: Lattice parameters and refinement details for gmelinite zeolite at 25, 50, 75, 90, 75r and 25c and 25tr°C, respectively

Sample Name	GME 100K
<b>Temperature</b>	100 K
<b>a (Å)</b>	13.743(1)
<b>c (Å)</b>	10.043(1)
<b>Vol (Å<sup>3</sup>)</b>	1642,7(1)
<b>Space Group</b>	<i>P3<sub>1</sub>c</i>
<b>Maximum 2θ</b>	35.0°
<b>Measured reflections</b>	6755
<b>Unique reflections</b>	4697
<b>Observed reflections &gt; 4σ</b>	3424
<b>Rint (%)</b>	6.04
<b>R1(%)</b>	3.08
<b>wR2(%)</b>	11.07
<b>Goof</b>	1.03
<b>No. Of parameters</b>	221
<b>Largest diffraction peak and hole</b>	0.62/-0.76 e/Å

Table 7b: Lattice parameters and refinement details for gmelinite zeolite at 100K

		<b>RT</b>	<b>50</b>	<b>75</b>	<b>90</b>	<b>75r</b>	<b>25r</b>	<b>25r-fin</b>
<b>T1</b>	x/a	0.4410(3)	0.43956(5)	0.43921(5)	0.43924(6)	0.43912(8)	0.44028(6)	0.44113(8)
	y/b	0.10562(3)	0.10482(4)	0.10476(5)	0.10528(6)	0.10500(8)	0.10521(6)	0.10576(8)
	z/c	0.09431(3)	0.09426(5)	0.09414(5)	0.09359(7)	0.0938(1)	0.09425(8)	0.0941(1)
	Uiso	0.0116(1)	0.0147(2)	0.0167(3)	0.0177(2)	0.0207(3)	0.0173(2)	0.0155(3)
<b>O1</b>	x/a	0.4169(2)	0.4206(2)	0.4234(3)	0.4257(3)	0.4253(4)	0.4190(3)	0.4170(3)
	y/b	0.20844(8)	0.2103(1)	0.2117(1)	0.2128(1)	0.2126(2)	0.2095(1)	0.2085(2)
	z/c	0.0607(2)	0.0586(3)	0.0561(3)	0.0521(3)	0.0541(4)	0.0588(3)	0.0603(4)
	Uiso	0.0298(4)	0.0381(6)	0.0429(8)	0.0415(8)	0.044(1)	0.0381(8)	0.033(1)
<b>O2</b>	x/a	0.8511(2)	0.8551(2)	0.8567(3)	0.8561(3)	0.8569(4)	0.8530(3)	0.8513(3)
	y/b	0.42557(8)	0.4275(1)	0.4284(1)	0.4281(1)	0.4284(2)	0.4265(1)	0.4256(1)
	z/c	0.0617(2)	0.0615(2)	0.0620(3)	0.0643(3)	0.0634(4)	0.0599(3)	0.0612(4)
	Uiso	0.0250(3)	0.0305(2)	0.0360(6)	0.0378(7)	0.040(1)	0.0307(7)	0.0276(9)
<b>O3</b>	x/a	0.4109(2)	0.40903(2)	0.4081(3)	0.4065(3)	0.4073(4)	0.4109(3)	0.4116(3)
	y/b	0.0651(2)	0.0660(2)	0.0669(3)	0.06987(3)	0.0688(4)	0.0654(3)	0.0660(3)
	z/c	1/4	1/4	1/4	1/4	1/4	1/4	1/4
	Uiso	0.0276(4)	0.0347(2)	0.0389(7)	0.038(8)	0.041(1)	0.0358(8)	0.0317(9)
<b>O4</b>	x/a	0.3557(1)	0.35274(5)	0.3512(2)	0.3592(2)	0.3522(3)	0.3544(2)	0.0356(2)
	y/b	0	0	0	0	0	0	0
	z/c	0	0	0	0	0	0	0
	Uiso	0.0288(4)	0.0326(2)	0.03613(7)	0.0377(7)	0.040(1)	0.0347(8)	0.0294(9)

Table 8a: Atomic coordinates and thermal parameters of framework atoms for gmelinite zeolite at 25, 50, 75, 90, 75r and 25c and 25rt°C, respectively.

		<b>RT</b>	<b>50</b>	<b>75</b>	<b>90</b>	<b>75r</b>	<b>25c</b>	<b>25r</b>
<b>C1</b>	x/a	1/3	1/3	1/3	1/3	1/3	1/3	1/3
	y/b	2/3	2/3	2/3	2/3	2/3	2/3	2/3
	z/c	0.0747(2)	0.0601(4)	0.0482(5)	0.0333(5)	0.0387(7)	0.0689(4)	0.0748(4)
	Frac	0.169(1)	0.156(2)	0.162(2)	0.166(2)	0.160(3)	0.16(1)	0,164
	Uiso	0.090(3)	0.050(1)	0.59(2)	0.06491(1)	0.065(2)	0.501(2)	0.043(2)
<b>C2</b>	x/a	0.1191(3)	0.124(5)	0.1317(7)	0.1433(9)	0.139(1)	0.1189(6)	0.1185(5)
	y/b	0.2381(5)	0.2489(6)	0.263(1)	0.287(2)	0.278(2)	0.238(1)	0.237(1)
	z/c	0.0691(7)	0.086(1)	0.094(2)	0.1197(2)	0.111(3)	0.073(1)	0.067(1)
	Frac	0.149(2)	0.140(8)	0.131(8)	0.167(5)	0.16(3)	0.143(1)	0.139(1)
	Uiso	0.0459(7)	0.112(1)	0.15(1)	0.29398(1)	0.267(22)	0.106(8)	0.092(7)
<b>W1</b>	x/a	0.1985(5)	0.210(1)	0.208(3)	-	-	0.2020(9)	0.1982(7)
	y/b	0.5454(5)	0.545(1)	0.537(5)	-	-	0.540(1)	0.5448(7)
	z/c	1/4	1/4	1/4	-	-	1/4	1/4
	Frac	1/4	0.162(4)	0.064(7)	-	-	0.205(1)	0.233(1)
	Uiso	0.061(2)	0.11260(0)	0.20(4)	-	-	0.123(5)	0.068(3)
<b>W2</b>	x/a	0.3387(6)	0.3341(2)	-	-	-	0.334(1)	0.33856(8)
	y/b	0.1694(2)	0.1670(8)	-	-	-	0.1671(6)	0.1693(4)
	z/c	-1/4	-1/4	-	-	-	-1/4	-1/4
	Frac	1/4	0.162(5)	-	-	-	0.191(1)	0.237(1)
	Uiso	0.134(3)	0.1832(0)	-	-	-	0.176(6)	0.139(4)
<b>W3</b>	x/a	0.1618(6)	0.149(2)	-	-	-	0.156(1)	0.1600(8)
	y/b	0.0809(3)	0.074(1)	-	-	-	0.0778(7)	0.0800(4)
	z/c	0.1200(1)	0.108(3)	-	-	-	0.103(6)	0.116(2)
	Frac	0.42(1)	0.24(1)	-	-	-	0.407(2)	0.464(1)
	Uiso	0.250(8)	0.4462(0)	-	-	-	0.49(5)	0.27(1)

Table 8b: Atomic coordinates, thermal parameters and site occupancies of extraframework atoms for gmelinite zeolite at 25, 50, 75, 90, 75r and 25c and 25rt°C, respectively

	<b>x/a</b>	<b>y/b</b>	<b>z/c</b>	<b>Ueq</b>
<b>Si1</b>	0.44073(5)	0.10581(5)	0.09439(5)	0.0127(1)
<b>Si2</b>	0.10552(5)	0.44108(5)	0.09423(5)	0.0112(1)
<b>Si3</b>	0.4410(5)	0.33479(5)	0.09339	0.0118(2)
<b>Si4</b>	0.33544(5)	0.44136(5)	0.09337(5)	0.0104(2)
<b>O1</b>	0.4167(4)	0.2072(4)	0.0577(4)	0.035(2)
<b>O1C</b>	0.2067(3)	0.4153(4)	-0.0598(5)	0.033(2)
<b>O2</b>	0.8507(4)	0.4256(3)	0.0589(3)	0.024(2)
<b>O2C</b>	0.1410(4)	0.5753(3)	-0.0581(4)	0.021(2)
<b>O3</b>	0.4119(4)	0.0604(4)	1/4	0.030(2)
<b>O3C</b>	0.3417(4)	0.4126(4)	-0.2498(2)	0.030(2)
<b>O4</b>	0.3547(4)	0.0015(4)	-0.0038(5)	0.029(2)
<b>O4C</b>	0.3577(4)	0.3562(4)	-0.0036(5)	0.030(2)

Table 8c: Atomic coordinates and thermal parameters of framework atoms for gmelinite zeolite at 100K

	<b>x/a</b>	<b>y/b</b>	<b>z/c</b>	<b>Sof</b>	<b>Ueq</b>
<b>Na1</b>	1/3	2/3	0.071(3)	1/3	0.029(4)
<b>Na1C</b>	2/3	1/3	-0.069(3)	1/3	0.040(7)
<b>Na2</b>	0.1357(9)	0.2506(8)	0.0717(1)	0.248(7)	0.091(6)
<b>Na2C</b>	0.2481(9)	0.1340(8)	-0.073(1)	0.241(7)	0.071(7)
<b>Na3</b>	-0.424(3)	-0.255(3)	0.243(3)	0.12199	0.137(9)*
<b>W1</b>	0.211(5)	0.540(6)	0.252(5)	0.445(9)	0.038(3)
<b>W1C</b>	-0.213(5)	-0.529(6)	-0.249(5)	0.4275(9)	0.070(8)
<b>W2</b>	0.335(1)	0.1388(8)	-0.258(1)	0.47(1)	0.08(1)
<b>W2C</b>	0.3196(1)	0.1331(8)	0.234(1)	0.33(1)	0.09(1)
<b>W4</b>	0.070(9)	0.1740(2)	0.025(2)	0.31(2)	0.140(15)
<b>W4C</b>	-0.102(9)	0.1717(2)	-0.021(3)	0.31(2)	0.134(15)
<b>W7</b>	0.504(4)	0.386(4)	-0.246(5)	0.136(12)	0.152(15)*
<b>W5</b>	0.174(3)	0.585(7)	0.25(11)	0.045(5)	0.020(6)*
<b>W6</b>	0.146(2)	-0.032(2)	-0.248(2)	0.052(5)	0.031(7)*
<b>W6C</b>	-0.213(2)	-0.020(2)	0.252(2)	0.115(7)	0.063(7)*

Table 8d: Atomic coordinates, thermal parameters and site occupancies of extraframework atoms for gmelinite zeolite at 100K (\*=Uiso)

	<b>25</b>	<b>50</b>	<b>75</b>	<b>90</b>	<b>75r</b>	<b>25r</b>	<b>25r_fin</b>
<b>Si1-O1</b>	1.6417(6)	1.634(1)	1.635(1)	1.638(1)	1.626(1)	1.628(1)	1.637(1)
<b>Si1-O2</b>	1.6567(8)	1.654(1)	1.654(1)	1.656(1)	1.644(1)	1.647(1)	1.650(2)
<b>Si1-O3</b>	1.6470(8)	1.637(1)	1.638(1)	1.639(1)	1.630(1)	1.637(1)	1.641(1)
<b>Si1-O4</b>	1.6394(6)	1.634(1)	1.640(1)	1.636(1)	1.627(1)	1.626(1)	1.635(1)

	<b>25</b>	<b>50</b>	<b>75</b>	<b>90</b>	<b>75r</b>	<b>25r</b>	<b>25r_fin</b>
<b>T1-O1-T1</b>	148.66(13)	150.02(18)	149.82(22)	148.32(23)	149.49(31)	149.12(22)	148.50(25)
<b>T1-O2-T1</b>	136.68(12)	139.02(17)	140.37(20)	141.49(22)	141.32(31)	137.23(20)	136.71(24)
<b>T1-O3-T1</b>	144.61(14)	145.43(19)	145.86(23)	146.64(24)	146.59(33)	145.08(24)	145.19(27)
<b>T1-O4-T1</b>	148.37(13)	146.40(17)	145.22(20)	147.02(21)	146.38(27)	147.49(21)	148.49(24)

	<b>25</b>	<b>50</b>	<b>75</b>	<b>90</b>	<b>75r</b>	<b>25r</b>	<b>25r_fin</b>
<b>C2-W3</b>	2.111(12)	2.282(3)	-	-	-	2.017(5)	2.06(2)
<b>C2-W2</b>	2.181(8)	1.931(1)	-	-	-	2.106(2)	2.2(1)
<b>C2-O1</b>	2.500(6)	2.506(1)	2.427(2)	2.393(2)	2.413(2)	2.517(1)	2.5(1)
<b>C2-W3 (x2)</b>	2.562(6)	2.588(1)	-	-	-	2.493(1)	2.54(1)
		2.852(6)	2.792(4)		2.792(1)	2.879(7)	
<b>C2-O4</b>	2.905(3)	x2	x2	2.286(1)	x2	x2	2.9(1)
<b>C1-W1 (x3)</b>	2.500(4)	2.541(9)	2.714(3)	3.002(4)	-	2.527(9)	2.49(1)
<b>C1-O2 (x3)</b>	2.593(2)	2.551(3)	2.519(4)	2.465(4)	2.475(6)	2.554(4)	2.59(1)
<b>C1-O1 (x3)</b>	-	-	-	-	3.008(5)	-	

Table 9: : Selected bond distances (Å ) and angles (°) within the framework of gmelinite

Sample Name	GME_ALPO
Temperature (°C)	330
a (Å)	13.843(1)
c (Å)	8.433(1)
Vol (Å <sup>3</sup> )	1399.50(1)
Space Group	<i>P6/mcc</i>
Maximum 2 $\theta$	60.1°
Measured reflections	7816
Unique reflections	729
Observed reflections > 4 $\sigma$	7816
R <sub>int</sub> (%)	8,3
R1 (%)	29.61
wR2 (%)	7,19
Goof	1,32
No. Of parameters	42
Largest diffraction peak and hole	0.75/-0.70 e/ Å

Table 10 : Lattice parameters and refinement details for gmelinite zeolite at 330°C

	x/a	y/b	z/c	sof	Uiso
<b>Si1</b>	0.447(3)	0.329(3)	0.186(4)	0,5	0.0325(8)
<b>O1</b>	0.210(3)	0.421(7)	1/4	0,5	0.045(2)
<b>O2</b>	0.360(1)	0	1/4	0,5	0.090(3)
<b>O3</b>	0.581(6)	0.420(6)	1/4	0,5	0.094(4)
<b>O4</b>	0.514(2)	0.353(2)	0	0,125	0.027(5)
<b>O4B</b>	0.493(9)	0.23(1)	0	0,125	0.19(3)
<b>Si1P</b>	0.463(2)	0.339(2)	0.316(9)	0,5	0.0227(6)
<b>O4P</b>	0.416(1)	0.313(1)	1/2	0,125	0.013(4)
<b>O4PB</b>	0.498(2)	0.373(3)	1/2	0,125	0.044(7)
<b>Na1</b>	2/3	1/3	0	0,08907	0.092(7)
<b>Na21</b>	0	0	1/4	0,1	0.35(3)
<b>X2</b>	0.24(1)	0.11(2)	0	0,11147	0.28(9)
<b>X3</b>	0.277(2)	0.097(2)	0	0,19702	0.067(7)
		-			
<b>X4</b>	0.124(3)	0.047(2)	0.070(4)	0,18803	0.055(8)
<b>Q2</b>	0.299(3)	0.227(3)	0	0,1	0.032(7)

Table 11: Atomic coordinates, thermal parameters and site occupancies of framework and extraframework atoms for gmelinite zeolite at 330°C

## 6.1) ZEOLITE OMEGA; STRUCTURAL AND CHEMICAL FEATURES

Omega zeolite is the synthetic counterpart of natural zeolite mazzite (framework code MAZ) whose structure was first described by Galli in 1974. It is a zeolite with a medium Al content (the Si/Al ratio is between 3 and 5). It was first synthesised at the end of the sixties by Union Carbide (Flanigen and Kellberg, 1966; Flanigen and Kellberg, 1967; Flanigen and Kellberg, 1980) almost at the same time as the synthesis of isostructural ZSM-4 by Mobil (Ciric, 1965; Ciric, 1968, Ciric and Ried, 1969).

These materials are usually crystallised at low temperatures (around 80-150°C) using TMA cations in the system (TMAOH)-NaOH-Al<sub>2</sub>O<sub>3</sub>-SiO<sub>2</sub>-H<sub>2</sub>O, where TMA is the tetramethylammonium cation (Aiello and Barrer, 1970; Bowes and Wise, 1971; Cole and Kouwenhoven, 1973 ; Perrotta et al., 1978 ; Di Renzo et al., 1992).

Both sodium and TMA ions take part in the crystallisation, but Na seems to play a more fundamental role in the synthesis of this zeolite. In fact, to date, Na is always present in the parent liquor, whatever organic template is used and also when the synthesis of zeolite omega is carried out in the absence of organics (Cannan and Wamer, 1987; Tsitsishvili and Charkviani, 1986).

Omega zeolite it is a large pore material known for its strong Brønsted acidity and its adsorption capacities for large molecular species, whose catalytic properties have been evaluated for gas-oil cracking (Perrotta et al., 1978) and hydrocracking (Cole and Kouwenhoven, 1973), aromatic alkylation (Flanigen and Kellberg, 1980; Ciric, 1965; Aiello and Barrer, 1970; Bowes and Wise, 1971) and isomerisation (Solinas et al., 1983), olefin hydration (Fajula et al., 1984), and paraffin isomerisation (Raatz et al., 1991).

The omega zeolite structure was first described by Barrer and Villinger in 1969, on the basis of X-ray powder diffraction and adsorption data. The crystal structure of zeolite omega was given by Martucci et al. (2003), who provided the missing evidence that zeolite omega presents the framework type (MAZ) as a natural mazzite. Crystal structure refinement carried out by Rietveld method demonstrated that the Barrer and Villinger model is incorrect even if many structural features are also present in the real omega structure.

The real symmetry of omega zeolite is  $P6_3/mmc$ , as in natural mazzite. Its framework consists of gmelinite-type cages (Figure 41) linked in parallel columns to the *c*-axis, which share their 6-membered rings of tetrahedra. Alternate columns are staggered by one-half of the period along the *c*-axis and are connected laterally by 5-rings to form a hexagonal assemblage of columns.

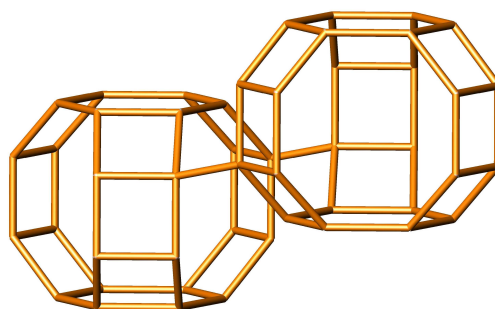


Figure 41: Gmelinite type cages

There are two different types of channels which are parallel to [001]: the largest channels are composed of 12-rings surrounded by gmelinite cages, while smaller channels are formed by distorted 8-rings between adjacent pairs of gmelinite cages (Figure 42). There are two crystallographically non-equivalent tetrahedral sites: one (in the general position with 24 atoms per unit cell) is in the gmelinite cage 4-membered rings, and is denoted as T2 (Galli et al., 1974; Galli, 1974; Galli, 1975; Rinaldi et al., 1975; Alberti, 1991; Alberti et al., 1981) or A (Klinowski, 1983, Massiani et al., 1988; Fyfe et al., 1985; Klinowski et al., 1986; Massiani et al., 1988; Buckermann et al., 1993) (or T1 by Goossens et al., 2000; Raatz et al., 1988), while the other, known as T1 [Galli et al., 1974 Galli, 1974, Galli, 1975; Rinaldi et al., 1975; Alberti, 1991; Alberti et al., 1981) or B (Klinowski et al., 1983; Massiani et al., 1988; Fyfe et al., 1985; Klinowski et al., 1986; Massiani et al., 1988; Buckermann et al., 1993] (or T2 by Goossens et al., 2000; Raatz et al., 1988), is in the gmelinite cage 6-rings (in a special position with 12 atoms per unit cell). In the following, I will use the notations given by Galli (1975) i.e. T1 for the tetrahedral site in the 6-ring, and T2 for the tetrahedral site in the 4-ring.

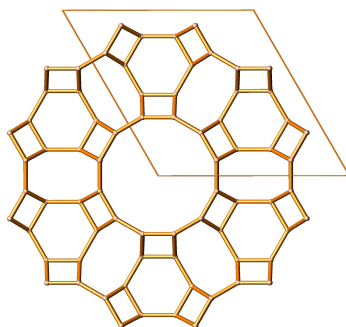


Figure 42: channels in omega zeolite

Na distribution in omega zeolite is similar to that found in mazzite. Sodium cations are distributed over two sites: one, the most populated site, is located in the 8-ring channel, it is 8-fold coordinated to six framework oxygens and two water molecules (NaI site); the residual Na cations are located along the axis of the 12-ring channel (NaII site), which coordinate nine H<sub>2</sub>O molecules (Martucci et al., 2003). While in mazzite the gmelinite cage is occupied by Na cations, in omega zeolite this cage hosts TMA molecules (as in offretite, TMA-sodalite and zeolite alpha) so that they cannot be easily extracted either by single cationic exchange or without provoking decomposition. TMA molecules have two possible orientations, which are symmetric to the plane passing through the centre and orthogonal to the threefold axis of the cage. Structure refinements have confirmed that TMA is only located inside the gmelinite cages, as stated in 1970 by Aiello and Barrer (Figure 43).

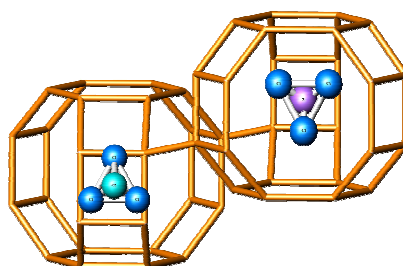


Figure 43: the location of TMA molecules inside the gmelinite cages

Recently, Martucci et al. (2007) studied the thermal behaviour of an as-synthesised omega sample by in-situ synchrotron powder diffraction. Structure refinements showed that TMA thermal degradation and dehydration processes are complete at about 550°C.

The Hoffmann degradation of TMA molecules causes permanent deformations in the framework and induces widening in the 8-ring channels and a star-shaped deformation in the 12-ring channels. The authors hypothesised the presence of residual protons on O2 framework oxygens due to TMA degradation on the basis of the narrowing of its T1-O2-T1 angle and the shift of this atom towards the centre of the gmelinite cage 6-ring. On the basis of these results, we have decided to perform a study on the ammonium form in order to observe the in-situ heating process and to have evidence about the formation of acid sites.

The advantage of studying the thermal behaviour of ammonium exchanged forms of zeolite omega is that ammonium-exchanged zeolites are widely used as precursors of catalytically active H-zeolites. In fact, by calcining ammonium-exchanged zeolite it is possible to obtain its acid form due to the expulsion of ammonium ions and template molecules, which while migrating create a charge imbalance which is equalised by protons attached to the framework oxygens. The ability to determine the types and concentrations of acid sites in zeolites is important for an increased understanding of structure/performance relationship in these materials.

Methods for the characterisation and quantification of acidic sites in solids are well-documented in the literature (Basila et al., 1964; Huges et al., 1967; Eberly, 1968; Liang and Gay, 1980; Dawson et al., 1981; Lunsford et al., 1985; Majors et al., 1986; Baltusis et al., 1986; Baltusis et al., 1987; Kofke et al., 1989; Peters, 1993; Sang and Chu, 1994; Maciel and Ellis, 1994) and most of these approaches involve the loading of a weak basic probe molecule onto a solid one followed by spectroscopic and/or thermal characterisation. One of the most commonly used techniques is pyridine/diffuse-reflectance IR spectroscopy (DRIFTS) (Basila et al., 1964; Huges et al., 1967; Eberly, 1968) which measures the qualitative amounts of Lewis and Brønsted acid sites in a given material (Rakiewicz et al., 1998). Several diffraction-based approaches have been used to determine the locations of Brønsted acid sites in zeolites and other silicates. Neutron diffraction is the most direct experimental method used to probe Brønsted acid siting because neutrons interact strongly enough with hydrogen nuclei to have a significant effect on Bragg peak intensities.  $^2\text{H}$  (deuterium) is the most desirable isotope for use in neutron diffraction experiments because it has both an unusually large coherent scattering cross section and a tolerably small incoherent scattering cross section. Early inferences were based on average Si-O bond lengths, as determined by X-ray diffraction, which are expected to increase upon protonation in proportion to the acid site occupancy factor. In  $\text{Ca}_3(\text{SiO}_3\text{OH})_2(\text{H}_2\text{O})_2$  (afwillite) and  $\text{Na}_2\text{H}_2(\text{SiO}_4)(\text{H}_2\text{O})_8$ , (disodium dihydrogensilicate tetrahydrate) for example, certain Si-O bonds were observed to be 0.08 Å longer than the others, on average, and were attributed to the formation of an acidic hydroxyl (Megaw, 1952; Jamieson and Dent-Glasser, 1966).

Based on these observations, Olson and Dempsey (1969) investigated T-O (T = Si, Al) distances in acidic zeolite Y (Si/Al = 2.3) via single crystal X-ray diffraction, compared them to those of acidic

faujasite zeolites, and concluded that the O1 and O3 sites were preferentially protonated while the other framework oxygens were not. Preferred acid sites correlate to preferred framework Al sites which they compensate. While it is difficult to distinguish between Si and Al using standard X-ray diffraction techniques, due to their similar scattering cross sections, Al occupancy can be inferred from average T-O distances (Alberti, 1990). The average T-O distance around a T-site that is preferentially occupied by Al will have an intermediate value between the ideal Si-O (1.61 Å) and Al-O (1.74 Å) distances (Ribbe and Gibbs, 1969; Jones, 1968).

The aim of this work is to give an exhaustive picture of the thermal behaviour of zeolite omega in its NH<sub>4</sub>-form, from RT to 800°C in order to observe the structural modifications induced by ammonium ion calcination using Rietveld structure analysis of temperature-resolved powder diffraction data collected using synchrotron radiation.

The study of the effect of dehydration on the crystal structure of zeolite-like materials has provided a number of results about the activation process induced by the calcination of ammonium forms or the decomposition of TMA molecules.

## **6.2) EXPERIMENTAL**

### **6.2.1) Material**

A sample of zeolite omega with the composition Na<sub>6.6</sub>TMA<sub>1.8</sub>(H<sub>2</sub>O)<sub>22.2</sub>[Al<sub>8.4</sub>Si<sub>27.6</sub>O<sub>72</sub>]-MAZ was synthesised at the Laboratoire de Matériaux Catalytiques et Catalyse en Chimie Organique, UMR 5618 CNRS, Montpellier, France. The synthesis of the zeolite omega was carried out in a stirred autoclave at 105°C from a synthesis batch of composition 0.48 Na<sub>2</sub>O/0.024 TMA<sub>2</sub>O/0.075 Al<sub>2</sub>O<sub>3</sub>/SiO<sub>2</sub>/26.6 H<sub>2</sub>O. The non-exchanged samples were the same as had been used for the in-situ study (Martucci et al., 2003). At the same laboratories, the sample was NH<sub>4</sub>-ion exchanged three times at room temperature and another three times at 90°C, in order to make the exchange as complete as possible. The chemical composition of the exchanged form was Na<sub>2.4</sub>TMA<sub>0.9</sub>(H<sub>2</sub>O)<sub>4.2</sub>(NH<sub>4</sub>)<sub>20.0</sub>[Al<sub>8.4</sub>Si<sub>27.6</sub>O<sub>72</sub>]. A thermogravimetric analysis was carried out in air using an STA 409 PC Luxx thermobalance, with a heating rate of 5°C/min, under a constant flux of air.

### **6.2.2) Experimental conditions**

The “in-situ” time resolved diffraction measurements were performed at the GILDA-BM8 beamline at the ESRF, Grenoble. The powder samples were loaded and packed into a 0.3 mm diameter Lindemann capillary open at both ends then horizontally mounted on a rotating goniometer head. The capillary was heated *in-situ* using a hot air stream equipped with a Eurotherm controller; a constant heating rate at 5°C/min was applied, and the samples were heated from 25°C to 940°C. The temperature was monitored using a thermocouple inserted at the heating gun opening. The

measurements were carried out using the translating image plate (TIP) experimental setup technique, i.e. during the heating treatment powder diffraction patterns were continuously recorded on a 4 mm slit-delimited portion of a 2D image plate which had a 2.5 pixel/c translating rate with respect to the temperature increase (Norby 1997).

Monochromatic incident radiation characterised by  $\lambda = 0.68881 \text{ \AA}$  was selected. The distance between the sample and the image plate was 204.7 mm and was determined by measuring the calibration procedure implemented in the FIT2D program. 59 wholly one-dimensional powder patterns were extracted from the image plate by integration onto 5°C-wide strips using an integration step of 10°C. The external standard LaB<sub>6</sub> was used to calibrate the wavelength, as well as to determine the zero-shift position, sample to detector distance, and tilting angle of the image plate detector.

### 6.2.3) Structure refinements

The structure refinements by full profile Rietveld analysis were performed in the  $P6_3/mmc$  space group using the GSAS package (Larson and Von Dreele, 1994) starting from site positions in framework atoms given by Martucci et al. (2003). Since no evidence was found to support a change in symmetry on the powder patterns until the amorphisation temperature, the same  $P6_3/mmc$  space group was adopted in all the crystal structure refinements. The Bragg peak profile was modelled using a pseudo-Voigt function with a 0.005% peak intensity cut-off. The instrumental background was empirically fitted using a Chebyshev polynomial of the first kind with 18 variable coefficients. The  $2\theta$ -zero shift was accurately refined in all the patterns of the data set. The scale factor was allowed to vary for all histograms. In the final cycles, the refined structural parameters for each data histogram were the following: fractional coordinates for all atoms, isotropic displacement and occupancy factors for extraframework sites and isotropic displacement factors (one for all tetrahedral cations, all framework oxygen sites, all Na cations, all water molecules and another for TMA molecules). Soft constraints were imposed on T-O distances during the initial cycles, and then released in the final cycles of refinement.

Structure refinements allowed us to observe how the heating process modified the occupancy of the extraframework sites.

Figure 44 shows the final observed and calculated powder patterns for zeolite omega at 50°C, 250°C, 430°C and 770°C. The refinement parameters are reported in Table 13, the refined coordinates in Tables 14a and 14b, bond distances and angles in Table 15.

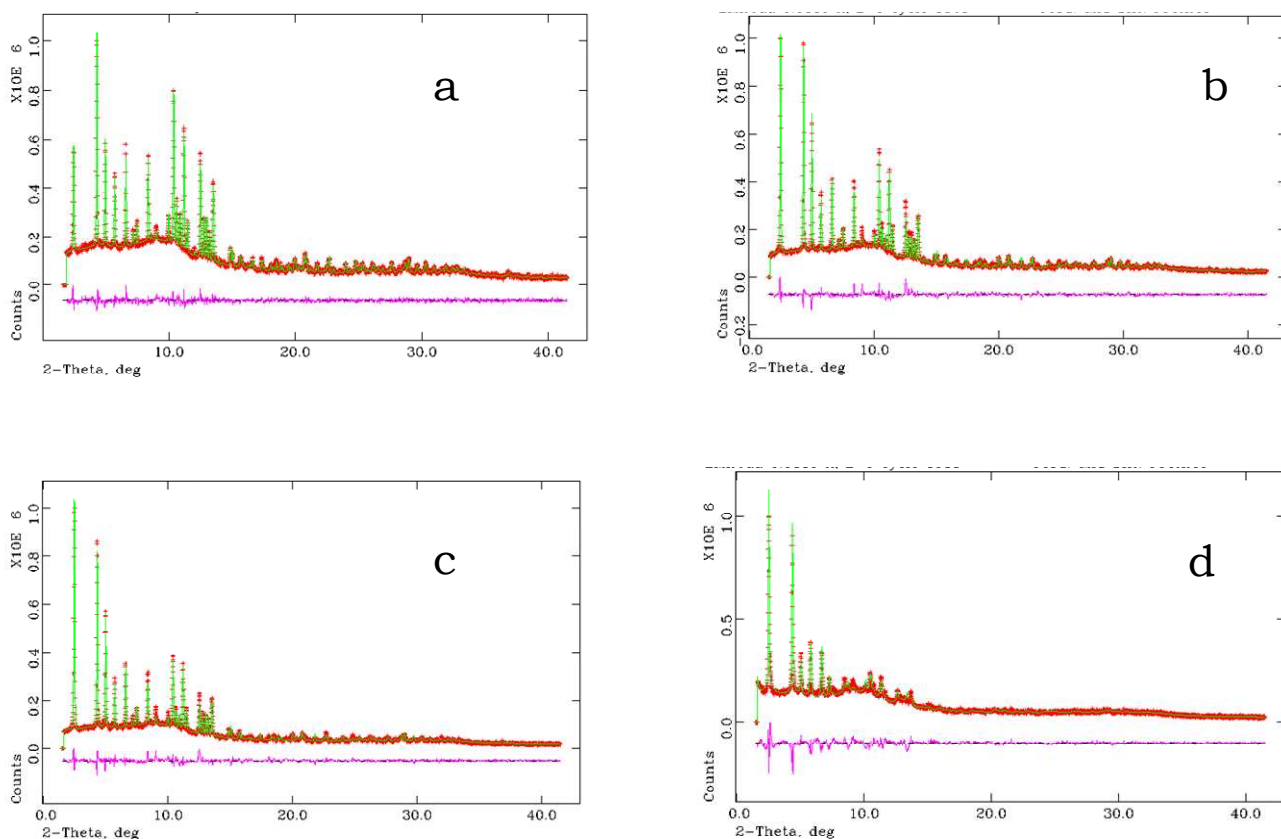


Figure 44 (a, b, c, d): final observed and calculated powder patterns for zeolite omega at 50°C, 250°C, 430°C and 770°C.

### 6.3) RESULTS OF STRUCTURE REFINEMENTS

#### 6.3.1) Crystal structure refinement of NH<sub>4</sub>-omega zeolite at room temperature

As has already been observed in as-synthesised omega, the symmetry after ammonium-exchange is hexagonal  $P63/mmc$  and the T1-O and T2-O average distances indicate a slight Al-enrichment in the T2 site (Table 15). Worth noting is the very wide T1-O<sub>2</sub>-T1 angle (173°, see Table 15) in the 6-ring zeolite omega gmelinite cage, which is almost identical to that found in the as-synthesised omega (176°) (Martucci et al. 2003), as well as in mazzite in its sodium (171°) (Arletti et al. 2005) and dehydrated mazzite (172°) (Rinaldi et al., 1975) - which is one of the widest found to date in zeolites. Since large T-O-T angles are expected to generate strong acidity in protic zeolites, by reducing the s character of the O-H bond (Rabo and Gajda, 1990) the exceptionally high T1-O<sub>2</sub>-T1 angle could provide a rationale for the presence of very strong Brønsted sites in ammonium-exchanged omega. On the contrary, the other T-O-T angle in the gmelinite cage 6-ring, T1-O<sub>1</sub>-T1, is narrower as in the as-synthesised omega (149° and 151°), respectively thus confirming the interaction of the extraframework ions located inside the gmelinite cage.

Structure refinements on data collected at room temperature have shown the extraframework content after the ion-exchange. As already discussed, in the precursor, the Na cations are

distributed over two positions: most of the Na (NaI) is located at the centre of the 8-membered ring, in a site between two gmelinite cages. The residual Na cations (NaII) are located in the middle of the 12-membered ring (Martucci et al., 2003). It is possible to note that after the ammonium-exchange, only half of the original sodium content (NaI site) remains. Na ions are eight-fold coordinated to six framework oxygens and two water molecules (W1) to form chains. All sodium localised at the centre of 12-ring has been completely exchanged with ammonium ions, so the NaII site is empty. On the whole, 2.4 Na ions per unit cell have been localised, in very good agreement with the chemical analysis, with respect to 2.4 Na ions found after the ammonium exchange.

As far as concerns the gmelinite-cage content, only 0.9 TMA molecules remain with respect to the original content (1.8 molecules) in good agreement with the chemical analysis. Ammonium ions occupy W5, W6 extraframework sites localised in the 12-ring and a new extraframework site called W7. The W1 site is attributed to residual water molecules, sandwiched between two Na cations in the 8-ring channel .

### 6.3.2) Refinement by in-situ X-ray data: temperature dependent unit cell variations

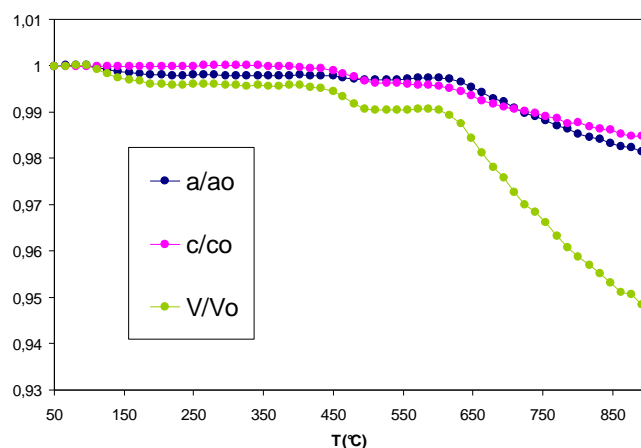


Figure 45: Temperature dependent variations in unit cell parameters

The variations in the unit cell parameters in the range 25-940°C, reported in Figure 45 suggest that the temperature-induced transformations can be schematised into the following steps:

- a) Temperature range 25°- 180°C.

This temperature range is characterised by small variations in the unit cell parameters. Up to about 100°C parameter *a* slightly decreases whereas *c* remains substantially unchanged; as a consequence we observe a small reduction in the unit cell volume.

- b) Temperature range 180°- 430°C.

In this temperature range, all parameters remain quite constant. As a consequence, the unit cell volume remains constant.

c) Temperature range 430°- 600°C.

A remarkable change in the unit cell parameters occurs in this range. Parameter  $a$  remains roughly constant, whereas a slope change is evident both in the variation of parameter  $c$  and the unit cell volume.

d) Temperature range 600°- 940°C.

In this range we observe a remarkable decrease in the cell parameters. It is worth noting that the crystal structure does not show any evidence of collapse until 940°C. The total volume decrease compared to the volume at room temperature is 5.86%.

### 6.3.3) Refinement by in situ X-ray data: temperature-dependent occupation of the extraframework sites

The structure refinements during the temperature ramp show large modifications in the occupancy of the extraframework sites, due to the processes of dehydration, removal of ammonium ions and degradation of TMA. The temperature dependence with regard to the occupation of the water and ammonium sites is illustrated in Figures 46 .

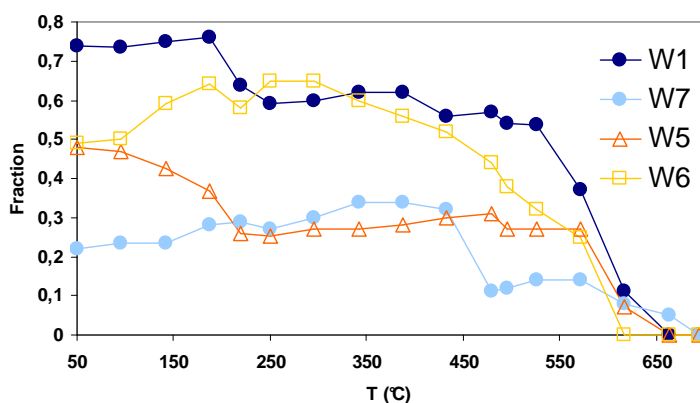


Figure 46: Evolution in the occupation of the water molecule and ammonium ion sites as a function of the temperature

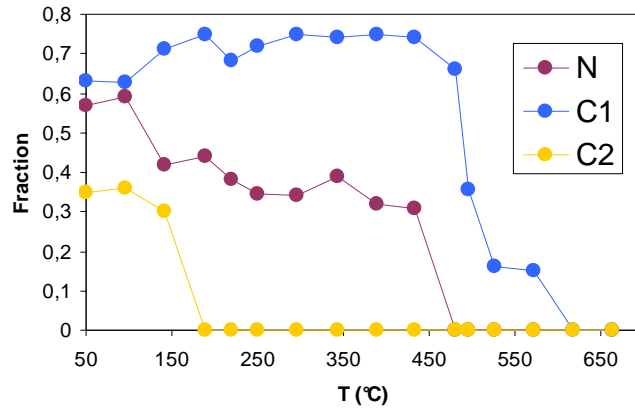


Figure 47: Evolution in the occupation of the template molecules sites as a function of the temperature

The dehydration process begins at about 200°C, when the W1 fraction begins to decrease. It is important to note that the W1 site remains highly occupied until high temperatures (~650°C), due to the fact that these molecules are strongly bonded to Na ions to the point of forming chains, and so are more difficult to remove from the 8-ring.

The loss of ammonium ions begins at 430°C and is completed at 650°C. It is interesting to observe an opposite trend for ammonium ions in the 12-ring which has been attributed to a partial migration between two partially occupied sites.

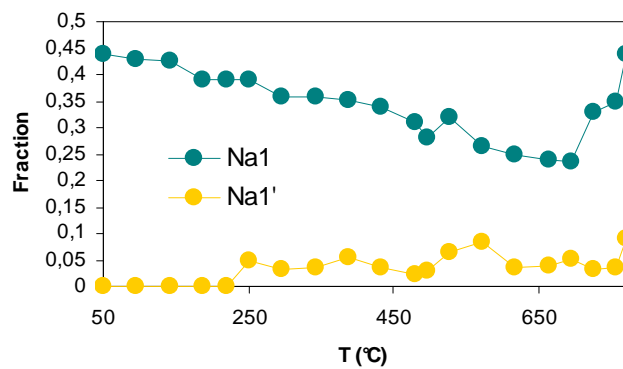


Figure 48: Evolution in the occupation of the sodium sites as a function of temperature

In Figure 48 it is possible to observe the variations in sodium sites during heating. The location of the Na1 site, in the 8-ring channels, is also affected by dehydration. As seen above, the Na1 site is eight-fold coordinated, with six framework oxygens and two water molecules (W1). At about 220°C, when the W1 site occupancy begins to decrease, sodium cations partially migrate towards a new position, called the Na1' site which is located near the wall of the gmelinite cage and five-fold-coordinated to O3, O4 and O6 framework oxygens. This migration is associated with the partial degradation of the TMA molecules which induce disorder in the position of the sodium cations and cause a decrease in the measured occupancy of the Na1 site. When the dehydration

process is complete, the Na1 site becomes fourfold coordinated to four O4 framework oxygens and maintains this coordination at high temperatures.

The variations in the occupancy of the TMA molecules as a function of temperature are shown in Figure 47. Structure refinements show that the state of the template is significantly altered at a relatively low temperature (about 180°C), when the C1 site is empty and N site occupancy is reduced by about 30%. This phenomenon represents the first step in the Hoffmann degradation process, which leads to the formation of protonated ammine. The transformation of a fraction of TMA into protonated trimethylamine severely disrupts the periodicity of the residual template molecules, with a consequent decrease in the measured occupancies. It is interesting to observe that the occupancy of the C1 site, which points towards the gmelinite cage 6-ring, is much less altered than the occupancy of the N site, at the centre of the cage, and the C2 site, which points towards the 4-rings of the cage.

TMA thermal degradation is completed in the 480–600°C temperature range, in correspondence with the emptying of N and C1 sites.

#### 6.3.4) Thermogravimetric analysis

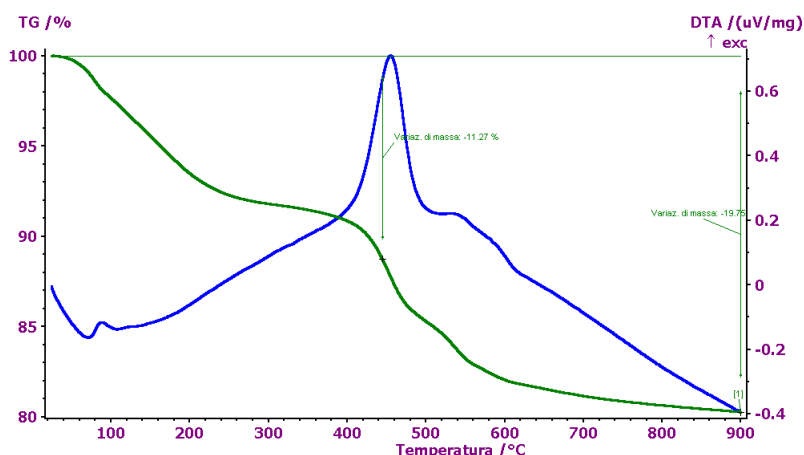


Figure 49: Results of thermogravimetric analysis

It is interesting to note that structural refinement shows results consistent with thermogravimetric analysis.

From the TG analysis curve (Figure 49) it is possible to observe a first step in weight loss of about 5% at about 200°C. This step is consistent with the early phase of Hoffmann degradation which, as seen above, begins at 180°C with the removal of C1, the onset of N removal, the beginning of the dehydration process and the removal of water molecules from the W1 site. This first step in dehydration also explains the change in the slope of the unit cell parameters curve. The second step in the TG curve is between the 400° and 600°C. It is the most important step in terms of weight loss, which is about 11%. This step corresponds to the definitive degradation of the template, the removal of ions from N and C2 sites (450 and 600°C respectively), and the definitive dehydration and calcination of the ammonium ions from the gmelinite cage and 12-ring channel.

This measure of weight loss is also consistent with the unit cell parameters curve, which shows a change in the slope in the 430-600°C range. The final weight at above 600°C essentially corresponds to the degradation of carbonaceous residues. On the whole, the total weight loss in the zeolite omega is 19.7% of its initial mass.

### 6.3.5) Refinement by in situ X-ray data: temperature-dependent deformation of the framework and evidence of formation of Brønsted acid sites.

Structure refinements during the thermal ramp provided information about how variations in extraframework site occupancy affect the geometry of the framework.

The most evident effect of the slow diffusion of TMA decomposition products is an expansion in the 8-ring, which develops significant internal pressure. The gmelinite cages are not in communication with the main 12-ring channels and the volatile products formed inside them have to diffuse along the 8-ring channels, occupied by the Na1 cation and W1 water molecule chains.

This process causes the deformation of the 8-ring channel which is defined by the distance between the O2–O2, O6–O6, and O4–O4 oxygens.

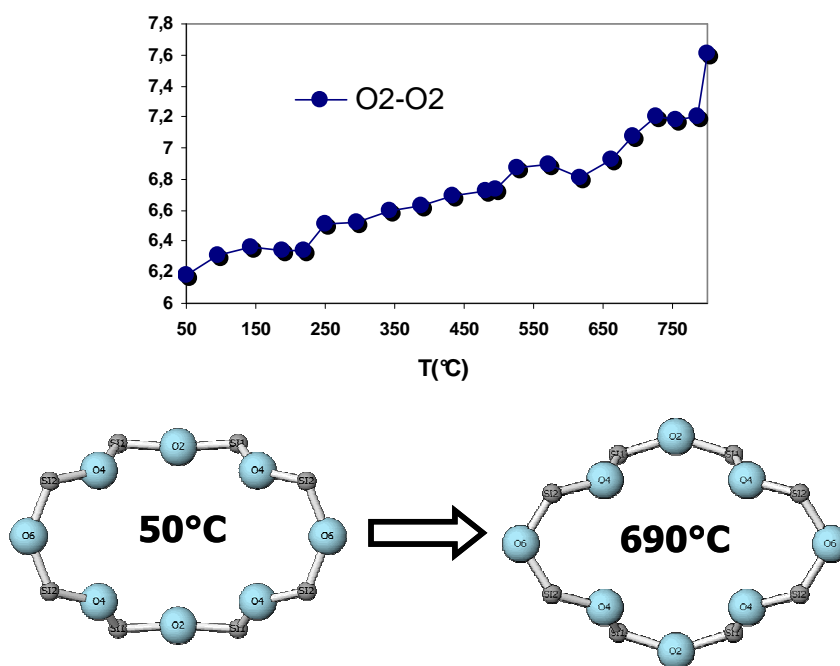


Figure 50: variations in the O2-O2 distances in the 8-ring channel and in the shape of the 8-ring channel

The evolution in the shape of the 8-ring during the thermal ramp is illustrated in Figure 50. The most important variation concerns the O2-O2 distance, as this distance limits the diffusion of the degradation products in the template, and the W1 and W7 ions.

The expulsion of the TMA degradation products causes an enlargement in the 8-ring, which reflects an increase in the O2-O2 distance. As a consequence, the eight-ring shape becomes more circular. This shape allows the degradation products to transit towards the exterior of the crystal more easily. It is important to note that the O2-O2 distance continues to increase also when the

TMA molecules have been completely expelled, so this distance goes from 6.18Å at 50°C to 7.6Å at 800°C (Table 15).

As a consequence of the O2-O2 increase, the Na1 site, which at room temperature was eight-fold coordinated, loses its coordination with O2 (Na1-O2= 3.44Å) and remains fourfold coordinated. The eight-ring deformation also influences the deformation in the gmelinite cage, and in particular in the gmelinite cage 6-ring. In correspondence with the deformation of this ring, the T1-O2-T1 angle (which at 30°C is near to 173°) (Figure 51), decreases during TMA expulsion, and is 120° at about 800°C. The latter angle is very narrow, even if not the narrowest found in dehydrated zeolites. In fact, a 114° T-O-T angle has been found in dehydrated natrolite (metanatrolite) (Baur and Joswig, 1996). A 116° Si-O-Si angle has also been found in bavenite, a framework similar to berillo-alumino-silicate (Cannillo et al., 1996) whereas angles near to 120° exist in other dehydrated zeolites, e.g. 122° in Ba-phillipsite (Sani et al., 2002) or 118° and 122° in epistilbite (Cruciani et al., 2003). The decrease in the T1-O2-T1 angle causes a shift in the O2 framework oxygen towards the centre of the gmelinite cage, as proved by the decrease in the O1-O2 distance shown in Figure 52.

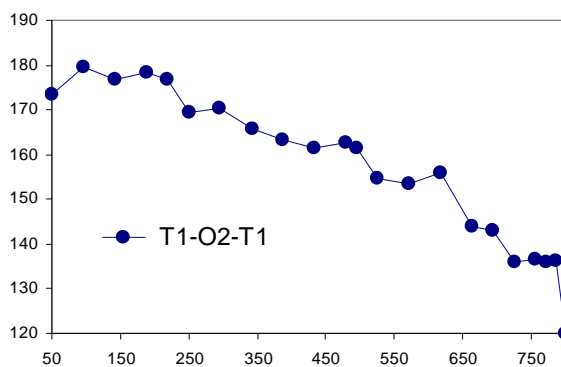


Figure 51: Variation in the T1-O2-T1 angle as a function of temperature

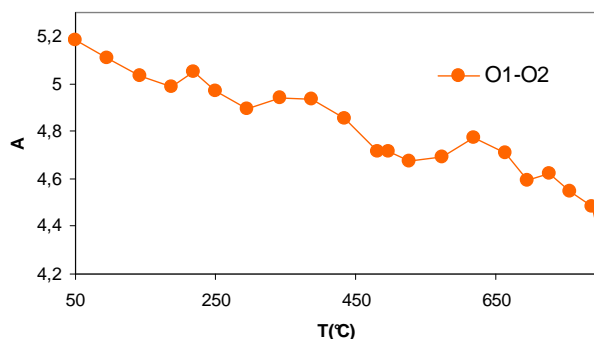


Figure 52: Variation in the O1-O2 distance as a function of temperature

My hypothesis is that this shift is guided by the presence of an O2-H Brønsted acid site, as a result of the presence of protons, residual to TMA Hoffmann degradation.

Eight-ring deformations also influence the shape of the 12-ring channel. Is it possible to observe that during the expulsion of the TMA and ammonium ions, the 12-ring tends to become more circular, due to an increase in the O5-O5 distance (from 10.91Å at 50°C to 11.37 Å at 694°C), while the O6-O6 distance remains quite constant .

However, the most important deformations in the 12-ring begin after the expulsion of the TMA molecules and ammonium ions. At  $T > 694^\circ\text{C}$  we can see a very strong inversion in this trend: the O5-O5 decreases from 11.37Å (at 690°C) to 9.61Å (at 720°C) whereas, the O6-O6 distance increases from 9.70Å (at 690°C) to 11.63Å at 720°C (Figure 53).

At the same time, the T-O-T angles centred on O5 and O6 undergo strong deformation (Table 15) and the 12-ring becomes star-shaped (Figure 54 and 55). Structure refinement clearly shows an increase in the T2-O5 bond distance from 1.6 to  $>1.8$  above  $800^\circ\text{C}$ . An explanation for this process is the presence of a proton bonded onto the O5 framework oxygen which compensates for the charge imbalance due to the removal of ammonium ions. When the temperature increases, the strongly inhomogeneous lengthening in the T2-O5 distance indicates that a dealumination process has occurred. The loss of crystallinity, as evidenced by the remarkable broadening of peak patterns at such temperatures, does not permit crystal structure refinement above  $770^\circ\text{C}$ .

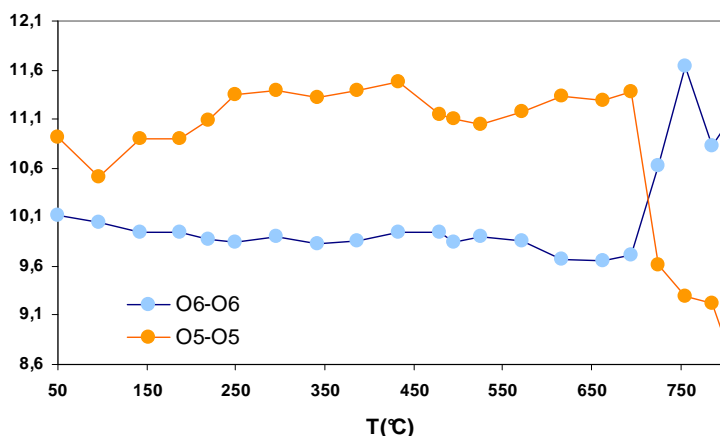


Figure 53: Variations in O-O distances in the 12 ring as a function of the temperature

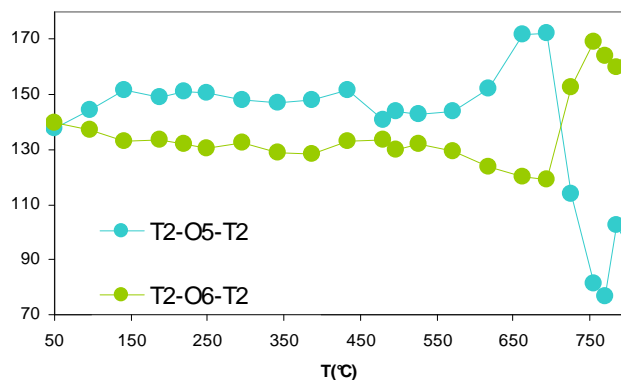


Figure 54: Variations in the T-O-T angles in the 12-ring as a function of the temperature

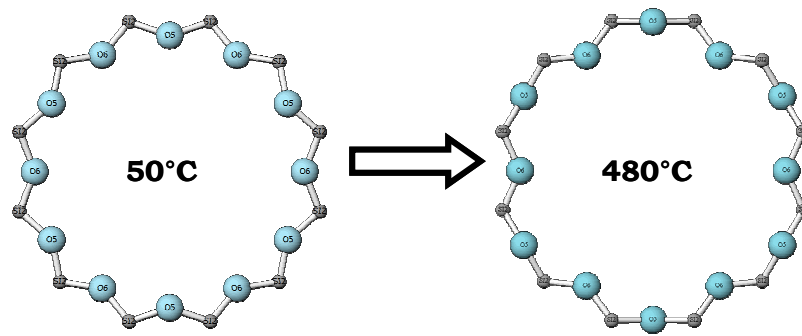


Figure 55: Variations in the shape of the 12-ring as a function of the temperature

For all tables: Estimated standard deviations in parentheses refer to the last digit.  
Site fractions are fixed to 1.0 for all framework atoms.

	<b>50</b>	<b>250</b>	<b>430</b>	<b>770</b>
<b>Space Group</b>	P6 <sub>3</sub> /mmc	P6 <sub>3</sub> /mmc	P6 <sub>3</sub> /mmc	P6 <sub>3</sub> /mmc
<b>a (Å)</b>	18.242(1)	18.203(1)	18.201(1)	18.066(1)
<b>c (Å)</b>	7.642(1)	7.641(1)	7.637(1)	7.555(1)
<b>V (Å<sup>3</sup>)</b>	2202.6(1)	2193.0(1)	2191.2(1)	2135.7(1)
<b>Refined pattern 2θ range (°)</b>	1.62 - 41.5	1.62 - 41.5	1.62 - 41.5	1.62 - 41.5
<b>R<sub>wp</sub>(%)</b>	6,05	7,55	8,11	9,72
<b>R<sub>p</sub>(%)</b>	4,65	5,71	6,62	7,48
<b>R<sup>2</sup><sub>F</sub>(%)</b>	8,51	16,51	17,73	12,23
<b>N<sub>obs</sub></b>	3967	3987	3995	3997
<b>N<sub>var</sub></b>	42	42	41	48

Table 13: Lattice parameters and refinement details for omega zeolite at 50, 250, 430, 770°C, respectively

Note: Synchrotron radiation:  $\lambda=0.68765(1)\text{Å}$

$$R_p = \frac{\sum(Y_{io} - Y_{ic})}{\sum Y_{io}}$$

$$R_{wp} = (\sum w_i(Y_{io} - Y_{ic})^2 / \sum w_i Y_{io}^2)^{0.5}$$

$$R^2_F = \frac{\sum |F^2_o - F^2_c|}{\sum |F^2_o|}$$

		<b>50</b>	<b>250</b>	<b>430</b>	<b>770</b>
<b>T1</b>	<b>x/a</b>	0.1597(3)	0.1576(3)	0.15771(3)	0.1564(12)
	<b>y/b</b>	0.4906(8)	0.4896(4)	0.4904(4)	0.4934(32)
	<b>z/c</b>	1/4	1/4	1/4	1/4
	<b>Uiso</b>	0.205(9)	0.021(21)	0.0218(24)	0.033(17)
<b>T2</b>	<b>x/a</b>	0.3558(2)	0.3535(2)	0.3550(2)	0.3645(20)
	<b>y/b</b>	0.0946(2)	0.0911(3)	0.0922(3)	0.1035(17)
	<b>z/c</b>	0.0472(5)	0.0472(5)	0.0478(6)	0.045(4)
	<b>Uiso</b>	0.205(9)	0.021(21)	0.0218(24)	0.033(17)
<b>O1</b>	<b>x/a</b>	0.2589(5)	0.2589(5)	0.2589(6)	0.2570(56)
	<b>y/b</b>	0.5180(9)	0.5178(10)	0.5177(1)	0.514(11)
	<b>z/c</b>	1/4	1/4	1/4	1/4
	<b>Uiso</b>	0.252(2)	0.027(4)	0.051(5)	0.13(4)
<b>O2</b>	<b>x/a</b>	0.4230(4)	0.4165(3)	0.4128(4)	0.4023(29)
	<b>y/b</b>	0.8462(8)	0.8330(6)	0.8256(7)	0.8046(58)
	<b>z/c</b>	1/4	1/4	1/4	1/4
	<b>Uiso</b>	0.252(2)	0.027(4)	0.051(5)	0.13(4)
<b>O3</b>	<b>x/a</b>	0.3871(6)	0.3839(7)	0.3861(8)	0.4062(47)
	<b>y/b</b>	0.0985(7)	0.0945(9)	0.0934(10)	0.1207(61)
	<b>z/c</b>	1/4	1/4	1/4	1/4
	<b>Uiso</b>	0.252(2)	0.027(4)	0.051(5)	0.13(4)
<b>O4</b>	<b>x/a</b>	0.4384(3)	0.4369(4)	0.4381(5)	0.4553(28)
	<b>y/b</b>	0.1131(4)	0.1086(5)	0.1088(6)	0.1190(41)
	<b>z/c</b>	-0.0726(8)	-0.0722(8)	-0.0715(10)	-0.050(4)
	<b>Uiso</b>	0.252(2)	0.027(4)	0.051(5)	0.13(4)
<b>O5</b>	<b>x/a</b>	0.1617(2)	0.1780(2)	0.1820(3)	0.1258(10)
	<b>y/b</b>	0.3235(5)	0.3599(5)	0.3639(5)	0.2515(19)
	<b>z/c</b>	-0.0098(13)	0.0043(17)	0.0111(21)	0.003(12)
	<b>Uiso</b>	0.252(2)	0.027(4)	0.051(5)	0.13(4)
<b>O6</b>	<b>x/a</b>	0.2773(5)	0.2703(5)	0.2732(7)	0.3255(83)
	<b>y/b</b>	0	0	0	0
	<b>z/c</b>	0	0	0	0
	<b>Uiso</b>	0.252(2)	0.027(4)	0.051(5)	0.13(4)

Table 14a: Atomic coordinates and thermal parameters in framework atoms for zeolite omega at 50, 250, 430, 770°C, respectively

		50	250	430	770
<b>NaI</b>	<b>x/a</b>	1/2	1/2	1/2	1/2
	<b>y/b</b>	0	0	0	0
	<b>z/c</b>	0	0	0	0
	<b>Frac</b>	0.44(1)	0.23(6)	0.34(8)	0.39(11)
	<b>Uiso</b>	0.195(2)	0.20(8)	0.2(8)	0.30(29)
<b>W5</b>	<b>x/a</b>	-0.0033(2)	0.1190(13)	0.1780(31)	-
	<b>y/b</b>	0.1303(1)	0.133(14)	0.0977(45)	-
	<b>z/c</b>	0.1024(23)	0.0320(68)	0.0426(71)	-
	<b>Frac</b>	0.475(5)	0.209(49)	0.300(63)	-
	<b>Uiso</b>	0.306(2)	0.306(58)	0.306(63)	-
<b>W6</b>	<b>x/a</b>	0.0914(2)	0.0790(10)	0.0817(13)	-
	<b>y/b</b>	0.1829(3)	0.1578(21)	0.1633(26)	-
	<b>z/c</b>	1/4	1/4	1/4	-
	<b>Frac</b>	0.488(20)	0.57(11)	0.525(113)	-
	<b>Uiso</b>	0.178(3)	0.178(42)	0.178(61)	-
<b>N</b>	<b>x/a</b>	1/3	1/3	1/3	-
	<b>y/b</b>	2/3	2/3	2/3	-
	<b>z/c</b>	-1/4	-1/4	-1/4	-
	<b>Frac</b>	0.5747(6)	0.27(23)	0.30(16)	-
	<b>Uiso</b>	0.024(2)	0.02(10)	0.02(11)	-
<b>C2</b>	<b>x/a</b>	1/3	-	-	-
	<b>y/b</b>	2/3	-	-	-
	<b>z/c</b>	-0.020(1)	-	-	-
	<b>Frac</b>	0.354(4)	-	-	-
	<b>Uiso</b>	0.063(4)	-	-	-
<b>W4</b>	<b>x/a</b>	0.5770(8)	0.5632(59)	0.5764(63)	-
	<b>y/b</b>	0.3490(7)	0.28(4)	0.2695(90)	-
	<b>z/c</b>	1/4	1/4	1/4	-
	<b>Frac</b>	0.220(21)	0.252(69)	0.329(80)	-
	<b>Uiso</b>	0.313(5)	0.314(98)	0.314(93)	-
<b>W1</b>	<b>x/a</b>	0.5300(8)	0.5299(14)	0.5227(17)	-
	<b>y/b</b>	0.0601(1)	0.0598(28)	0.0453(35)	-
	<b>z/c</b>	1/4	1/4	1/4	-
	<b>Frac</b>	0.739(18)	0.49(10)	0.565(114)	-
	<b>Uiso</b>	0.122(1)	0.116(39)	0.116(45)	-
<b>C1</b>	<b>x/a</b>	0.3016(2)	0.3054(20)	0.2999(24)	-
	<b>y/b</b>	0.6037(3)	0.611(4)	0.601(5)	-
	<b>z/c</b>	-0.148(4)	-0.111(7)	-0.088(6)	-
	<b>Frac</b>	0.631(4)	0.53(20)	0.75(18)	-
	<b>Uiso</b>	0.2981(3)	0.30(9)	0.298(7)	-
<b>NaI'</b>	<b>x/a</b>	-	1/3	1/3	0.04(4)
	<b>y/b</b>	-	2/3	2/3	0.36(5)
	<b>z/c</b>	-	-0.11(10)	0.0(6)	1/4
	<b>Frac</b>	-	0.08(30)	0.01(11)	0.13(17)
	<b>Uiso</b>	-	0.125(87)	0.06(31)	0.30(29)

Table 14b: Atomic coordinates, thermal parameters and site occupancies in extraframework atoms for zeolite omega at 50, 250, 430 and 770 °C, respectively

	50°C	250°C	433°C	770°C
<b>T1-O1</b>	1.620(6)	1.648(4)	1.645(5)	1.664(30)
<b>T1-O2</b>	1.630(6)	1.631(6)	1.631(5)	1.650(30)
<b>T1-O4 (x2)</b>	1.630(5)	1.646(28)	1.646(6)	1.655(6)

	50°C	250°C	433°C	770°C
<b>T2-O3</b>	1.642(6)	1.636(3)	1.642(7)	1.681(7)
<b>T2-O4</b>	1.649(5)	1.660(4)	1.658(4)	1.681(3)
<b>T2-O5</b>	1.627(6)	1.610(5)	1.622(4)	2.298(4)
<b>T2-O6</b>	1.640(6)	1.632(4)	1.633(5)	1.671(3)

	50°C	250°C	433°C	770°C
<b>T1-O1-T1</b>	149.2(15)	148.7(14)	149.7(17)	157.(15)
<b>T1-O2-T1</b>	173.5(10)	169.6(8)	161.5(10)	136.(8)
<b>T2-O3-T2</b>	141.5(7)	142.5(8)	140.4(10)	134.(6)
<b>T1-O4-T2</b>	143,6(7)	141.9(6)	141.4(7)	129.(5)
<b>T2-O5-T2</b>	137.8(6)	150.8(9)	149.1(11)	77.(11)
<b>T2-O6-T2</b>	139.5(7)	130.3(8)	133.1(10)	164.(11)

	50°C	250°C	433°C	770°C
<b>Gmelinite cage</b>				
<b>O1-O2</b>	5,18	4,97	4,85	4,54
<b>O3-O3</b>	5,91	5,95	5,84	5,48
<b>O4-O4</b>	7,64	7,64	7,63	7,56
<b>12-ring channel</b>				
<b>O5-O5</b>	10,91	11,35	11,47	9,3
<b>O6-O6</b>	10,12	9,84	9,44	11,63
<b>8-ring channel</b>				
<b>O2-O2</b>	6,18	6,58	6,69	7,18
<b>O4-O4</b>	5,71	5,58	5,55	5,33
<b>O6-O6</b>	8,13	8,36	8,25	6,43

Table 15: Selected bond distances (Å) and angles (°) within the zeolite omega framework at 50, 250, 430 and 770°C, respectively

## 7.1) FERRIERITE: STRUCTURAL AND CHEMICAL FEATURES

Ferrierite is a natural or a synthetic zeolite which is widely used as a catalyst in processes such as diffusion or adsorption thanks to its framework flexibility. It is a medium-pore material described as an excellent catalyst for various petrochemical reactions. The characteristic behaviour of this zeolite is its high conversion with low isobutene selectivity after a short time-on-stream, which is associated with the presence of strong acid sites (Xu et al., 1995, Finelli et al., 2002, Moiweer et al., 1993; Jirak et al., 1980). Synthetic ferrierite is also an important feedstock for the production of methyl tert-butyl ether (MTBE), which is a commercial oxygenate additive in unleaded motor fuel. The technological importance of synthetic ferrierite as a shape-selective catalyst is restricted to low-silica ferrierites, i.e. to materials with an Si/Al content of between 5 and 10.

Natural ferrierite is a rare zeolite mineral whose known occurrences are essentially restricted to filled vesicles in altered basalts and andesites (Wise and Tschernich, 1976), although one diagenetic occurrence in tuffaceous sediment has been reported (Regis, 1970).

The crystal structure of ferrierite was first resolved by Vaughan in 1966. It can be described by the gathering of a Secondary Building Unit 5-1. These SBUs form a framework characterised by two systems of mutually perpendicular channels (Figure 56). The first one is composed of one-dimensional channels delimited by 10- and 6-membered rings parallel to the *c*-axis and the other by 8-membered rings parallel to the *b* axis.

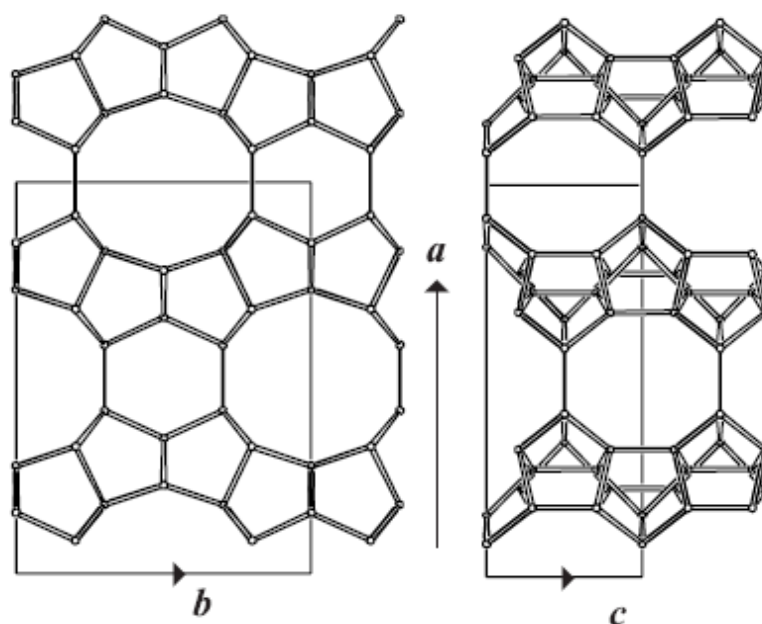


Figure 56: Parallel projections for unit cell content in FER viewed along *c* and *b*. The projections along *b* are equal.

The crystal structure of Mg-rich ferrierite, with apparent *Immm* symmetry (which is also the topological symmetry) was determined by Vaughan in 1966 and subsequently confirmed by Gramlich-Meier et al. in 1984. Mg-rich ferrierites are characterised by the presence of an  $\text{Mg}(\text{H}_2\text{O})_6^{2+}$  octahedron at the centre of the so-called 'ferrierite-cage' (Gramlich-Meier, 1984; Alberti and Sabelli, 1987) namely a  $[8^26^26^45^8]$  cage. The same *Immm* symmetry was used for Rietveld

refinements of K-exchanged (Pickering et al., 1989) and Kr-containing (Jones et al., 1995) synthetic ferrierites, using neutron and X-ray resonant powder diffraction, respectively. Although the *Immm* space group has been successfully used in Mg-rich ferrierite structure refinements, a lowering of the real symmetry can be detected. This lower symmetry has been proposed by Vaughan (1966) as a possibility which could be mainly due to the site symmetry  $\bar{1}$  of one of the bridging oxygen atoms, O5, in the case of *Immm* symmetry. This symmetry reduction has on the whole been ascribed to the movement of this bridging oxygen away from the inversion centre at  $\frac{1}{4}, \frac{1}{4}, \frac{1}{4}$  site in order to avoid  $180^\circ$  T-O-T bond angles. In fact, the real symmetry in natural ferrierite is reduced to *Pnmm* (Alberti and Sabelli, 1987) or *P2<sub>1</sub>/n* (Gramlich-Meier et al., 1985), depending on the extraframework cation content, and to *Pmnn* in synthetic all-silica ferrierite (Kuperman et al., 1993; Lewis et al., 1996; Weigel et al., 1996; Morris et al., 1994). Some years ago, Cruciani et al. (1998) performed synchrotron X-ray Rietveld refinements on low silica ferrierite in its as-synthesised, NH<sub>4</sub>-exchanged, and rehydrated H-forms in the *P2<sub>1</sub>/n*, *Immm* and *Immm* space groups, respectively. The monoclinic distortion in the as-synthesised form was explained by the strong interaction of the (K, Na) atoms, located near the centre of the 8-ring (I site), with the framework oxygens. When the I site is empty - as occurs in natural Mg-rich ferrierite (Vaughan, 1966; Gramlich-Meier et al., 1984; Alberti and Sabelli 1987), in all-silica ferrierite (Weigel et al., 1996), and in Kr-containing ferrierite (Jones et al., 1995) - the symmetry is strongly pseudosymmetric *Immm*. Neutron Rietveld refinements of synthetic low silica ferrierite in its acidic deuterium form (Martucci et al., 1999) were also performed in the *Immm* space group.

## 7.2) CATALYTIC PROPERTIES AND PROTON TRANSFER IN FERRIERITE

Acid zeolite catalysts are widely used in the chemical and petroleum industries for their catalytic activity, their remarkable reaction selectivity, and their excellent chemical and thermal stability. The principal acidity mechanism in these materials is the donation of Brønsted acid protons from bridging framework hydroxyls. The location and population of these hydroxyl groups in hydrogen zeolites provides a basis for the interpretation of their properties. For this reason, the protonated or deuterated forms of zeolites have long been a subject of research.

Martucci et al. (1999) used neutron powder diffraction to determine the number and location of hydroxyl groups in calcined D-ferrierite.

Despite the large efforts which have been devoted to these studies, knowledge on the interaction of Brønsted acid sites with polar molecules at atomic level is still incomplete. An area of great practical interest is the mechanism of proton transfer inside microporous channels in zeolites. Extensive theoretical studies have been carried out to address this problem. Proton transfer from Brønsted acid sites to water molecules adsorbed in the channels of a microporous solid acid catalyst to form a hydroxonium ion (H<sub>3</sub>O)<sup>+</sup> is now commonly accepted and demonstrated as possible by computational studies and infrared spectroscopy, whereas the reaction pathway of spontaneous proton transfer from a framework oxygen to another framework oxygen mediated by water is still debated.

For this reason, particular interest is focused in this work on rehydrated D-ferrierite to verify if:

1. in these form it is still possible to localise the two Brønsted acid sites recognised by Martucci et al. (1999) in D-ferrierite;
2. changes in the location and population of Brønsted sites in their acid hydrated form with respect to its anhydrous form arise;
3. water interacting with acid sites forms hydroxonium ions, hydrogen-bonded water, isolated water or free OH groups.

### 7.3) EXPERIMENTAL

Recently, synchrotron X-ray Rietveld refinements of a low-silica ferrierite in its as-synthesised and  $\text{NH}_4$ -exchanged forms, as well as its rehydrated H form, have been performed in the  $P2_1/n$ ,  $Immm$ , and  $Immm$  space groups respectively (Cruciani et al., 1998).

The same low-silica synthetic ferrierite (Engelhard ferrierite EZ<sup>TM</sup>-500, composition  $\text{K}_{2.7}\text{Na}_{1.1}\text{Al}_{3.8}\text{Si}_{32.2}\text{O}_{72} \cdot 12\text{H}_2\text{O}$ , and  $\text{Si}/\text{Al}=8.5$ ) was exchanged with  $\text{ND}_4\text{NO}_3$ , then washed with  $\text{D}_2\text{O}$  and dried overnight at  $96^\circ\text{C}$ , to obtain an intermediate  $\text{ND}_4$  form. The  $\text{ND}_4$  form was heated at  $550^\circ\text{C}$  for two hours in order to obtain its acid form (D-FER) by calcining ammonia ions ( $\text{ND}_3$ ). After calcinations, the sample was rehydrated in a glass box saturated with  $\text{D}_2\text{O}$  vapour (D<sub>2</sub>O-FER). A powder sample was put in a vanadium cylinder, sealed with indium wire and then collected at the ILL, Grenoble ( D2B beamline) at 2.25K (Figure 57).

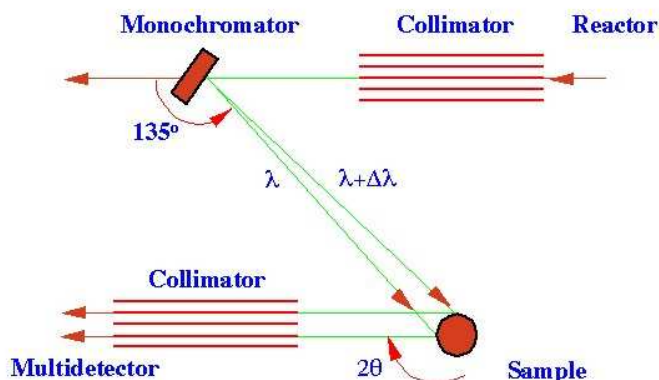


Figure 57: Diffraction line at the ILL (Grenoble)

Rietveld structure refinement was performed in the  $Immm$  space group using the GSAS package (Larson and von Dreele, 1994) starting from the structure model by Martucci et al. (1999)

Refinement soft constrains were applied at the initial stage, and were then released in the final cycles. The O-D distances were initially restrained to  $1.00\text{Å}$ , but in the concluding cycles these restrains were relaxed and both the coordinates and occupancies of the deuterium atom were allowed to refine independently. Extra-framework atoms were localised by Fourier maps and refined by least squares.

Crystallographic data and refinement details are reported in Table 16. Final atomic positions, thermal parameters and occupancies are given in Table 17a and 17b. Selected bond distances and angles within the framework for zeolite ferrierite are given in Table 18.

The final observed and calculated pattern is shown in Figure 58.

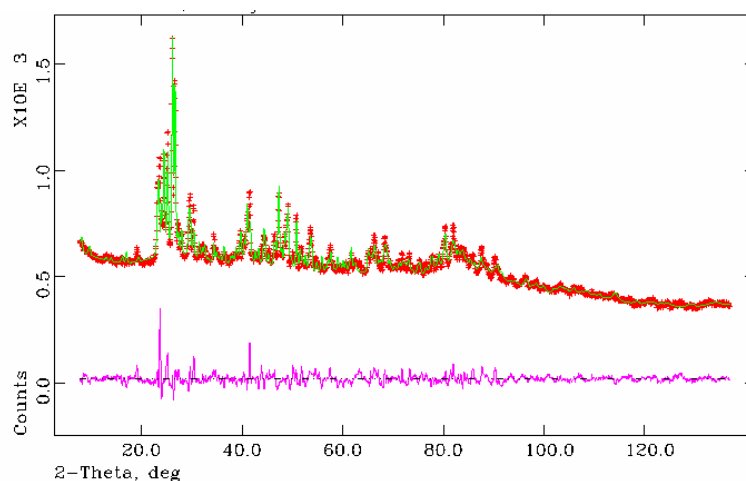


Figure 58: The final observed and calculated pattern of DFERD<sub>2</sub>O

#### 7.4) RESULTS OF STRUCTURE REFINEMENTS

As mentioned above, one of the great problems when studying crystal structure ferrierite is the determination of its real symmetry. A close inspection of the diffraction pattern in rehydrated sample has revealed the absence of reflection forbidden in the *I*-centring space group, and, consequently, the space group *Immm* was adopted.

The unit cell volume obtained by Rietveld cell parameter refinements is 1994.1(4) Å<sup>3</sup>, which is markedly greater than the as-synthesised sample ( $V = 1984 \text{ \AA}^3$ ), and slightly smaller with respect to the unit cell volume of NH<sub>4</sub>-form ( $V = 2001 \text{ \AA}^3$ ) (Cruciani et al., 1998).

Martucci *et al.* (1999) recognised two partially occupied Brønsted acid sites in the calcined deuterium form of ferrierite (D-FER). The first one, was localised on framework oxygen O4, between the T1 and T3 tetrahedron cations, facing towards the centre of the ferrierite cage. The second one, D2, was attached to framework oxygen O6, which is a bridge between two T4 tetrahedron cations, facing toward the 10-ring channel parallel to the [001] direction, not far from the centre of the ferrierite cage 8-ring facing toward the channel. These two deuterium sites were occupied in about 15% of cases. They had quite similar geometry and vibrated in large cavities.

In the D<sub>2</sub>O-FER sample, three acid sites were localised (see Table 17b). One of these, D1, which is bonded to the O4 framework oxygen, and facing towards the centre of ferrierite cage, is the same as in the acid form, with the same position and the same fraction. The second one, bonded to the O6 framework oxygen, corresponds to D2 in the acid form. In the D<sub>2</sub>O-FER sample, this site has a different orientation, facing towards the 8-ring channel parallel to [010], and its fraction is half (0.8) that of the acid form (0.15). The new acid site, D3, which is facing towards the centre of the

10-ring parallel to [001], is bonded to the O1 framework oxygens, which bridge two T2 tetrahedron cations, and is occupied in 32% of cases (see Figure 59). The narrowing of the angle on the O1 oxygen ( $149^\circ$ ), with respect to the D-form ( $166^\circ$ ) can confirm that the D3 site is attached to the O1 site. On the whole, 3.56 hydroxyl groups were recognised, as compared with the 3.8 Al atoms in the unit cell. According to the results by Alberti and Sabelli (1987), in a Mg-rich ferrierite among the tetrahedron sites, T2 (and T1 to a lesser extent, which are the two tetrahedron sites in the 6-ring) is the richest in Al, and T4 is the poorest.

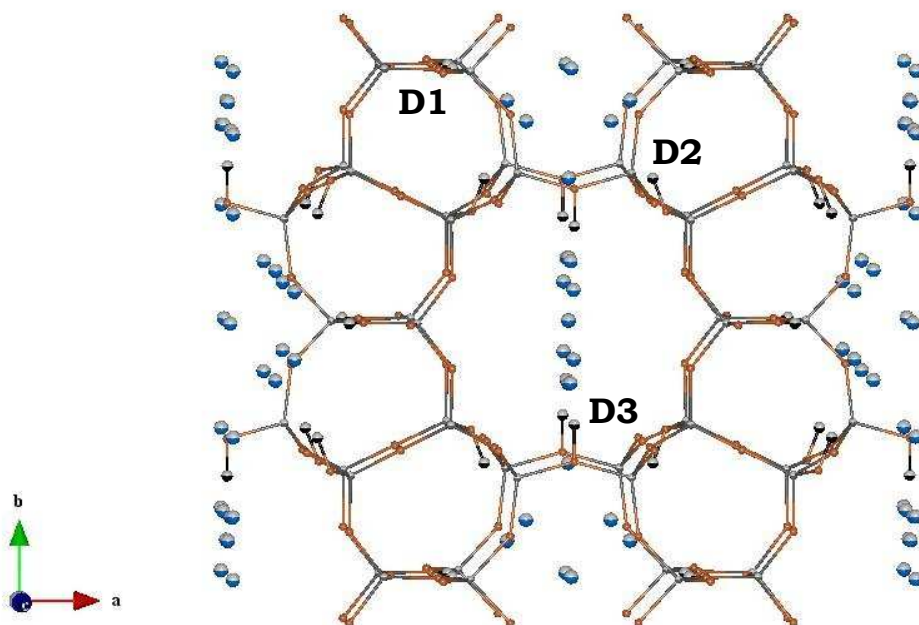


Figure 59: Location of Brønsted acid sites in the D-FER-D<sub>2</sub>O framework

Rietveld structure refinement on D<sub>2</sub>O-FER enabled us to accurately determine the location and occupancy of the water molecule oxygen sites. Eight extraframework sites were found, all of which had partial occupancy and large distances from the framework oxygens. The distances among many of these sites are too short for their simultaneous occupancy, but their partial occupancy allows an alternate presence of ions in these sites. It was not possible to also localise deuterium atoms in the D<sub>2</sub>O groups. This result has been interpreted as due to a partial disordering in the orientation of the water molecule. Such disorder could explain why D atoms were not found for the other water molecules.

In conclusion, the absence of a Brønsted acid site on the framework oxygen O1 and the higher deuterium occupancy on framework oxygen O6 in acid dehydrated ferrierite (Martucci et al. 1999) and the findings of a new Brønsted site in rehydrated ferrierite can be interpreted as a proton transfer mediated by water inside the channel of ferrierite. The mechanism of proton transfer inside microporous channels in zeolites is of great practical interest for understanding the catalytic properties of these materials.

## 7.5) DISCUSSION

Extensive theoretical studies have been carried out to address this problem. Proton transfer from Brønsted acid sites to water molecules adsorbed in the channels of a microporous solid acid catalyst to form hydroxonium ions ( $\text{H}_3\text{O}^+$ ) is now commonly accepted and demonstrated as possible by computational studies and infrared spectroscopy, whereas the reaction pathway of spontaneous proton transfer from a framework oxygen to another framework oxygen mediated by water is still being debated.

This work has demonstrated using neutron diffraction that this last proton transfer is possible and occurs in ferrierite D-forms.

To demonstrate this proton transfer we must follow three steps:

- localise the Brønsted acid groups and determine the population of the protons in the acid anhydrous form
- experimentally verify the presence of hydroxonium ions in acid hydrated forms
- demonstrate the changes in Brønsted site location and populations in acid hydrated forms with respect their anhydrous forms

1. Several studies on protonated or deuterated samples of zeolite Y, RHO, mordenite and chabazite (Olson and Dempsey, 1969; Mortier *et al.*, 1976; Bosacek *et al.*, 1981; Czjzek *et al.*, 1992; Baur *et al.*, 1987; Fisher *et al.*, 1988; Mortier *et al.*, 1975; Mortier *et al.*, 1979; Smith *et al.*, 1997; Martucci *et al.* 2000) have been carried out by X-ray or neutron diffraction in order to obtain the Brønsted acid sites locations and populations.

Neutron diffraction is the most direct experimental method used to probe Brønsted acid siting since neutrons interact strongly enough with hydrogen nuclei to produce a significant effect on diffracted intensities. Deuterium is the isotope which is usually used in neutron diffraction experiments because of its large coherent scattering cross section and tolerably small incoherent scattering cross section. Neutron powder diffraction experiments have therefore been performed by many authors (Olson and Dempsey, 1969; Mortier *et al.*, 1976; Bosacek *et al.*, 1981; Czjzek *et al.*, 1992; Baur *et al.*, 1987) to localise acid  $^2\text{H}$  sites and determine their occupancy in numerous dehydrated acid zeolites.

2. The ability of Brønsted acid sites to react with adsorbed water molecules in order to form hydroxonium ions,  $\text{H}_3\text{O}^+$ , has been studied by many authors by means of a variety of experimental techniques and computational methodologies.

The formation of hydroxonium ions has been envisaged for many years (Barrer and Klinowski, 1975) but still today an unambiguous indication of its presence has not reached. Infrared spectra obtained for a loading level of one water molecule per Brønsted site have been interpreted as due either to the formation of a hydroxonium ion (Marchese *et al.*, 1993) or to a neutral hydrogen-bonded complex (Wakabayashi *et al.*, 1996) or the simultaneous presence of both species (Czjzek *et al.*, 1992; Fischer *et al.*, 1987, Smith *et al.*, 1997; Parker *et al.*, 1993) or the presence of  $\text{H}_5\text{O}_2^+$  or  $\text{H}_7\text{O}_3^+$  clusters (Sauer and Haase, 1994).

The effect of water molecule adsorption on bridging hydroxyl groups has also been studied using  $^1\text{H}$  MAS NMR measurements (Hunger *et al.*, 1991; Batamack *et al.*, 1993; Batamack *et al.*, 1991).

The results indicate the simultaneous presence of hydroxonium ions and hydrogen-bonded H<sub>2</sub>O up to a level of one water molecule per Brønsted site. Moreover, the shift in the <sup>1</sup>H NMR of bridging OH groups can be interpreted as a fast proton exchange between water molecules, bridging OH groups and hydroxonium ions (Hunger et al., 1991).

Neutron inelastic scattering has been used to study the adsorption of water, at low loading, in H-mordenite (Jobic et al., 1992) and H-ZSM-5 (Jobic et al., 1996). In H-mordenite after water adsorption, the observed vibrational features are assigned to hydroxonium ions, H<sub>2</sub>O hydrogen-bonded, and free hydroxyl groups, whereas in H-ZSM-5 hydroxonium ions have not been found and a water molecule is attached to an acid site via two hydrogen bonds. Stuckenschmidt et al. (1996) detected the presence of H<sub>3</sub>O<sup>+</sup> groups in calcined and rehydrated ammonium-natrolite using single crystal X-ray diffraction data. In reality, H atoms were localised only for two of the four possible H<sub>3</sub>O<sup>+</sup> group, so that the presence of hydrogen-bonded water molecules or isolated water cannot be excluded in this material. X-ray and neutron diffraction refinements of partially dehydrated Na,H<sub>3</sub>O-X zeolite (Zhu et al., 1999) revealed the presence of hydroxonium ions which assumed very interesting configurations; isolated H<sub>3</sub>O<sup>+</sup> molecules where each deuteron hydrogen bonds to a framework oxygen, and (H<sub>3</sub>O<sup>+</sup>)<sub>2</sub>H<sub>2</sub>O(Na<sup>+</sup>)<sub>2</sub> clusters.

Many computational studies have been performed in order to study the interaction of water molecules with H-zeolites (Demuth et al., 2001, Stich et al., 1998, Termath et al., 1998). These calculations indicate that a structure is energetically more stable in the presence of neutral adsorption complexes, while the hydroxonium ions correspond to a transition structure for proton exchange. The low proton affinity of water (Benco et al., 2000) is seen as an obstacle to the protonation of water in H-zeolites. However, some of the studies cited earlier have provided evidence for protonated H<sub>2</sub>O. This discrepancy can be overcome by considering that the calculated proton affinity of water dimers and trimers (806 and 853 kJ mol<sup>-1</sup>) are by far larger than those of water molecules (694 kJ mol<sup>-1</sup>) and can be compared with that of ammonia (858 kJ mol<sup>-1</sup>) which is always protonated in any H-zeolite. Molecular dynamic simulations have shown that for two water molecules per framework hydroxyl group, hydrogen bonded H<sub>2</sub>O and protonated dimers were found, with small energy differences between them. Moreover, the H<sub>2</sub>O(H<sub>3</sub>O)<sup>+</sup>H<sub>2</sub>O trimer is a local energy minimum and “frequent proton jumps between the water trimer and the zeolite occur” (Zygmunt et al., 1996). Nusterer et al. (1996), investigating the interaction of water with low-aluminium sodalite using Molecular dynamic simulations found that for one H<sub>2</sub>O adsorbed at an acid site, the water molecule forms a strong hydrogen bond with the Brønsted site, for two H<sub>2</sub>O adsorbed, the Brønsted proton is removed from the framework to form an (H<sub>5</sub>O<sub>2</sub>)<sup>+</sup> cluster, whereas for three H<sub>2</sub>O per acid site, the acid proton is transferred from the zeolite framework to the next water molecule and it jumps to one of the other two water molecules.

In conclusion, from experimental results it was not possible to have an unambiguous indication of the presence of a neutral complex, in which the proton stays at the active site but binds with a water molecule (H<sub>2</sub>O), or an ion pair, in which the proton is transferred from the Brønsted site to the water molecules, forming a hydroxonium ion (H<sub>3</sub>O<sup>+</sup>) or larger (H<sub>5</sub>O<sub>2</sub>)<sup>+</sup> or (H<sub>7</sub>O<sub>3</sub>)<sup>+</sup> clusters, whereas computational methods favour the formation of charge clusters like (H<sub>5</sub>O<sub>2</sub>)<sup>+</sup> or (H<sub>7</sub>O<sub>3</sub>)<sup>+</sup>.

3. In the previous section, the proton transfer between zeolitic Brønsted proton and water molecules or water clusters were considered, as well as proton transfer between water molecules

in the same cluster. Experimental and theoretical studies suggest that an acid proton is not fixed to a specific zeolitic site: rather it “hops” or migrates from one site to another neighbouring site. In acid zeolites two types of proton motion have to be distinguished: a) on-site jumping between two oxygen atoms of the same Al-tetrahedron; and b) translational, inter-site motion between the oxygen atoms in two different Al-tetrahedra (Zygmunt et al., 1996). This proton transfer can occur in a dry H-zeolite or in a more or less hydrated H-zeolite. The proton jump energy barrier is the first parameter which has to be determined in order to follow the mobility of the acid protons on Brønsted sites. Energy barriers are related to the proton affinity in the framework oxygen atoms, which in turn depend on the framework type and Si-Al distribution. As a general rule, an oxygen which bridges two Si cations has a lower proton affinity than an oxygen in an Al<sup>(+)</sup>-O-Si site.

Many authors have tackled the problem of the proton jump energy barrier by density functional theory (DFT) calculations. Proton jump barriers have been calculated in dry H-ZSM-5 for translational protons moving through the zeolite lattice between two neighbouring Brønsted sites as a function of their separation distance.

For on-site proton jumping, the calculated barriers vary in the range of 60-100 kJ mol<sup>-1</sup> for CHA, FAU and MFI structures (Islam et al., 2001), whereas the proton jump barriers experimentally determined by <sup>1</sup>H NMR technique are significantly lower than the calculated ones (Fois and Gamba, 1999).

In dehydrated zeolites translation, proton motion through the zeolite lattice appears to be much less likely since the protons have to leave the Al-O-Si site and move to the new Si-O-Al site using an intermediate jump to an Si-O-Si site which has a lower proton affinity. The barrier for proton transfer from its AlO<sub>4</sub> site to the new AlO<sub>4</sub> site along an Si-O-Si path (Bull et al., 1993) has been evaluated by DFT calculation at around 200 kJ mol<sup>-1</sup>. This value is about twice that derived from experiments. Ryder et al. (2000) showed that “an experimental undetectable quantity of water can significantly affect the kinetics of proton migration, thus water-assisted proton transfer provides a kinetically favourable alternative mechanism for proton migration about the Brønsted acid site”.

These results demonstrate that a proton transfer mediated by water is not only possible but also probable. However, for this transfer to be reliable it is necessary for water molecules sites to be located at a coordination distance from framework oxygens O6 and O1, and that these water molecules form a water polymer to allow the transfer of a Brønsted deuterium from O6 to a water molecule at a coordination distance from O6, and by means of proton migration thorough water polymer molecules, it can thus be transferred from a polymer molecule in framework oxygen O1. In the previous sections, we reported that eight water molecules sites have been recognised in deuterium rehydrated ferrierite. An examination of the bond distances among them shows that many water polymers are possible, in particular the trimer W7-W5-W4 with bond distances W7-W5=2.62Å, W5-W4=2.11Å is possible. Moreover, the distance O6-W7=2.89 Å and W4-O1=3.01 allow the proton to transfer from O6 to O1 to form new Brønsted acid sites. This process is favoured by the high proton affinity of water trimers, as pointed out before, and by the easy and fast proton transfer between water molecules as demonstrated by numerous studies on the argument. However, the proton transfer of an acid site on O6 to the acid site on O1 is not sufficient to explain the population in the D3 site. Sonneman et al. (1993) demonstrated that there is a significant non-linear deviation between the actual concentration of, on one hand,

possible maximum concentration in Brønsted acid sites, and on the other hand, that this discrepancy increases when increasing the Al content. In a study on the D-heulandite dehydrated acid form, reported in chapter 8 of this PhD thesis, I demonstrated that this discrepancy depends not only on the Si/Al ratio but also on the presence of small amounts of water, even if not experimentally detectable, in acid materials. Therefore, this effect can be attributed to proton transfer from the Brønsted site to reabsorbed water molecules, forming either a hydroxonium ion  $(\text{H}_3\text{O})^+$  or charged clusters like  $(\text{H}_5\text{O}_2)^+$  or  $(\text{H}_7\text{O}_3)^+$ . In the previous section of this chapter, I reported that the amount of Brønsted sites found by Martucci et al (1999) in the dehydrated form are equal to 2.4 in comparison with a theoretical value of 3.8 given by the Al content per unit cell. As for D-heulandite, this discrepancy can be attributed to the proton transfer to reabsorbed water molecules forming charge clusters or hydroxonium ions. In rehydrated D-ferrierite where 3.56 hydroxyl groups were recognised, it is easy to hypothesise that a remarkable part of the deuterium atoms in the charged clusters transfer to the D3 hydroxyl group with framework oxygen O1.

For all tables: Estimated standard deviations in parentheses refer to the last digit.  
Site fractions are fixed to 1.0 for all framework atoms.

<b>Space Group</b>	<b><i>Immm</i></b>
<b>a (Å)</b>	18.979(2)
<b>b (Å)</b>	14.113(1)
<b>c (Å)</b>	7.445(7)
<b>V (Å<sup>3</sup>)</b>	1994.05(3)
<b>Refined pattern 2θ range (°)</b>	7.8 - 137
<b>R<sub>wp</sub>(%)</b>	38
<b>R<sub>p</sub>(%)</b>	26
<b>R<sup>2</sup><sub>F</sub>(%)</b>	10
<b>N<sub>obs</sub></b>	2604
<b>N<sub>var</sub></b>	49

Table 16: Lattice parameters and refinement details for zeolite ferrierite at 2K

	<b>x/a</b>	<b>y/b</b>	<b>z/c</b>	<b>Uiso</b>
<b>Si1</b>	0.1582(12)	0	0	0.023(5)
<b>Si2</b>	0.0822(5)	0.1974(11)	0	0.023(5)
<b>Si3</b>	0.2777(7)	0	0.2897(14)	0.023(5)
<b>Si4</b>	0.3259(3)	0.2046(6)	0.2026(13)	0.023(5)
<b>O1</b>	0	0.2337(24)	0	0.035(3)
<b>O2</b>	0.2544(16)	0	1/2	0.035(3)
<b>O3</b>	0.0972(11)	0.0831(11)	0	0.035(3)
<b>O4</b>	0.1995(10)	0	0.1945(21)	0.035(3)
<b>O5</b>	1/4	1/4	1/4	0.035(3)
<b>O6</b>	0.1442(11)	0.2854(16)	1/2	0.035(3)
<b>O7</b>	0.1111(6)	0.2545(10)	0.1761(16)	0.035(3)
<b>O8</b>	0.3194(6)	0.0906(6)	0.2055(18)	0.035(3)

Table 17a: Atomic coordinates and thermal parameters in framework atoms for zeolite ferrierite at 2K

	<b>x/a</b>	<b>y/b</b>	<b>z/c</b>	<b>Fraction</b>	<b>Uiso</b>
<b>w1</b>	0	0	0.270(17)	0.23(9)	0.076(70)
<b>w2</b>	0.0806(15)	0.0812(22)	1/2	0.44(6)	0.018(14)
<b>w3</b>	0.052(4)	0.144(6)	1/2	0.34(10)	0.035(34)
<b>w4</b>	0	0.433(3)	0.087(5)	0.55(6)	0.039(19)
<b>w5</b>	0	0.644(3)	0.334(6)	0.58(8)	0.04(11)
<b>w9</b>	0	1/2	1/2	0.11(34)	0.174(15)
<b>w7</b>	0	0.2249(25)	1/2	0.86(12)	0.008(35)
<b>w6</b>	0	0.394(5)	1/2	0.51(12)	0.048(36)
<b>D1</b>	0.174(4)	0	0.312(6)	0.18(5)	0.011(37)
<b>D2</b>	0.124(11)	0.220(7)	1/2	0.08(8)	0.03(15)
<b>D3</b>	0	0.3048(25)	0	0.38(12)	0.120(88)

Table 17b: Atomic coordinates, thermal parameters and site occupancies in extraframework atoms for zeolites ferrierite at 2K

<b>Si1-O3</b>			
<b>(x2)</b>	1.648(1)		
<b>Si1-O4</b>			
<b>(x2)</b>	1.647(1)		
<b>Si2-O1</b>	1.643(2)		
<b>Si2-O3</b>	1.638(2)		
<b>Si2-O7</b>			
<b>(x2)</b>	1.634(1)		
<b>Si3-O2</b>	1.627(1)		
<b>Si3-O4</b>	1.644(2)		
<b>Si3-O8</b>			
<b>(x2)</b>	1.630(1)		
<b>Si4-O5</b>	1.616(2)		
<b>Si4-O6</b>	1.618(1)		
<b>Si4-O7</b>	1.606(1)		
<b>Si4-O8</b>	1.613(2)		
<b>D1-O4</b>	1.0014(8)		
<b>D2-O6</b>	0.9982(9)		
<b>D3-O1</b>	1.0035(10)		
<b>T2-O1-</b>			
<b>T2</b>	143.6(5)		
<b>T3-O2-</b>			
<b>T3</b>	148.5(4)		
<b>T1-O3-</b>			
<b>T2</b>	145.3(3)		
<b>T1-O4-</b>			
<b>T3</b>	143.9(7)		
<b>T4-O5-</b>			
<b>T4</b>	180.0(0)		
<b>T4-O6-</b>			
<b>T4</b>	137.5(6)		
<b>T2-O7-</b>			
<b>T4</b>	151.5(1)		
<b>T3-O8-</b>			
<b>T4</b>	145.5(3)		

Table 18: Selected bond distances (Å) and angles (°) within the framework for zeolite ferrierite at 2K

### 8.1) HEULANDITE: STRUCTURAL AND CHEMICAL FEATURES

Heulandite-type zeolites are among the most abundant microporous aluminosilicates in nature. According to the Zeolite Subcommittee of the Commission on New Minerals and Mineral Names of the International Mineralogical Association (IMA) two minerals, heulandite and clinoptilolite, have the same topology [IZA code HEU].

Heulandite is defined as the zeolite mineral having an Si/Al ratio  $< 4.0$ , and clinoptilolite as having an Si/Al ratio  $\geq 4.0$ . A suffix indicates the chemical symbol of the most abundant extraframework element, e.g. heulandite-Na, heulandite-Ca, clinoptilolite-K etc. (Coombs *et al.*, 1998). Therefore the mineral used in this work is classified as heulandite-Ca.

Heulandite-type zeolites can be of a sedimentary or hydrothermal genesis. The genetic growth environment is important because the dominant part of heulandite-type material applied in technological application is of “sedimentary” origin. Historically the name “clinoptilolite” is associated to sedimentary materials and “heulandite” to materials of hydrothermal genesis. However the classification in hydrothermal and sedimentary heulandite-type materials does not match up with the classification in heulandite and clinoptilolite according to the IMA Commission’s criterion. Even if the Si/Al ratio is usually less than four in minerals of hydrothermal genesis and greater than four in materials crystallized in sedimentary environment, there are clinoptilolites of almost certain hydrothermal origin as well as “sedimentary” heulandites. It is interesting to note that if in addition to Si and Al the most common extraframework cations (Ca, Na, K, Mg, Sr, Ba) and H<sub>2</sub>O molecules are taken into account, discriminant analysis is able to correctly classify ca. 96% of heulandite-type minerals with regard to their genetic groups (Alberti and Brigatti, 1985).

The topological symmetry of heulandite-type minerals is  $C2/m$  with approximate unit cell parameters  $a = 17.7 \text{ \AA}$ ,  $b = 17.9 \text{ \AA}$ ,  $c = 7.4 \text{ \AA}$ ,  $\beta = 116^\circ$ . A two-dimensional channel arrangement parallel to (010) characterizes the HEU framework-type (Figure 60). Channels delimited by ten-membered ( $7.5 \times 3.1 \text{ \AA}$ ) and eight-membered ( $4.6 \times 3.6 \text{ \AA}$ ) tetrahedra rings run parallel to the  $c$ -axis. These channels are cross-linked by additional eight-membered ring channels which run parallel to  $[100]$  and  $[102]$ .

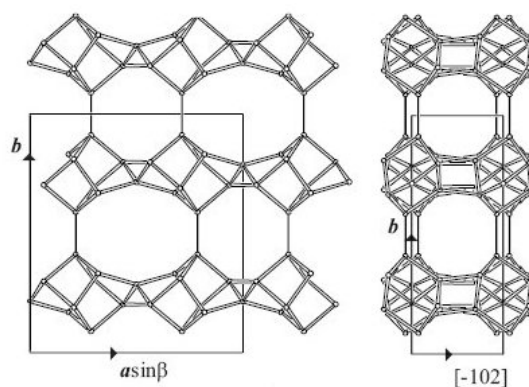


Figure 60: Unit cell content of zeolite heulandite projected along  $c$  (left) and along  $[102]$  (right).

There is still doubt about the true symmetry of heulandites and clinoptilolites.  $C2/m$  is the maximum symmetry, which may be lowered to  $C2$ ,  $Cm$ ,  $C-1$  and  $C1$ , due to different Si, Al preference on tetrahedral sites associated with specific locations of extraframework cations and  $H_2O$  molecules (Armbruster, 2001).

It is known that the behaviour of HEU structures when heated strongly varies as a function of the extraframework cations. In particular natural Ca-dominant (Alberti & Vezzalini, 1983; Khobaer *et al.*, 2008) and  $Cd^{2+}$ -exchanged heulandites (Doebelin & Armbruster, 2003) heated over  $250^\circ C$  transform into a new phase (usually called phase B) characterized by strong distortion of the framework and breaking of T-O-T bridges with the formation of new T-O-T connections which partially occlude the ten-membered ring channels. These T-O-T breakings do not occur in K-dominant heulandite (Galli *et al.*, 1983), in natural Na-, Ca-rich K-poor clinoptilolites (Armbruster & Gunter, 1991), and in natural Na-poor Ca-, Mg-, K-rich clinoptilolites (Armbruster, 1993). As a general rule, the prevailing presence of small divalent extraframework cations seems to allow breaking of T-O-T bridges whereas the HEU framework with monovalent extraframework cations preserves its topology upon heating. Therefore, it is highly probable that heating above  $250-300^\circ C$  causes the breaking of T-O-T bridges in our heulandite-Ca starting sample whereas this phase transformation does not occur in its Na-,  $NH_4$ -exchanged or acidic forms. This last assumption will be confirmed by a structure refinement of dehydrated acid heulandite also named D-heulandite.

## 8.2) EXPERIMENTAL

### 8.2.1) Materials

A sample of natural heulandite-Ca from Nasik, India,  $Ca_{0.9}K_{0.9}Ca_{3.5}Al_{8.62}Si_{27.51}O_{72} nH_2O$  (Sukheswala *et al.*, 1974) was pulverized. Ca and other minor extraframework ions were exchanged by  $Na^+$  by mixing and stirring the heulandite powder in 2 M NaCl solution. Exchange was first attempted for two weeks at ambient conditions. After this procedure did not yield completely Na-exchanged heulandite-Na, the powder and the exchange solution were placed in a Teflon-coated autoclave at 433 K for additional two weeks. Complete exchange (absence of Ca and K) was verified by using the energy dispersive system (EDS) of a scanning electron microscope. Heulandite-Na was then filled in a glass ampoule, dehydrated under vacuum ( $3 \times 10^{-3}$  mbar) for 24 hours at 580 K, and subsequently sealed.

Then, dehydrated heulandite-Na was undertaken in a glove-bag in an argon or nitrogen atmosphere. The sample was stirred for 3 weeks at  $25^\circ C$  in 2 M  $ND_4Cl$  solution ( $ND_4Cl$  with  $D_2O$ ). After periods of 10 days the exchange solution was replaced. Complete  $ND_4$ -exchange was verified by EDS analyses (absence of Na) with the scanning electron microscope. Subsequently, the sample was filtered and washed with  $D_2O$ .

Heulandite- $ND_4$  was refilled in a glass ampoule and heated under vacuum for 24 h at 770 K to

remove D<sub>2</sub>O and ND<sub>3</sub>. The glass ampoule was sealed under vacuum to avoid contact with air and humidity. Finally, the heat-treated heulandite sample was repacked in an argon-flushed glove-bag from the ampoule into a vanadium container sealed with a rubber gasket and 6 screws to ensure humidity-free transport to the neutron source.

### 8.2.2) Neutron data collection

Neutron powder patterns were collected at 2.25 K at the D2B line (ILL, Grenoble). Rietveld structure refinements were performed with the GSAS package (Larson & von Dreele, 1994). The cell volume (2072(1) Å<sup>3</sup>) is significantly smaller (2.5%) than that of the NH<sub>4</sub>-exchanged form (2126(1) Å<sup>3</sup>) and that of the untreated heulandite-Ca (2107.0(5) Å<sup>3</sup>) (Mortier and Pearce 1981, Yang and Armbruster, 1998). The main cause of the volume decrease of acid heulandite is related to decrease of the *b* parameter. Framework atoms of NH<sub>4</sub>-heulandite (Yang and Armbruster, 1998) provided the initial parameters of structure refinement. Extraframework atoms were localized by Fourier maps and refined by least-squares methods.

Two Brønsted acid sites were recognized. The position of each deuterium atom was initially restrained geometrically using an O-D distance of 1.00 Å, but these restraints were relaxed in the last cycles of refinement, and both the coordinates and occupancies of the deuterium atom were allowed to refine independently. Details of the refinement are given in Table 19, final atomic positions and occupancies in Table 20, bond distances and angles in Table 21. The final observed and calculated patterns are shown in Figure 61.

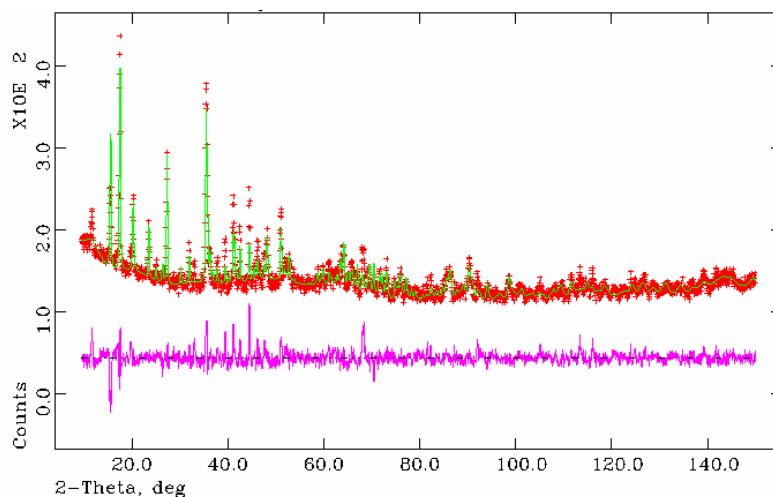


Figure 61: neutron diffraction final observed and calculated powder patterns for D-heulandite at 2K

### 8.3) RESULTS OF REFINEMENT AND DISCUSSION

From the structure refinement of the heulandite studied in this work, two Brønsted acid sites were recognized (see Table 20). The first one, D1, is on framework oxygen O1 pointing towards the center of the 8-membered ring channel running parallel to [102]; the second one, D2 is localized on the framework oxygen O6 pointing towards the 10-membered ring (see Figure 62). The deuterium sites have occupancies of 19 and 31 % for D1 and D2, respectively. The two Brønsted groups show quite regular site geometry.

The T2-O1-T2 angle, related to the D1 site, is narrow in the dehydrated acid phase, and significantly larger in NH<sub>4</sub>-exchanged heulandite (Yang & Armbruster, 1998) (135° and 153°, respectively; see Table 21). It is known that if a Brønsted proton forms an hydroxyl group the related T-O-T angle usually narrows (Sauer *et al.*, 1989), therefore, this result confirms that O1 becomes a Brønsted acid site. On the whole, about 3.2 acid sites were located in the unit cell, corresponding to only 37% of the measured aluminium content and the associated NH<sub>4</sub> content necessary for charge balance in the hydrated NH<sub>4</sub> phase. Thus the refined concentration of Brønsted acid sites is considerably lower than expected. Bankós *et al.* (1988), Crocker *et al.* (1993), Datka *et al.* (1995), Sawa *et al.* (1990) and Rodriguez-Gonzales *et al.* (2007) showed that for zeolites with high Al content the concentration of Brønsted sites is remarkably lower than predicted from the aluminium content. In particular, Sonnemans *et al.* (1993) demonstrated that there is a significant non-linear deviation between the actual concentration on one hand and the possible maximal concentration of Brønsted sites on the other hand. This discrepancy increases with increasing Al content. According to their results, the experimentally determined Brønsted sites for an Si/Al ratio as low as 3.1, as is the case of sample studied in this work, may not account for up to 70% of the theoretical value.

A number of reasons, such as incomplete NH<sub>4</sub><sup>+</sup> ion exchange, dehydroxylation and/or dealumination occurring during calcination, as well as residual NH<sub>4</sub><sup>+</sup> ions after calcination, have been put forward to explain the lower concentration of Brønsted acid sites (Sonnemans *et al.*, 1993)

Three additional extraframework sites (X1, X2 and X3 in Table 19) were recognized in D-heulandite, all at long distances from the framework. Some hypotheses can be suggested about their nature:

- a) The extraframework sites may represent residual Na cations due to incomplete NH<sub>4</sub><sup>+</sup> ion exchange. This hypothesis is highly improbable as a chemical (EDS) analysis was performed on the studied material after NH<sub>4</sub>-exchange. In addition, single crystals used to study the crystal structure of NH<sub>4</sub>-exchanged heulandite (Yang & Armbruster, 1998) indicated also complete cation exchange Na→NH<sub>4</sub>.
- b) The extraframework sites may represent residual ND<sub>4</sub>-groups after calcination. Difference Fourier synthesis does not show any indication of positive maxima at about 1 Å from these sites, attributable to D atoms of ND<sub>4</sub> groups or D<sub>2</sub>O molecules; this fact together with the long duration

(24 h under vacuum) and high temperature (770 K) excludes that there is residual D<sub>2</sub>O or ND<sub>4</sub> after calcination. As a result, the presence of a significant residue of ND<sub>4</sub> or D<sub>2</sub>O in the D-heulandite samples studied seems improbable and may be disregarded.

c) The extraframework sites may represent extraframework Al atoms caused by dealumination of the framework. Firstly, the procedure followed to obtain D-heulandite should avoid significant dealumination of the framework. Moreover, the Rietveld difference-Fourier synthesis does not show any maximum, which can be interpreted as oxygen atoms coordinated to hypothetical extraframework Al. As a consequence we may exclude dehydroxylation due to dealumination of the framework. We may also exclude dehydroxylation associated with a significant amount of three-coordinated framework aluminium as the structure refinement does not show any remarkable distortion of the tetrahedral framework. It should also be noted that only 3.2 Brønsted acid sites have been localized compared with 8.8 Al atoms given by the chemical analysis and such a high number of tetrahedral defects should be evidenced by the structure refinement.

d) The location of the extraframework site X1 is intermediate between that of fully occupied N3 found in NH<sub>4</sub>-exchanged heulandite (Yang & Armbruster, 1998) and that of H<sub>2</sub>O site (frequently called W1) found in natural and cation-exchanged heulandite-clinoptilolite minerals, which is usually the H<sub>2</sub>O site with highest occupancy. All three sites X1, W1, and N3 are six-fold coordinated and bonded to the same framework oxygens O2, O3 and O4 respectively (see Fig. 63). X2 and X3 sites positions do not resemble those of other extraframework sites found in other structures with HEU topology. It should also be noted that the use of nitrogen or oxygen scattering cross-sections for neutrons does not remarkably influence the occupancy of X1, X2, and X3 sites found in the diffraction experiment. The absence of maxima which can be attributed to deuterium atoms located near these sites supports the hypothesis that the additional extraframework sites may represent re-adsorbed H<sub>2</sub>O molecules. Our hypothesis is that when the ampoule was melted off after calcinations under vacuum or there was significant humidity when the sample was filled into the vanadium cylinder for neutron data collection. In such case X1, X2, and X3 represent about 40% of the H<sub>2</sub>O molecules found in the single-crystal structure refinement of hydrated NH<sub>4</sub>-exchanged heulandite (Yang & Armbruster, 1998). This fraction seems very high but we have to consider the strongly hydrophilic behaviour of the heulandite powder sample due to the low Si/Al ratio (3.1).

e) Once the presence of significant residual NH<sub>4</sub><sup>+</sup> ions or extraframework Al atoms is disregarded, another explanation must be found to justify the experimental evidence that the concentration of Brønsted sites is by far lower than the theoretical value given by the Al-content. On the other hand it is highly improbable that the high discrepancy between expected and analysed D sites is an artefact due to underestimation of the acid sites in our structure refinement. The ability of Brønsted acid sites to react with adsorbed H<sub>2</sub>O molecules to form hydroxonium ions, H<sub>3</sub>O<sup>+</sup>, has been studied by many authors by means of a variety of experimental techniques and computational methodologies. The formation of hydroxonium ions has been envisaged for many years (e.g. Barrer & Klinowski, 1975) but still today unambiguous evidence of their presence has not yet been adduced. Infrared spectra obtained for samples with a loading level of one H<sub>2</sub>O molecule per Brønsted site have been interpreted as due the formation of a hydroxonium ion (Marchese *et al.*, 1993) or a neutral hydrogen-

bonded complex (Wakabayashi *et al.*, 1996) or to the simultaneous presence of both species (Smith *et al.*, 1996; Parker *et al.*, 1993) or to the presence of  $\text{H}_5\text{O}_2^+$  or  $\text{H}_7\text{O}_3^+$  clusters (Jentys *et al.*, 1989). The effect of  $\text{H}_2\text{O}$  molecules adsorbed on bridging hydroxyl groups has also been studied by  $^1\text{H}$  MAS NMR measurements (Hunger *et al.*, 1991; Batamack *et al.*, 1993). Results indicate the simultaneous presence of hydroxonium ions and hydrogen-bonded  $\text{H}_2\text{O}$  up to a level of one  $\text{H}_2\text{O}$  molecule per Brønsted site. Moreover the shift of the  $^1\text{H}$  NMR of bridging OH groups can be interpreted by fast proton exchange between  $\text{H}_2\text{O}$  molecules, bridging OH groups and hydroxonium ions (Hunger *et al.*, 1991). In H-mordenite after water adsorption, the observed vibrational features in neutron inelastic scattering experiments are assigned to hydroxonium ions, hydrogen-bonded  $\text{H}_2\text{O}$ , and free hydroxyl groups. Stuckenschmidt *et al.* (1996) detected the presence of  $\text{H}_3\text{O}^+$  groups in calcined and rehydrated ammonium-natrolite by using single crystal X-ray diffraction data. Many computational studies have been performed in order to study the interaction of  $\text{H}_2\text{O}$  molecules with acid centres in H-zeolites. These calculations seem to indicate that with one  $\text{H}_2\text{O}$  molecule per acid site the structure is energetically stabilized, while the hydroxonium ions correspond to a transition state for proton exchange. At higher coverage (two or more molecules per acid site) protonated complexes are stabilized (Nusterer *et al.*, 1996; Zygmunt *et al.*, 1996; Jeanvoine *et al.*, 1998)). The calculated low proton affinity of  $\text{H}_2\text{O}$  ( $694 \text{ KJ mol}^{-1}$ ) and the by far larger proton affinity of  $\text{H}_2\text{O}$  dimers and trimers ( $806$  and  $853 \text{ KJ mol}^{-1}$ ), which can be compared with that of ammonia ( $858 \text{ KJ mol}^{-1}$ ) (Sauer, 2007), which always is protonated in any H-zeolite, is seen as an obstacle to the protonation of single  $\text{H}_2\text{O}$  molecules in H-zeolites but not to the protonation of  $\text{H}_2\text{O}$  dimers and trimers. In contrast, molecular dynamic simulations of  $\text{H}_2\text{O}$  molecules adsorbed in gmelinite (Benco *et al.*, 2000) and mordenite (Demuth *et al.*, 2001) indicate that even a single  $\text{H}_2\text{O}$  is sufficient to produce an hydroxonium ion.

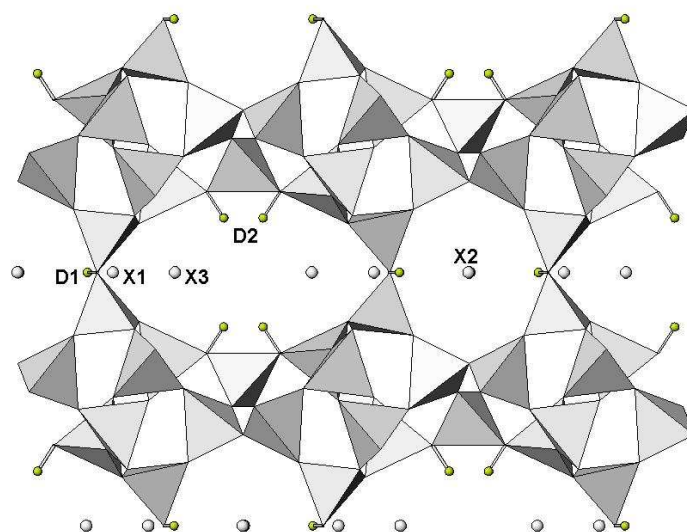


Figure 62: Location of Brønsted sites and extraframework sites in D-Heulandite at 2K

In conclusion, experimental results and computational studies provide convincing evidence for proton is transferred from the Brønsted site to reabsorbed  $\text{H}_2\text{O}$  molecule, forming either a

hydroxonium ion ( $\text{H}_3\text{O}^+$ ) or charge clusters like  $(\text{H}_5\text{O}_2)^+$  or  $(\text{H}_7\text{O}_3)^+$ . The latter interpretation is favoured by computational approaches (Kletnieks *et al.*, 2006).

As reported before, three potential  $\text{H}_2\text{O}$  sites, locating about 7.5 molecules per unit cell, were determined in D-heulandite; one of these (X2) is at coordination distance (see Table 21) only to framework oxygens. X1 and X3 are also coordinated by framework oxygens but are linked in a  $\text{H}_2\text{O}$  dimers with the distance  $\text{X1-X3} = 2.24 \text{ \AA}$  (Table 21 and Figure 63). This distance seems quite short for an Ow-Ow separation but the standard error is also large. Computational studies gave for an  $\text{H}_2\text{O-H-OH}_2$  cluster an ideal Ow-Ow distance around  $2.4 \text{ \AA}$ , where equal OH distances indicate formation of a protonated water dimer (Sauer, 2007).

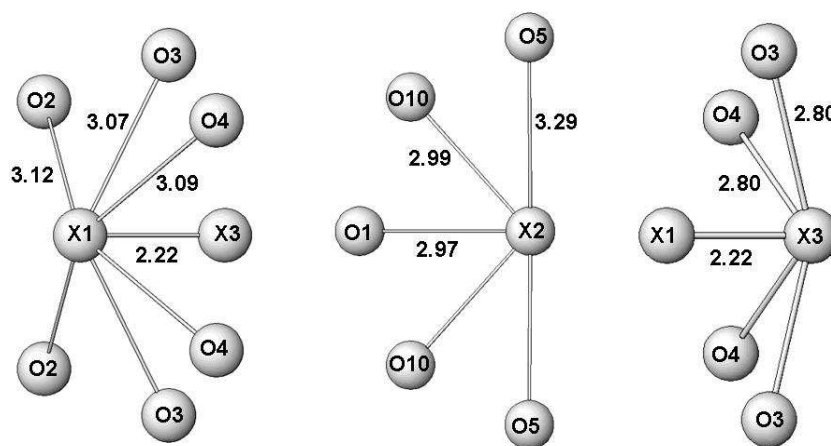


Figure 63: Coordination distances of the three extraframework sites in D-heulandite at 2K

Moreover, experimental finding by powder neutron diffraction indicates that the average oxygen-oxygen distance in a  $\text{DO}\cdots\text{D}\cdots\text{OD}$  dihydroxide anion in deuterated sodalite is as low as  $2.28 \text{ \AA}$  (Wiebcke *et al.*, 1992). Therefore, we assume that the discrepancy between the experimentally found Brønsted acid sites and their theoretical value (based on framework Al) is explained by the presence of hydroxonium ions or charged  $\text{H}_2\text{O}$  clusters.

However, Sonnemans *et al.* (1993) showed that there is a significant non-linear deviation between the concentration of Brønsted acid sites, determined by conductometric titration and infrared spectroscopy, and the theoretical concentration expected on the basis of the aluminium content. The lower the Si/Al ratio, the higher the discrepancy. These authors attributed this discrepancy to dealumination and dehydroxylation processes occurring during calcinations and proposed a model according to which the degree of these processes strongly depends on the concentration of paired Brønsted acid sites, which in turn is related to the concentration of vicinal tetrahedral aluminium sites in the zeolite framework.

A similar mechanism was invoked by Marosi (1980); dehydroxylation occurs in two steps: in the first step  $\text{H}_2\text{O}$  is eliminated from those hydroxyl groups which are coordinated to neighbouring framework aluminium atoms thus forming three-coordinated framework Al. The second step of dehydroxylation always involves migration of framework aluminium ions into the extraframework

pore system. With these interpretations dehydroxylation strongly depends on the Si/Al ratio. According to our hypothesis dehydroxylation is still related to the Al fraction in the tetrahedral framework but the mechanism of dehydroxylation is completely different. It is well known that the hydrophilicity or hydrophobicity of a zeolite depends by its Si/Al ratio. Usually the NH<sub>4</sub>-exchanged zeolite is heated to obtain its acid form and the sample is subsequently placed in the instrumental holder (vanadium container). During this operation the sample must have been partly rehydrated, even if the relocation was fast, scrupulous and performed under cover gas to reduce humidity. The amount of reabsorbed H<sub>2</sub>O is roughly a function not only of the time lapsed during refilling but also of the sample hydrophilicity, i.e. its Si/Al ratio.

In dehydrated H-SSZ-13 (CHA topology) (Smith et al., 1997) where the Si/Al ratio is 16, no detectable amount of H<sub>2</sub>O was evidenced, and the concentration of Brønsted acid sites corresponded to the theoretical value. The presence of a hydroxonium ion has been observed in the hydrated form of SSZ-13 through infrared spectroscopy. It is interesting to note that in H-SSZ-13 Brønsted sites were localized on the framework oxygens O1 and O2 whereas in H-SAPO-34 (CHA topology) (Smith et al., 1996) protonation was observed at oxygens O2 and O4. However, with low H<sub>2</sub>O loading in H-SAPO-34 the proton was removed from O4 to form a hydroxonium ion interacting with O1. In D-ERS-7 (IZA code ESV) (Campbell et al., 2001) the Si/Al ratio was 8.3, 65% of the theoretical concentration of acid sites was found and no other extraframework sites were reported. In synthetic ferrierite (Martucci et al., 1999) the Si/Al ratio was 8.5, 2.4 hydroxyl groups (63% of the amount assumed from Al atoms) and 1.9 H<sub>2</sub>O molecules were found in the unit cell. Three samples of mordenite (Martucci et al., 2000) with an Si/Al ratio of 5.5, 5.6 and 10.0 respectively were studied. 2.8, 2.4 and 2.4 H<sub>2</sub>O molecules and 3.2, 3.5 and 2.8 Brønsted sites (44%, 48% and 64% respectively of Al atoms) were localized in the unit cell. An interesting feature was found in D-Y zeolite (Czjzek et al., 1992). In the dehydrated sample (Si/Al = 2.43) three hydroxyl groups were found, accounting for about 90% of the (Al - Na) content. When the sample was slightly rehydrated (about 15 H<sub>2</sub>O molecules compared to 384 framework oxygens) the deuterons of one of the hydroxyl groups (accounting for about 40% of the deuterons found in the dehydrated sample) shifted in the direction of an H<sub>2</sub>O molecule up to a distance of 1.16 Å from the oxygen of the molecule while the distance to the framework oxygen increased up to 2.04 Å. The authors interpreted this shift as the jump of the deuterons to the H<sub>2</sub>O molecules with the formation of hydroxonium ions.

An interesting feature was found in D-Y zeolite (Czjzek *et al.*, 1992). In the dehydrated sample (Si/Al = 2.43) three hydroxyls groups were found, accounting for about 90% of the (Al - Na) content. When the sample was slightly rehydrated (about 15 H<sub>2</sub>O molecules compared to 384 framework oxygens) the deuterons of one of the hydroxyl groups (accounting for about 40% of the deuterons found in the dehydrated sample) shifted in the direction of an H<sub>2</sub>O molecule up to a distance of 1.16 Å from the oxygen of the molecule while the distance to the framework oxygen increased up to 2.04 Å. The authors interpreted this shift as the jump of the deuterons to the H<sub>2</sub>O molecules with the formation of hydroxonium ions.

Many authors have tackled the problem of the proton jump energy barrier by density functional theory (DFT) calculations. The calculated barriers for on-site proton jump vary within the range 60-100 KJ mol<sup>-1</sup> for CHA, FAU and MFI structures (Fermann *et al.*, 2000; Tuma & Sauer, 2004), whereas the proton jump barriers experimentally determined by <sup>1</sup>H NMR technique are significantly lower than the calculate ones (around 15-25 KJ mol<sup>-1</sup>) (Baba *et al.*, 1998; Tuma & Sauer, 2004). This discrepancy has been explained by the presence of undetected H<sub>2</sub>O in the sample (Ryder *et al.*, 2000).

It is therefore evident that the presence of H<sub>2</sub>O favours the proton transfer from the Brønsted acid sites to H<sub>2</sub>O molecules, thus supporting the hypothesis proposed in this work for interpretation of the discrepancy between experimentally determined and theoretical hydroxyl groups in acid zeolites.

Space Group	<b>C 2/m</b>
<b>a</b> (Å)	17.662(2)
<b>b</b> (Å)	17.713(2)
<b>c</b> (Å)	7.416(1)
<b>b</b> (°)	116.7(1)
<b>V</b> (Å) <sup>3</sup>	2072.3(5)
<b>Refined pattern min/max 2θ</b> (°)	10-120
<b>R<sub>wp</sub></b> (%)	4.38
<b>R<sub>p</sub></b> (%)	3.43
<b>R<sub>F</sub><sup>2</sup></b> (%)	8.05
<b>N<sub>obs</sub></b>	2810
<b>N<sub>var</sub></b>	105

Table 19: Lattice parameters and refinement details on D-heulandite at 2K  
Notes: Synchrotron radiation,  $\lambda=2.39845(1)$  Å

	<b>x/a</b>	<b>y/b</b>	<b>z/c</b>	<b>Fraction</b>	<b>Uiso</b>
<b>T1</b>	0.1813(8)	0.3336(8)	0.0982(8)	0.860(0)	0.002(1)
<b>T2</b>	0.2861(7)	0.4153(7)	0.4902(7)	0.520(0)	0.002(1)
<b>T3</b>	0.2845(7)	0.1850(7)	0.2785(7)	0.810(0)	0.002(1)
<b>T4</b>	0.4295(5)	0.2975(5)	0.5748(5)	0.890(0)	0.002(1)
<b>T5</b>	0	0,2891(9)	0	0.660(0)	0.002(1)
<b>O1</b>	0.3236(3)	0.05	0.556(7)	1.000(0)	0.004(1)
<b>O2</b>	0.2591(2)	0.1119(13)	0.372(4)	1.000(0)	0.004(1)
<b>O3</b>	0.3050(2)	0.1512(6)	0.1013(3)	1.000(0)	0.004(1)
<b>O4</b>	0.2308(2)	0.4029(12)	0.2485(1)	1.000(0)	0.004(1)
<b>O5</b>	0.05	0.3202(18)	0.05	1.000(0)	0.004(1)
<b>O6</b>	0.0805(8)	0.3416(10)	0.032(5)	1.000(0)	0.004(1)
<b>O7</b>	0.3667(2)	0.2298(14)	0.444(5)	1.000(0)	0.004(1)
<b>O8</b>	0.0248(2)	0.2355(16)	0.1964(2)	1.000(0)	0.004(1)
<b>O9</b>	0.2104(9)	0.2465(8)	0.160(4)	1.000(0)	0.004(1)
<b>O10</b>	0.3769(6)	0.3756(4)	0.545(6)	1.000(0)	0.004(1)
<b>X1</b>	0.2099(34)	0	0.011(8)	0.989(5)	0.034(2)
<b>X2</b>	0.001(10)	0	0.612(19)	0.500(5)	0.092(2)
<b>X3</b>	0.154(8)	0.05	0.918(17)	0.550(5)	0.101(2)
<b>D1</b>	0.156(2)	0	0.55(4)	0.191(5)	0.019(3)
<b>D2</b>	0.042(5)	0.396(5)	0.017(18)	0.307(3)	0.008(3)

Table 20: Atomic coordinates and thermal parameters of framework atoms for D-heulandite at 2K

<b>T1-O3</b>	1.625(1)	<b>T2-O1</b>	1.624(1)	<b>T3-O2</b>	1.624(1)
<b>T1-O4</b>	1.624(1)	<b>T2-O2</b>	1.627(1)	<b>T3-O3</b>	1.626(1)
<b>T1-O6</b>	1.626(1)	<b>T2-O4</b>	1.625(1)	<b>T3-O7</b>	1.625(1)
<b>T1-O9</b>	1.626(1)	<b>T2-O10</b>	1.627(1)	<b>T3-O9</b>	1.624(1)
<b>T4-O5</b>	1.625(1)	<b>T5-O6 [x2]</b>	1.625(1)	<b>D2-O6</b>	1.16(8)
<b>T4-O7</b>	1.626(1)	<b>T5-O8 [x2]</b>	1.625(1)	<b>D1-O1</b>	1.00(3)
<b>T4-O8</b>	1.625(1)				
<b>T4-O10</b>	1.625(1)				
<b>X1-O2 [x2]</b>	3.12(5)	<b>X2-O1</b>	2.97(2)	<b>X3-O3 [x2]</b>	2.79(3)
<b>X1-O3 [x2]</b>	3.07(3)	<b>X2-O5 [x2]</b>	3.29(4)	<b>X3-O4 [x2]</b>	2.80(9)
<b>X1-O4 [x2]</b>	3.09(5)	<b>X2-O10 [x2]</b>	2.99(1)	<b>X3-X1</b>	2.21(2)
<b>X1-X3</b>	2.22(2)	<b>X2-X2</b>	1.65(4)		
<b>X1-D1</b>	3.11(4)				
<b>T2-O1-T2</b>	135.0(2)	<b>T1-O6-T5</b>	139.6(2)		
<b>T2-O2-T3</b>	144.3(2)	<b>T3-O7-T4</b>	161.6(4)		
<b>T1-O3-T3</b>	148.5(3)	<b>T4-O8-T5</b>	162.4(2)		
<b>T1-O4-T2</b>	136.9(1)	<b>T1-O9-T3</b>	149.9(9)		
<b>T4-O5-T4</b>	151.3(2)	<b>T2-O10-T4</b>	147.3(2)		

Table 21: Selected bond distances ( $\text{\AA}$ ) and angles ( $^\circ$ ) within the framework of D-heulandite at 2K

For all tables: Estimated standard deviations in parentheses refer to the last digit.  
Site fractions are fixed to 1.0 for all framework atoms.

## CONCLUSIONS

The aim of this work was to characterise zeolitic catalysts in non-ambient conditions starting from structure analysis of diffraction data collected on powder or single crystals, using X-ray (conventional source or synchrotron radiation) or neutron diffraction. The main results can be summarised as follows:

- 1) zeolite tschernichite. The stepwise dehydration process in both monoclinic and tetragonal polytypes of tschernichite, monitored by the breaking-up of powder patterns as a function of temperature, put in evidence some important differences in the behaviour of the two polytypes. The amorphisation process begins at about 250°C in the tetragonal polytype and at about 450°C in the monoclinic type. A careful check of the experimental profiles for the two samples clearly indicated that there are remarkable differences in region 13-10 Å. It is easy to attribute these differences to different fractions of polytypes in the two samples. The results of Rietveld refinements indicate the presence of a very high fraction of monoclinic polytype in sample A (comparable with that in the tetragonal one) which generates frequent staking vectors where polytypes A and B meet, thus favouring an instability in the framework at lower temperatures. On the contrary in sample B, where only one polytype (the monoclinic one) is preponderant, staking vectors and linear defects are less frequent, favouring stability at higher temperatures.
- 2) zeolite omega. The high quality of the XRPD data collected during the in situ time resolved heating process allowed a careful investigation of the structural changes to occur during template decomposition and ammonium ions calcination. Although the symmetry of the structure was not altered by the activation process, permanent and transient structural modifications of the framework have been evidenced. The deformation of the gmelinite cage is related to a shift in the O2 framework oxygen towards the centre of cavity. The experimental results suggest that this shift is guided by the presence of an O2-H Brønsted acid site, as a result of the presence of protons, residual to TMA Hoffmann degradation. At the same time, the star-shaped deformation in the 12-ring channel indicates the presence of a proton bonded on an O5 framework oxygen which compensates the charge imbalance due to the removal of ammonium ions.
- 3) zeolite gmelinite. The thermal behaviour of sodium-gmelinite is characterised by a series of unique or peculiar features. The mineral is fully dehydrated at a temperature as low as 90°C and is only stable up to 280°C; as a consequence of water loss, one cation site is only bonded to three frameworks, thus representing the first finding of a threefold coordination for sodium in silicates. At 100 K extraframework cations and water molecules are spread over a number of sites with low occupancy; at room temperature these ions gather in a few positions with high occupancy. Above 280°C gmelinite transforms, through a 'face sharing tetrahedra' process, into an AFI-type material characterised by strong disorder in the framework. This disorder causes an anomalous and unusual X-ray diffuse scattering in the reciprocal planes  $hkl$  with  $l$  odd. The transition from gmelinite to AFI-type phase occurs

through an intermediate, 'transient' phase, which exists in the temperature range 300-370°C, and rapidly transforms into the AFI-type phase.

- 4) ferrierite. Neutron Rietveld structure refinement of ferrierite in its deuterium rehydrated form enabled us to accurately determine the location and occupancy of the water molecule oxygen sites. Eight extraframework sites were found, all with partial occupancy and at large distances from the framework oxygens, which were attributed to reabsorbed H<sub>2</sub>O molecules. On the whole, 3.56 hydroxyl groups were recognised, as compared with the 3.8 Al atoms in the unit cell. The presence of a new acid site, D3, which faces towards the centre of the 10-ring parallel to [001], and bonded to the O1 framework oxygens, suggests an interesting mechanism of proton transfer inside microporous channels in this zeolite.
- 5) zeolite heulandite. Neutron Rietveld refinement of a natural heulandite in its deuterium form allowed us to identify two Brønsted acid sites. One was on framework oxygen O1, occupied to 20% and facing toward the centre of the 8-ring channel running parallel to [102]; the other was on O6, occupied to 30% and facing toward the 10-ring channel running parallel to the *c* axis. Three other extraframework sites, located around a distance of 3 Å from the framework oxygens, were attributed to reabsorbed H<sub>2</sub>O molecules. On the whole, about 3.2 Brønsted acid sites were located representing about 37% of the value expected on the basis of the aluminium content. This discrepancy is attributed to a proton transfer from the Brønsted site to reabsorbed H<sub>2</sub>O molecules, forming either a hydroxonium ion (H<sub>3</sub>O<sup>+</sup>) or charged clusters such as (H<sub>5</sub>O<sub>2</sub>)<sup>+</sup> or (H<sub>7</sub>O<sub>3</sub>)<sup>+</sup>.

## REFERENCES

- R. Aiello, R.M. Barrer, *J. Chem. Soc. A* (1970) 1470.
- A. Alberti, *Stud. Surf. Sci. Catal.* 60 (1990) 107.
- A. Alberti, in: T. Inui, S. Namba, T. Tatsumi (Eds.), *Chemistry of Microporous Crystals*, Kodansha, Tokyo (1991) 107.
- A. Alberti, M.F. Brigatti, *Amer. Mineral.* 70 (1985) 805.
- A. Alberti, G. Cruciani, M. C. Dalconi, A. Martucci, S. Caruso. *Studies in Surface Science and Catalysis*, 140 (2001) 13.
- A. Alberti, G. Cruciani, E. Galli, R. Millini, S. Zanardi, *J. Phys. Chem. C* 111 (2007) 4503.
- A. Alberti, G. Cruciani, E. Galli, S. Merlino, R. Millini, S. Quartieri, G. Vezzalini, S. Zanardi, *J. Phys. Chem. B* 106 (2002) 10277.
- A. Alberti, G. Cruciani, E. Galli, G. Vezzalini, *Zeolites* 17 (1996) 457.
- A. Alberti, P. Davoli, G. Vezzalini, *Zeitschrift fuer Kristallographie, Kristallgeometrie, Kristallphysik, Kristallchemie* 175 (1986) 249.
- A. Alberti, G. Gottardi, *Zeitschrift für Kristallographie*, 184 (1988) 49.
- A. Alberti, C. Sabelli, *Z. Kristallogr.* 178 (1987) 249.
- A. Alberti, G. Vezzalini, *TMPM Tschermaks Min. Petr. Mitt.* 31 (1983) 259.
- A. Alberti, G. Vezzalini, *Proc. 6th Int. Zeolite Conf.*, Reno (Olson D., Bisio A, eds.), Butterworths, UK, (1984) 834.
- A. Alberti, G. Vezzalini, *TMPM Tschermaks Min. Petr. Mitt.*, 31 (1983) 259.
- A. Alberti, G. Vezzalini, *Bull. Mineral.* 104 (1981) 5.
- A. Alberti, G. Vezzalini, E. Galli, S. Quartieri, *European Journal of Mineralogy* 8 (1996) 69.
- A. Alberti, M. Sacerdoti, S. Quartieri, G. Vezzalini, *Phys. Chem. Minerals* 26 (1999) 181
- T. Armbruster, *Amer. Mineral.* 78 (1993) 260.
- T. Armbruster, A. Galarnau, F. Di Renzo, F. Faujula, J. Vadrine (Eds.), *Zeolites and Mesoporous Materials at the Dawn of the 21<sup>st</sup> Century*, Elsevier, Amsterdam, (2001) 13.
- T. Armbruster, M.E. Gunter, *Amer. Mineral.* 76 (1991) 1872.
- R. Arletti, E. Galli, G. Vezzalini, W.S. Wise, *American Mineralogist* 90 (2005) 1186.
- R. Arletti, E. Mazzucato, G. Vezzalini, *Am. Mineral.* 91 (2006) 628
- T. Baba, N. Komatsu, Y. Ono, H. Sagisawa, *J. Phys. Chem. B* 102 (1998) 804.
- L. Baltusis, J.S. Frye, G.E. Maciel, *J. Am. Chem. Soc.* 108 (1986) 7119.
- L. Baltusis, J.S. Frye, G.E. Maciel, *J. Am. Chem. Soc.* 109 (1987) 40.
- Bankós, J. Valyon, G.I. Kapustin, D. Kalló, A.L. Klyachko, T.R. Brueva, *Zeolites* 8 (1988) 189.
- R.M. Barrer, *Jour. Chem. Soc. London* (1948) 2158.
- R.M. Barrer, *R. Jour. Chem. Soc. London*, (1958) 99.
- R.M. Barrer, H. Villiger, *Chem. Commun.* (1969) 659.
- R. M. Barrer, J.J. Klinowski, *Chem. Soc., Faraday Trans. 1*, 71 (1975) 690.
- R.M. Barrer, London Academic Press (1982).
- M.R. Basila, T.R. Kantner, K.H. Rhee, *J. Phys. Chem.* 68 (1964) 3197.
- P. Batamack, C. Dorémieux-Morin, J. Fraissard, D. Freude *J. Phys. Chem.*, 95 (1991) 3790.
- P. Batamack, C. Dorémieux-Morin, R. Vincent, J. Fraissard, *J. Phys. Chem.* 97 (1993) 9779.
- W.H. Baur, *J. Solid State Chem.* 97 (1992) 243.
- W.H. Baur, R.X. Fisher, R.D. Shannon, R.H. Staley, A.J. Vega, L. Abrams, D.R. Corbin, J.D. Jorgensen, *Z. Kristallogr.* 179 (1987) 281.
- G. Bellussi, G. Pazzuconi, C. Perego, G. Girotti, G. Terzoni, *J. Catal.* 157 (1995) 227.
- L. Benco, Th. Demuth, L. Hafner., F. Hutschka, *Chem. Phys. Letters* 324 (2000) 373.
- J.M. Bennett, J.P. Cohen, E.M. Flanigen, J.J. Pluth and J.V. Smith, *ACS Symp. Ser.* 228 (1983) 109.
- R. Bialek, W.M. Meier, M. Davis, M.J. Annen, *Zeolites* 11 (1991) 438-442
- D.L. Bish J.W. Carey, *Min. Soc. Am. Rev. in Min.* 45 (2001), 403.
- R.C. Boggs, D.G. Howard, J.V. Smith, G.L. Klein, *Amer. Mineral.* 78 (1993) 822.
- L. Boretto, M.A. Cambor, A. Corma; Perez-Pariente, *J. Appl. Catal.* 82 (1992) 37.

- V. Bosacek, S. Beran, Z. Jirak, *J. Phys. Chem.* 85 (1981) 367.
- E. Bowes, J.J. Wise, US Patent 3, 578 (1971) 728.
- D.W. Breck, *Zeolite Molecular Sieves*, Wiley, New York (1974).
- W.A. Buckermann, C.B. Huong, F. Fajula, C. Gueguen, *Zeolites* 13 (1993) 448.
- L.M. Bull, A.K. Cheetham, P.D. Hopkins, B.M. Powell. *J. Chem. Soc., Chem. Commun.* (1993) 1196.
- B.J. Campbell, A.K. Cheetham, T. Vogt, L. Carluccio, W.O.Jr. Parker, C. Flego, R. Millini, *J. Phys. Chem. B* 105 (2001) 1947.
- T.R. Cannan, G.L. Wamer WO, Patent 87 (1987) 00158.
- E. Cannillo, A. Coda, G. Fagnani, *Acta Cryst.* 20 (1966) 301
- G. Cao, L.R.M. Luc, J.L. White, T.-J Chen, M.J. Shah, US Patent 6080303 (1998)
- J.F. Carpency, T.-J Chen, S.C. Fung, A. Brennek, US Patent 6090271 (1997)
- J. Ciric, US Appl. 509 (1965) 568.
- J. Ciric, *British Pat.* 1, 117 (1968) 568.
- J. Ciric, L.J. Ried, US Pat. 3, 433 (1969) 589.
- J.F. Cole, H.W. Kouwenhoven, in: W.M. Meier, J.B. Uytterhoeven (Eds.), *Molecular Sieves*, ACS Symposium, vol. 121, American Chemical Society, Washington DC, 1973, p. 583.
- D.S. Coombs, A. Alberti, T. Armbruster, G. Artioli, C. Colella, E. Galli, J.D. Grice, F. Liebau, J.A. Mandarino, H. Minato, E.H. Nickel, E. Passaglia, D.R. Peacor, S. Quarieri, R. Rinaldi, M. Ross, R.A. Sheppard, E. Tillmanns, G. Vezzalini, Recommended nomenclature for zeolite minerals. *Eur. J. Mineral.* 10 (1998) 1037.
- D.S. Coombs, A. Alberti, T. Armbruster, G. Artioli, C. Colella, E. Galli, J.D. Grice, F. Liebau, J.A. Mandarino, H. Minato, E.H. Nickel, E. Passaglia, D.R. Peacor, S. Quarieri, R. Rinaldi, M. Ross, R.A. Sheppard, E. Tillmanns, G. Vezzalini, *Canadian Mineralogist*, 35 (1997) 1571.
- D.E. Cox, Academic Press, London, U.K. (1992) 186
- M. Crocker, R.H.M. Herold, M.H.W. Sonnemans, C.A. Emels, A.E. Wilson, J.N. van der Moolen, *J. Phys. Chem.* 97 (1993) 432.
- F. Cronsted, *Akad. Handl.*, 17 (1756) 20.
- G. Cruciani, A. Martucci, C. Meneghini, *European Journal of Mineralogy* 15 (2003) 257.
- G. Cruciani, A. Alberti, A. Martucci, K.D. Knudsen, P. Ciambelli, M. Rapacciuolo, Proceedings 12th International Zeolite Conference, Baltimore, MD, 5–10 July (1998)
- G. Cruciani, G. Artioli, A. Gualtieri, K. Stahl, J.C. Hanson, *Am. Mineral.* 82 (1997) 729–739.
- M. Czjzek, H. Jovic, A.N. Fitch, T. Vogt, *J. Phys. Chem.* 96 (1992) 1535.
- R.H. Daniels, G. T. Ken, L.D. Rollmann, *J. Am. Chem. Soc.* 100 (1978) 3097.
- J. Das, Y.S. Bath, A.B. Halgeri, *Catal. Lett.* 23 (1994) 161.
- J. Datka, B. Gil, A. Kubacka, *Zeolites* 15 (1995) 501.
- W.H. Dawson, S.W. Kaiser, P.D. Ellis, R.R. Inners, *J. Am. Chem. Soc.* 103 (1981) 6780.
- K.P. De Jong, C.M.A.M. Mesters, D.R.G. Peferoen, P.T.M. van Brugge, C. de Groot, *Chem. Eng. Sci.* 51 (1996) 2053.
- Th. Demuth, L. Benco, L. Hafner., H. Toulhoat, *Int. J. Quantum Chemistry* 84 (2001) 110.
- F. Di Renzo, F. Fajula, F. Figueras, T. Des Courieres, US Pat. 5, 165 (1992) 906.
- N. Doebelin, T. Armbruster, *Micr. Mes. Mat.* 61 (2003) 85.
- P.E. Jr. Eberly, *J. Phys. Chem.* 72 (1968) 1042.
- J. Elsen, G.S.D. King, W.J. Mortier, *Journal of Physical Chemistry* 91 (1987) 5800.
- S. Esposito, C. Ferone, M. Pansini, L. Bonaccorsi, E. Proverbio, *J. Eur. Ceram. Soc.* 24. (2004) 2689.
- F. Fajula, R. Ibarra, F. Figueras, C. Gueguen, *J. Catal.* 89 (1984) 64.
- J.T. Fermann, C. Blanco, S. Auerbach, *J. Chem. Phys.* 112 (2000) 6779.
- Z.R. Finelli, C.A. Querini, R.A. Comelli, *Catal. Lett.* 78 (2002) 339.
- R.X. Fischer, W.H. Baur, R.D. Shannon, R.H. Staley, L. Abrams, A.J. Vega, J.D. Jorgensen *Acta Cryst.* 179 (1987) 281
- R.X. Fisher, W.H. Baur, R.D. Shannon, R.H. Staley, L. Abrams, A.J. Vega, J.D. Jorgensen, *Acta Crystallogr. B* 44 (1988) 321.
- K. Fisher, *N. Jb. Miner. Mh.* (1966) 1.
- E.M. Flanigen, E.R. Kellberg, US Appl. 569 (1966) 805.
- E.M. Flanigen, E.R. Kellberg, *Dutch Pat.* 6, 710 (1967) 729.

- E.M. Flanigen, E.R. Kellberg, US Pat. 4, 241 (1980) 036.
- C. Flego, R. Millini, J. Phys. Chem. B 105 (2001) 1947.
- E. Fois, A. Gamba J. Phys. Chem. B 103 (1999) 1794-1799.
- G. M. Fraase Storm, F. Tuinstra J. Appl. Cryst. 19 (1986) 372.
- G. Friedel Compt. Rend., 122 (1896,) 948.
- W. Friedrich Phys. Z. 14 (1913) 317
- C.A. Fyfe, G.C. Gobbi, G.J. Kennedy, J.D. Graham, R.S. Ozubko, W.J. Murphy, A. Bothner-By, J. Dadok, A.S. Chesnick, Zeolites 5 (1985) 179.
- E. Galli, Soc. It. Miner. Petr., Rendiconti XXXI 2 (1975) 599.
- E. Galli, Cryst. Struct. Commun. 3 (1974) 339.
- E. Galli, G. Gottardi, H. Mayer, A. Preisinger, E. Passaglia, Acta Cryst. B39 (1983) 189.
- E. Galli, E. Passaglia, D. Pongiluppi, R. Rinaldi, Contr. Mineral. Petrol. 45 (1974) 99.
- E. Galli, E. Passaglia, P.F. Zanazzi, N. Jb. Mineral., Mh., (1982) 145.
- E. Galli, S. Quartieri, G. Vezzalini, A. Alberti, European Journal of Mineralogy 7 (1995), 1029.
- A.M. Goossens, E.J.P. Feijen, G. Verhoeven, B.H. Wouthers, P.J. Grobet, P.A. Jacobs, J.A. Martens, Micropor. Mesopor. Mater. 35-36 (2000) 555.
- G. Gottardi, E. Galli, Natural Zeolites. Springer: Berlin. (1985) 409.
- R. Gramlich-Meier, W.M. Meier, B.K Smith, Z. Kristallogr. 169 (1984) 201.
- R. Gramlich-Meier, V. Gramlich, W.M. Meier, Am. Mineral. 70 (1985) 619.
- Guo Zhenya; Guo Chenghua; Jin Qinghua; Li Baohui; Ding Datong, Journal of Porous Materials (2005) 12, 29-33
- F. Haase, J. Sauer J. Phys. Chem. 98 (1994), 3083.
- B.S. Hemingway, R.A. Robie, Am. Mineral., 69 (1984) 307.
- J.B. Higgins, R.B. LaPierre, J.L. Schlenker, A.C. Rohrman, J.D. Wood, G.T. Kerr, W.J. Rohrbach, Zeolites 8 (1988) 446.
- A.J. Hoefnagel, H. van Bekkum, Appl. Catal. A 97 (1993), 87.
- T.R. Hughes, H.M. White, J. Phys. Chem. 71 (1967) 2192.
- M. Hunger, D. Freude, H. Pfeifer, J. Chem. Soc., Faraday Trans. 87 (1991) 657.
- Q. Huo, N.A. Stephenson, Patent EP1216959 (2002).
- T. Ikeda, K. Miyazawa, F. Izumi, Q. Huang, A. Santoro, Journal of Physics and Chemistry of Solids 60 (1999) 1531.
- M.S. Islam, R.A. Davies, J.D. Gale J. Chem. Soc., Chem. Commun. (2001) 661.
- P.B. Jamieson, L.S. Dent-Glasser, Acta Crystallogr. 20 (1966) 688.
- Y. Jeanvoine, J.G. Ángyán, G. Kresse, J. Hafner, J. Phys. Chem. B 102 (1998) 7307.
  - Jentys, G, Warecka, M. Derewinski, J.A. Lercher, J. Phys. Chem. 93 (1989) 4837.
- Z. Jirak, S. Vratislav, V. Bosacek, Phys. Chem. Solids 41 (1980) 1089.
- H. Jobic, M. Czjzek, R.A. van Santen J. Phys. Chem., 96 (1992)1540.
- H. Jobic, A. Tuel, M. Krossner, J. Sauer, J. Phys. Chem., 100 (1996) 19545.
- J.B. Jones, Acta Crystallogr. B24 (1968) 355.
- R.H Jones, P. Lightfoot, R.M. Ormerod, J. Chem. Soc., Chem. Commun. (1995) 783.
- H.B. Keene; Nature (London) 91 (1913) 607.
- T.M. Khabaer, T. Kuribayashi, K. Komatsu, Y. Kudoh, J. Mineral. Petrolog. Sciences 103 (2008) 61.
- G.J. Klap, H. van Koningsveld, H. Graafsma, A.M.M. Schreurs, Microporous and Mesoporous Materials 38 (2000) 403.
- P.W. Kletnieks, J.O. Ehresmann, J.B. Nicholas, J.F. Haw, Chem. Phys. Chem. 7 (2006) 114.
- J. Klinowski, M.W. Anderson, J.M. Thomas, J. Chem. Soc., Chem. Commun. (1983) 515.
- J. Klinowski, M.W. Anderson, J. Chem. Soc., Faraday Trans. 1 (1986) 569.
- H.P. Klug, L.E. Alexander, Wiley Interscience, New York, N.Y. (1974)
- T. J. G.Kofke, T.J. Gorte, G.T. Kokotailo, W.E. Farneth, J. Catal. 115 (1989) 265.
- H.W. Kouwenhoven, E.A. Gunnewegh, H. van Bekkum, Tagungsbericht 9601 (1996) 9.
- K. Koyama, Y. Takeuchi, Zeits. Krist. 145 (1977) 216.
- G.H. Kühn, J.N. Miale, Natural Zeolites: Occurrence, Properties, Use, Pergamon, (1978) 421
- Kuperman, S. Nadimi, S. Oliver, G.A. Ozin, J.M. Garces, M.M. Olken, Nature 365 (1993) 239.
- C. Lamberti. Micropor. Mesopor. Mater. 30 (1999), 155.

- A.C. Larson, R.B. von Dreele, Report LAUR (1994) 86.
- J.K. Lee, H.K. Rhee, *Catal Today* 38 (1997) 235.
- J.E. Lewis, C.C. Freyhardt, M.E. Davis, *J. Phys. Chem.* (1996) 5039.
- S.H.C. Liang, I.D.J. Gay, *J. Catal.* 66 (1980) 294.
- W. Loewenstein *Am Mineral* 39 (1954) 92.
- J.H. Lunsford, W.P. Rothwell, W. Shen, *J. Am. Chem. Soc.* 107 (1985) 1540.
- D. Luppi, Carbonin S. Boscardin M. Pegoraro S., *Rivista Mineralogica Italiana* 31 (2007) 8.
- G.E. Maciel, P.D. Ellis, *NMR Techniques in Catalysis*; Bell, A. T., Pines, A., Eds.; Marcel Dekker: New York, 1994; Vol. 55, pp 231-309.
- Yu. A. Malinovskii, *Sov. Phys. Crystallogr.* 1984, 29, 256
- L. Marchese, J. Chen, P.A. Wright, J.M. Thomas, *J. Phys. Chem.* 97 (1993) 8109.
- L. Marosi, *Angew. Chem. Int. Ed. Engl.* 19 (1980) 743.
- A. Martucci, A. Alberti, G. Cruciani, P. Radaelli, P. Ciambelli, M. Rapacciuolo, *Micr. Mes. Mat.* 30 (1999) 95.
- A. Martucci, A. Alberti, M.L. Guzman-Castillo, F. Di Renzo, F. Fajula, *Microp. Mesop. Mater.* 63 (2003) 33.
- A. Martucci, G. Cruciani, A. Alberti, C. Ritter, P. Ciambelli, M. Rapacciuolo, *Micr. Mes. Mat.* 35-36 (2000) 405.
- A. Martucci M. De Lourdes Guzman-Castillo, F. Di Renzo, F. Fajula, A. Alberti, *Micron. Mesop. Mat.* 104 (2007) 257.
- P. Massiani, F. Fajula, F. Di Renzo, *J. Chem. Soc., Chem. Commun.* (1988) 814.
- P. Massiani, F. Fajula, F. Figueras, J. Sanz, *Zeolites* 8 (1988) 332.
- P.D. Majors, T.E. Raidy, P.D. Ellis, *J. Am. Chem. Soc.* 108 (1986) 8123.
- H.D. Megaw, *Acta Crystallogr.* 5 (1952) 477.
- W.M. Meier, D.H. Olson, *Atlas of Zeolite Structure Types*: 3rd edition. Butterworth-Heinemann: London (1992).
- W.M. Meier, D.H. Olson, Ch. Baerlocher, *Atlas of Zeolite Structure Types* (1996). 4th Ed., Elsevier
- W.M. Meier, *Molecular sieves*, Society of Chemical Industry, London (1968) 10.
- H.H. Mooiweer, J. Suurd, K.P. de Jong, *Eur. Patent* 0,574,994 A1 (1993).
- A.J. Mora, A.N. Fitch, M. Cole, R. Goyal, R.H. Jones, H. Jovic, S.W. Carr, *Journal of Materials Chemistry* 6 (1996) 1831.
- R.E. Morris, S.J. Weigel, N.J. Henson, L.M. Bull, M.T. Janicke, B.F. Chmelka, A.K. Cheetham, *J. Am. Chem.* 116 (1994) 11849.
- W.J. Mortier, J.J. Pluth, J.V. Smith, *Mater. Res. Bull.* 10 (1975) 1319.
- W.J. Mortier, J.J. Pluth, J.V. Smith, *Nature* 256, (1975) 718.
- W.J. Mortier, J.J. Pluth, J.V. Smith, *J. Catal.* 45 (1976) 367
- W.J. Mortier, G.S.D. King, L. Sengler, *J. Phys. Chem.* 83 (1979) 2263.
- W.J. Mortier, J.R. Pearce, *American Mineralogist* 66 (1981) 309.
- J.M. Newsam, M.M.J. Treacy, W.T. Koetsier, C.B. de Gruyter, *Proc. R. Soc. Lond. A*, 420 (1988) 375.
- G.S. Nivarthi, A. Feller, K. Seshan, J.A. Lercher, *Micropor. Mesopor. Mater.* 75 (2000), 35.
- P. Norby, *J. Appl. Cryst.* 30 (1997) 21.
- E. Nusterer, P.E. Blöchl, K. Schwarz, *Chem. Phys. Letter*, 253 (1996) 448.
- D.H. Olson, E. Dempsey, *J. Catal.* 13 (1969) 221.
- Z. Otwinosky and W. Minor In: C.W. Carter Jr. and R.M. Sweet, Editors, *Method in Enzymology: Molecular Crystallography*, Part A, Academic press, New York (1997) 30.
- L. Parker, D.M. Bibby, G.R. Burns, *Zeolites* 13 (1993) 107.
- I.E. Paukov, I.A. Belitsky, Y.A. Kovalevskaya, *J. Chem. Thermodynamics* 33 (2001) 1687.
- S. Perego, R. Amarilli, R. Millini, G. Bellussi, G. Girotti, G. Terzoni, *Micropor. Mater.* (1996) 6.
- E. Passaglia, E., Pongiluppi, D., and Vezzalini, G. *N. Jb. Mineral. Mh.* (1978) 310.
- A.J. Perrotta, C. Kirby, B.R. Mitchell, E.R. Tucci, *J. Catal.* 55 (1978) 240.
- W. Peters, *Instrumental methods of FCC catalyst characterization*. In *Fluid Catalytic Cracking: Science and Technology*; Magee, J. S., Mitchell, M. M., Jr., Eds.; Elsevier: New York, 76, (1993)183.
- I.J. Pickering, P.J. Maddox, J.M. Thomas, A.K. Cheetham, *J. Catal.* 119 (1989) 261.

- J.A. Rabo, G.J. Gajda in: D. Barthomeuf, E.G. Derouane and W. Hoelderich, Editors Guideline for mastering the properties Of Molecular Sieves, NATO ASI Series B Vol. 22, Plenum, New York (1990) 273.
- F. Raatz, J.C. Roussel, R. Cantiani, G. Ferre, J.B. Nagy, Stud. Surf. Sci. Catal. 37 (1988) 301.
- F. Raatz, C. Travers, C. Marcilly, T. Des Courieres, F. Fajula, F. Figueras, US Pat. 5, 157 (1991) 198.
- E.F. Rakiewicz, A.J. Benesi, M.W. Grutzeck, S. Kwan *J. Am. Chem. Soc.*, 120 (25) (1998) 6415
- A.J. Regis, Geological Society of America Abstracts with Programs, 2 (1970)661.
- P.H. Ribbe, G.V. Gibbs, Am. Mineral. 54 (1969) 85.
- J.W.Jr. Richardson, J.J. Pluth, J.V. Smith, Acta Crystallographica C 43 (1987) 1469.
- R. Rinaldi, J.J. Pluth, J.V. Smith, Acta Crystallogr. B 31 (1975) 1603.
- F. Rinne, Sitzungsber. Preuss. Akad. Wiss. 14 (1890) 1163.
- L.D. Rollman, NATO ASI Ser. E-60, "Zeolites: Science and Technology", R. Ribeiro et al, p. 109, (1984).
- L. Rodriguez-Gonzales, F. Hermes, M. Bertmer, E. Rodriguez- Castellon, A. Jimenez-Lopez, U. Simon, Applied Catalysis A: General 328 (2007) 174.
- A.R. Ruiz-Salvador, G. Sastre, D.W. Lewis and C.R.A. Catlow, J. Mater. Chem. 6 (1996), 1837.
- J.A. Ryder, A.K. Chakraborty, A.T. Bell, J. Phys. Chem. B 104 (2000) 6998.
- H. Sang, H.Y. Chu, J.H. Lunsford, Catal. Lett. 26 (1994) 235.
- A. Sani, G. Vezzalini, P. Ciambelli, M.T. Rapacciuolo, Microp. and Mesop. Mater. 31 (1999) 263
- A. Sani, G. Cruciani, G.F. Gualtieri, Physics and Chemistry of Minerals, 29, 5, (2002) 351
- J. Sauer, C.M. Kolmel, I.R. Hill, R. Ahlrichs, Chem. Phys. Letters 164 (1989) 193.
- J. Sauer, in: J.T. Hynes, J.P. Klinman, H.H. Limbach, R.L. Schowen R.L. (Eds), Hydrogen-transfer reactions. Wiley-VCH, (2007) 685.
- M. Sawa, M. Niwa, Y. Murakami, Zeolites 10 (1990) 532.
- T.-C. Sheng, I.D. Gay, J. Catal. 145 (1994) 10.
- G.M. Sheldrick, SHELXL93. Program for the Refinement of Crystal Structures. University of Göttingen, Germany (1993).
- P. Simonic, T. Armbruster, American Mineralogist 89 (2004) 421.
- J.V. Smith Mineral Soc Am Spec Paper (1963) 281.
- J.V. Smith, J.J. Pluth, R. C.Boggs, D. G. Howard, J. Chem. Soc., Chem. Commun. (1991) 363.
- L.J. Smith, A.K. Cheetham, R.E. Morris, L. Marchese, J.M. Thomas, P.A. Wright, J. Chem. Science 271 (1996) 799.
- L.J. Smith, A. Davidson, A.K. Cheetham, Catal. Lett. 49 (1997) 143.
- V. Solinas, R. Monaci, B. Marongiu, L. Forni, Appl. Catal. 5 (1983) 171.
- M.H.W. Sonnemans, C. den Heejer, M. Crocker, J. Phys. Chem. 97 (1993) 440.
- K. Ståhl, J.C. Hanson, Microporous and Mesoporous Materials, 32 (1999) 147.
- J.D., Stich, K. Gale, M.C. Terakura, Paine, Chemical Physics Letters 283 (1998) 402.
- E. Stuckenschmidt, W. Joswig, W.H. Baur, Eur. J. Mineral. 8 (1996) 85.
- M.P. Szostak, A. Hensel, F.O. Eko, R. Klein, T. Auer, H. Mader, A. Haslberger, S. Bunka, G. Wanner, W. Lubitz, W., J. Biotechnol. 44, (1995) 161.
- R.N. Sukheswala, R.K. Avasia, M. Gangopadhyay, Mineral. Mag. 39 (1974) 658.
- V. Termath, F. Haase, J. Sauer, J. Hutter, M. Parrinello, J. Am. Chem. Soc. 120 (1998) 8512.
- F.E. Trigueiro, D.F.J. Monteiro, F.M.Z. Zotin, E. Falabella, Sousa-Aguiar, Alloys Compounds 344 (2002) 337.
- S.M. Tomlinson, R.A. Jackson, C.Richard, A. Catlow, J. Chem. Soc., Chem. Comm. (1990) 813
- P. Tschaufeser, S.C. Parker, Journal Physical Chemistry 99 (1995) 10609.
- G.V. Tsitsishvili, M.K. Charkviani, Stud. Surf. Sci. Catal. 28 (1986) 161.
- G.V. Tsitsishvili, T.G. Andronikashvili, G.N. Kirov, L.D. Filizova Natural Zeolites Ellis Horwood, Chichester (1992)
- F. Tuinstra, G.M. Fraase Storm, *J. Appl. Cryst.* 11 (1978) 257

- C. Tuma, J. Sauer, Chem. Phys. Letters 387 (2004) 388
- D.E.W. Vaughan, K.G. Strohmaier, Patent EP0589693 (2002)
- P.A. Vaughan, Acta Crystallogr. 21 (1966) 983.
- G. Vezzalini, S. Quartieri, E. Passaglia, IV. Jb. Mineral. Mh. (1990) 504.
- G. Vezzalini, S. Quartieri, E. Galli, A. Alberti, G. Cruciani, Å. Kvick, Zeolites 19 (1997) 323.
- A.G. Vigdorichik, Yu.A. Malinovskii, Kristallografiya 31 (1986) 879.
- R.L. Wadlinger, G.T. Kerr, E. J. Rosinski, US Patent No. 3,308,069 Mobil Oil Corporation (1967) 395.
- F. Wakabayashi, J.N. Kondo, K. Domen, C. Hirose, J. Phys. Chem. 100 (1996) 1442.
- Q. Wang, T.C. Tsai, S.T. Huang, Ind. Eng. Chem. Res. 29 (1990) 2005
- Z. B. Wang, A. Kamo, T. Youeda, T. Komatsu, T. Yashima, (1998)
- O. Weigel, E. Steinhoff, Z. Kristallogr. (1925) 61
- S.J. Weigel, J.C. Gabriel, E.. Gutierrez Puebla, A.. Monge Bravo, N.J. Henson, L.M. Bull, A.K. Cheetham, J. Am. Chem. Soc. 118 (1996) 2427.
- M. Wiebcke, G. Engelhardt, J. Felsche, P.B. Kempa, P. Sieger, J. Schefer, P. Fischer, J. Phys. Chem. 96 (1992) 392.
- A.S. Wilson, Crystal Structure Communications 11 (1982) 809.
- W.S. Wise, R.W. Tschernich, American Mineralogist, 61 (1976) 60.
- P.A. Wright, W. Zhou, J. Perez-Pariente, M. Arranz, J. Am. Chem. Soc. 127 (2005) 494
- W.-Q. Xu, Y.-G. Yin, S.C. Suib, J.C. Edwards, C.L. O'Young, J. Phys. Chem. 99 (1995) 9443.
- P. Yang, T. Armbruster, Eur. J. Mineral. 10 (1998) 461.
- L. Zhu, K. Seff, D.H. Olson, B.J. Cohen, R.B. Von Dreele J. Phys. Chem. B, 103 (1999) 10365.
- S.A. Zygmunt, L.A. Curtiss, L.E. Iton, M.K. Erhardt, J. Phys. Chem. 100 (1996) 6663.